

University of Alberta

**P- and S-wave velocity measurement and pressure sensitivity analysis of
AVA response**

by

Tiewei He 

A thesis submitted to the Faculty of Graduate Studies and Research
in partial fulfillment of the requirements for the degree of

Master of Science

in

Geophysics

Department of Physics

Edmonton, Alberta

Fall 2006



Library and
Archives Canada

Bibliothèque et
Archives Canada

Published Heritage
Branch

Direction du
Patrimoine de l'édition

395 Wellington Street
Ottawa ON K1A 0N4
Canada

395, rue Wellington
Ottawa ON K1A 0N4
Canada

Your file *Votre référence*
ISBN: 978-0-494-22284-3
Our file *Notre référence*
ISBN: 978-0-494-22284-3

NOTICE:

The author has granted a non-exclusive license allowing Library and Archives Canada to reproduce, publish, archive, preserve, conserve, communicate to the public by telecommunication or on the Internet, loan, distribute and sell theses worldwide, for commercial or non-commercial purposes, in microform, paper, electronic and/or any other formats.

The author retains copyright ownership and moral rights in this thesis. Neither the thesis nor substantial extracts from it may be printed or otherwise reproduced without the author's permission.

AVIS:

L'auteur a accordé une licence non exclusive permettant à la Bibliothèque et Archives Canada de reproduire, publier, archiver, sauvegarder, conserver, transmettre au public par télécommunication ou par l'Internet, prêter, distribuer et vendre des thèses partout dans le monde, à des fins commerciales ou autres, sur support microforme, papier, électronique et/ou autres formats.

L'auteur conserve la propriété du droit d'auteur et des droits moraux qui protègent cette thèse. Ni la thèse ni des extraits substantiels de celle-ci ne doivent être imprimés ou autrement reproduits sans son autorisation.

In compliance with the Canadian Privacy Act some supporting forms may have been removed from this thesis.

Conformément à la loi canadienne sur la protection de la vie privée, quelques formulaires secondaires ont été enlevés de cette thèse.

While these forms may be included in the document page count, their removal does not represent any loss of content from the thesis.

Bien que ces formulaires aient inclus dans la pagination, il n'y aura aucun contenu manquant.


Canada

Abstract

Reservoir conditions, such as pore pressure and fluid saturation levels, will change during the production of fluids and enhanced oil recovery. These changes will also influence the seismic wave properties of the rock. In order to better understand its seismic response, compressional and shear wave velocities were measured on a series of low porosity conglomerates under different confining and pore pressures and under both dry and water saturated conditions using standard pulse transmission methods. As expected, the dry P-wave velocities always increase after the dry sample is saturated with water. Conventional assumptions from Gassmann's relations suggest that S-wave velocity would drop after water saturation; however, in this study an increase of S-wave velocity was observed. To better understand time-lapse seismic data, we also performed pressure sensitivity analysis of the P-P and P-SV reflectivity on a simple two layer interface using complete Zoeppritz's equations based on the laboratory velocity measurement.

Acknowledgements

First of all, I would like to thank Douglas Schmitt for his supervision and help during my graduate studies in this department. I would also like to thank Len Tober for his technical assistance with the laboratory experiment and Dean Rokosh for assisting in SEM imaging and thin section on these samples.

I would also like to take this opportunity to thank my wife, Fenglian Xu, for the happiness she brought to me. Her kindness, generosity, consideration, and all her merits beyond words have made my graduate studies and also my life much easier and happier. I also thank my newborn baby, Colin, for the happiness he brings to my family, although he is not as considerate as his mom.

This work was funded in part by a research grant from Burlington Resources Ltd. and by the Discovery grant funding to Dr. Schmitt from the National Science and Engineering Research Council of Canada. Partial stipend support came from teaching and research assistantships awarded from the Department of Physics at the University of Alberta.

Table of content

Chapter 1: Introduction.....	1
1.1 Objectives.....	1
1.2 Chapter Descriptions.....	3
Chapter 2: Background Concepts.....	6
2.1 Underlying assumptions and definitions.....	7
2.2 Effect of pore structure.....	10
2. 2.1 Equant pores.....	10
2.2.2 Crack-like porosity.....	12
2.3 Effect of clay.....	16
2.4 Confining and pore pressure.....	17
2.5 Pore fluids and saturation.....	19
2.6 Gassmann's equation.....	21
2.7 Summary.....	25
Chapter 3: Experimental Configuration and Procedure.....	26
3.1 Experimental configuration.....	26
3.1.1 Pressurization system.....	27
3.1.2 Piezoelectric system.....	29

3.2 Sample preparation	31
3.3 Velocity Determination and Calibration.....	33
3.4 Experimental protocol.....	40
3.5 Summary.....	43
Chapter 4: Material Characterization.....	44
4.1 Geological characterization.....	44
4.2 Core sampling	57
4.3 Determination of grain density	61
4.4 Bulk density and porosity.....	62
4.5 Mercury porosimetry.....	64
4.6 Optical thin section analysis.....	72
4.7 SEM/ESEM and X-ray analysis.....	79
4.8 Summary.....	90
Chapter 5: Experimental Results.....	91
5.1 Introduction.....	91
5.2 Example of Raw Waveforms.....	92
5.3 Changes in P-wave and S-wave velocities with pressure.....	96
5.4 Water saturation and velocity dispersion.....	110
5.5 V_p/V_s ratios and Poisson's ratio	116
5.6 Effective stress coefficient	120
5.7 Discussions and conclusions.....	129
Chapter 6: Pressure and Fluid Sensitivity of AVA Response.....	131
6.1 Background of amplitude versus angle analysis.....	131

6.2 Zeoppritz's equations.....	138
6.3 Petrophysical sensitivity of reflection coefficient.....	142
6.4 Summary.....	150
Chapter 7: Conclusion.....	151
7.1 Summary of work in the thesis.....	151
7.2 Contributions of this work.....	153
7.3 Recommendations and future research directions.....	154
References	156
Appendix: Experimental Data of the Samples	166

List of tables

3.1	Sample dimensions of the eight cylindrical samples.....	31
4.1	The well location, lithology and depth of the eight samples.....	57
4.2	Grain volume as determined from He porosimetry, weight and grain density of the eight samples.....	62
4.3	The bulk density and the porosities determined using different methods.....	63
5.1	Best fit parameters using equation (2) for the experimental velocity data. “Dry” represents the parameters for the dry sample; “Sat” means the parameters for the water saturated samples and “Par” is the partially water saturated samples (~7%).....	110
5.2	Effective stress coefficient n for P- and S-wave velocities at constant differential pressures of 15 MPa and 30 MPa.....	122
6.1	The density, P- and S-wave velocities of each layer on a simple two-layer model. The parameters used in layer two are based on the lab measurement of sample SB007.....	145

List of Figures

2.1 Illustrative variations in the effective bulk K and shear μ moduli with porosity for spherical pores within a quartz matrix according to Eqns 2.5 and 2.6. The bulk K_s and shear μ_s moduli of the solid mineral quartz grains, are 37.8 GPa and 44.3 GPa.....	11
2.2 The closure pressure as a function of aspect ratio within a material with elastic properties of $E=74$ GPa and Poisson's ratio = 0.2.....	14
2.3 Graphic illustration of the volume change upon the increasing of confining pressure.....	15
3.1 The experimental configuration mainly consists of the confining pressure system, the pore pressure system and the signal acquisition system.....	27
3.2 The sample is sealed with plastic tubing with two aluminum buffers on each end of the sample.....	28
3.3 The changes in shape of the ceramic material generated by electric pulse for the P- and S-wave transducers. The solid line is the original shape and the dashed line outlines the shape after the particle motion.....	30
3.4 A pair of buffers attached with P- and S-wave transducers using conductive epoxy.....	30
3.5 Pictures of the eight cylindrical conglomerate and sandstone from the Cadotte formation in central western Alberta.....	32

3.6	The upper figure shows the setup determining the travel time through the two aluminum buffers; the lower figure shows the setup of determining the travel time through the aluminum buffers and the rock sample.....	34
3.7	Two typical P-wave signals at confining pressure 40 MPa, Figure a is the signal through the two aluminum buffers; Figure b is the signal through the two aluminum buffers and the rock sample.....	35
3.8	Figure a and b are the transit time changes through the aluminum buffers with the confining pressure for the P- and S-wave respectively.....	35
3.9	Typical P- (Figure a and c) and S-wave (Figure b and d) signals through the head to head transducers in time and frequency domain.	36
3.10	Typical P- (Figure a and c) and S-wave (Figure b and d) signals through the 4 cm plexiglass sample in time and frequency domain.....	37
3.11	Figure a shows the P-wave velocity changes with effective pressure for four PMMA samples with different length. Figure b shows the deviation of P-wave velocity changes from the average velocities at given pressures of the four acrylic samples.....	39
3.12	Figure a shows the S-wave velocity changes with effective pressure for four PMMA samples with different length. Figure b shows the deviation of S-wave velocity changes from the average velocities at given pressures of the four acrylic samples.....	39
3.13	Sealed sample using previous method showing the sealing material and where the fluid can break through the assembly. The white arrow points to one of the holes of the heat shrink after leaking	42

4.1	Isopach (i.e. thickness) map of the total Cretaceous and Paleocene section with oil and gas-generating areas (after Masters, 1984). The area of the Deep Basin was redefined by Masters (1984) to be delineated by the 'gas window', i.e. the zones in which the thermal maturity of the basin only allows for the existence of free gas. Figure from Masters (1984) permission to use granted by the American Association of Petroleum Geologists.....	46
4.2	Generalized stratigraphic chart for the Lowermost Cretaceous section of the Deep Basin area studied. Chart is based on the work of Hayes et al. (1994). It indicates the geological timing of the various regional geological units. The rocks here are sampled from the Cadotte member	50
4.3	Thin section of Cadotte conglomerate sample SB002 (depth of 2403.7 m in 15-29-66-11W6) showing rounded clasts predominantly of chert and quartz. Image acquired using high resolution scanner in back-lit mode at 1200 dpi resolution.....	52
4.4	Thin section of Cadotte sandstone sample SB008 (depth of 2455.1 m in 15-29-66-11W6).....	53
4.5	Simplified cross section A-B across Alberta through the Deep Basin highlighting the unusual behaviour of water-saturated zones up-dip from gas-saturated zones. Figure from Davis (1984) with permission to use granted by the American Association of Petroleum Geologists.....	55
4.6	Pore fluid pressure in water and gas saturated zones of the Cadotte member as a function of elevation relative to sea-level. Figure is developed after that of Davis (1984) with permission to use granted by the American	

Association of Petroleum Geologists.....	56
4.7 Location of the three wells where the eight cores of sandstone and conglomerate are taken from. The red circles represent the three wells where the samples are from.....	59
4.8 Available geophysical well logs for 6-30-66-11W6 (Latitude 54.74111° N, Longitude -119.65222° W) Left Panel: Natural gamma ray intensities (in arbitrary API units) versus depth from the kelly bushing (i.e. the drill rig floor). Right panel, Bulk density as estimated by active gamma-ray log via Compton scattering effect in kg/m ³ and compressional wave velocity in m/s versus depth from kelly bushing.....	60
4.9 The pore diameter versus the corresponding intrusion pressure curve. The pressure required for the mercury to intrude into the pores increases with the decreasing pore diameter.....	65
4.10 Cumulative (blue line) and incremental intrusion (green line) of mercury versus increasing pressure for sample SB002.....	68
4.11 Cumulative (blue line) and incremental intrusion (green line) of mercury versus increasing pressure for sample SB003.....	68
4.12 Cumulative (blue line) and incremental intrusion (green line) of mercury versus increasing pressure for sample SB004.....	69
4.13 Cumulative (blue line) and incremental intrusion (green line) of mercury versus increasing pressure for sample SB005.....	69
4.14 Cumulative (blue line) and incremental intrusion (green line) of mercury versus increasing pressure for sample SB006.....	70

4.15 Cumulative (blue line) and incremental intrusion (green line) of mercury versus increasing pressure for sample SB007.....	70
4.16 Cumulative (blue line) and incremental intrusion (green line) of mercury versus increasing pressure for sample SB008.....	71
4.17 Cumulative (blue line) and incremental intrusion (green line) of mercury versus increasing pressure for sample SB009.....	71
4.18 Typical thin section images of a Cadotte conglomerate with the pore spaces saturated with blue died epoxy viewed a) under plane polarized light, rectangle represents areas of higher magnification in b) magnified view under plane polarized light and c) magnified and rotated view under cross- polarization.....	75
4.19 Typical thin section images of a Cadotte sandstone with the pore spaces saturated with blue died epoxy viewed a) under plane polarized light, rectangle represents areas of higher magnification in b) magnified view under plane polarized light and c) magnified and rotated view under cross- polarization.....	76
4.20 The thin section of sample SB005. It shows a high degree of pressure solut- ion as evidenced by the irregular suturing at the grain boundaries.....	77
4.21 A thin section of sample SB002, an excellent thin section showing internal fracturing in a quartz grain.....	78
4.22 SEM image of the highest porosity and permeability sample SB004. There are no non-silica/quartz minerals in this image. Pressure solution of quartz and chert gains would have provided the chemical material for precipitation	

of euhedral quartz overgrowth crystals and the finer grained silica cement...	83
4.23 SEM image of sample SB004 showing kaolinite on quartz overgrowth.	
Here, most of the quartz overgrowth is not well-formed euhedral crystals....	84
4.24 SEM image of SB005 shows an abundance of quartz overgrowth crystals in a variety of shapes and sizes. Note that the scale of 100 microns (0.1 mm) is the lower size limit of a fine sand grain; hence, some of the overgrowth crystals in this reservoir grow to substantial size and occlude porosity.....	85
4.25 SEM image of sample SB007 showing a low magnification view of kaolin booklets nestled against fine to medium grained sand. A fracture is evident in the lower right of the image.....	86
4.26 SEM image of sample SB008 showing silica cement and illite in tight sandstone along with a few small pores that are not connected.....	87
4.27 SEM image of Sample SB008 showing clay-sized crystals of euhedral quartz overgrowth, with indeterminate white clay, along with illite in tight sandstone. As indicated in the image, microporosity is evident.....	88
4.28 ESEM image of sample SB004 showing multiple fractures (white arrows), some of which are open. Above the upward-pointing white arrow on the right appears to be braided microfractures, which are likely to be natural rather than induced.....	89
5.1 The full set of waveform of P-wave (Figure a) and S-wave (Figure b) traces of the dry sample SB007 at different confining pressures.....	94
5.2 The waveform of P-wave (Figure a) and S-wave (Figure b) traces of the water saturated sample SB007 at different confining pressures when the	

	differential pressure was constant at 30 MPa.....	95
5.3	The P- (Figure a) and S-wave (Figure b) velocities versus effective pressure curve showing some consolidation upon repeatable pressurization and depressurization less than 60 MPa.....	98
5.4	The P- (Figure a) and S-wave (Figure b) velocities of dry, partially saturated (~7%), experimentally determined and Gassmann's equation determined water saturated sample SB006 as a function of effective pressures.....	101
5.5	The P- (Figure a) and S-wave (Figure b) velocities of dry, partially saturated (~7%), experimentally determined and Gassmann's equation determined water saturated sample SB007 as a function of effective pressures.....	102
5.6	The P- (Figure a) and S-wave (Figure b) velocities of dry, partially saturated (~7%), experimentally determined and Gassmann's equation determined water saturated sample SB007 as a function of effective pressures.....	103
5.7	The P- (Figure a) and S-wave (Figure b) velocities of dry, experimentally determined and Gassmann's equation determined water saturated sample SB009 as a function of effective pressures.....	104
5.8	Experimental data and the best-fit curves for SB007. The star and diamond lines represent the experimental data for the dry V_P and V_S respectively. The red line and black line indicate the best-fit curves by least squares fitting method using equation 5.1 and 5.2 respectively.....	107

5.9	Test of the predictability of the empirical equations. The actual experimental data to 100 MPa is compared against the empirical curves determined from the observed velocities to 60 MPa for sample SB007. The star and diamond represent the experimental data for the dry V_P and V_S . The red line and black line indicate the best-fit curves by lsqr method using equation 5.1 and 5.2 respectively.....	108
5.10	P-wave (Figure a) and S-wave (Fig b) velocity changes with density for the dry samples at zero effective pressure, pressure 45MPa and extremely high effective pressure.....	109
5.11	Changes in the dry and water saturated (both experimentally determined and Gassmann's equation predicted) bulk (Figure a) and shear moduli (Figure b) with effective pressure. The Gassman's equation predicted shear moduli is equal to the dry shear moduli	114
5.12	P-wave (Figure a) and S-wave (Figure b) velocity changes as a function of effective pressure for the dry, experimental and Gassmann's equation predicted values of water-saturated sample (SB007) with a higher peak pressure 100 MPa.....	115
5.13	Velocity dispersion between theoretical Gassmann and the observed laboratory measured P- and S-wave velocities as a function of effective pressure for a fully saturated sample.....	116
5.14	P- and S-wave velocity ratio as a function of effective pressure for sample SB007. The star, square represent the experimental data for the dry and the water saturated respectively. The solid line indicates the best-fit curves	

using lsqr method.....	119
5.15 Poison's ratio as a function of effective pressure for sample SB007. The star, square represent the experimental data for the dry and the water saturated respectively. The solid line indicates the best-fit curves using lsqr method.....	119
5.16 Crossplot of P-wave against S-wave velocities for four dry and water-saturated samples. The colors represent different samples, and circles and stars represent the velocities of the dry and water-saturated samples at different effective pressures respectively. Higher velocity corresponds to higher effective pressure. The blue line is the 'mudrock line' defined by Castagna et al. (1985).....	120
5.17 P-wave velocity (Figure a) and S-wave (Figure b) as a function of confining pressure and differential pressure for water saturated, but spoiled, sample SB004.....	123
5.18 P-wave velocity (Figure a) and S-wave (Figure b) as a function of confining pressure and differential pressure for water saturated sample, but spoiled, SB005.....	124
5.19 P-wave velocity (Figure a) and S-wave (Figure b) as a function of confining pressure and differential pressure for water saturated sample SB006.....	125
5.20 P-wave velocity (Figure a) and S-wave (Figure b) as a function of confining pressure and differential pressure for water saturated sample SB007.....	126

5.21 P-wave velocity (Figure a) and S-wave (Figure b) as a function of confining pressure and differential pressure for water saturated sample SB008.....	127
5.22 P-wave velocity (Figure a) and S-wave (Figure b) as a function of confining pressure and differential pressure for water saturated sample SB009.....	128
6.1 Sketch map showing the reflected P- and S-wave in upper layer and the transmitted P- and S-wave in lower layer of an incident P-wave in upper layer on a solid-solid interface. i_1, i_2 represent the reflected and transmitted angles for P-wave; j_1, j_2 represent reflected and transmitted angles of S-wave respectively; ρ_1, V_{P1}, V_{S1} are the density, P- and S-wave velocities in the upper media; ρ_2, V_{P2}, V_{S2} are the density, P- and S-wave velocities in the lower media.....	134
6.2 A gas model showing the gas sand encased in shale (From Ostrander (1984) with the permission to use by the Society of Exploration Geophysics).....	135
6.3 P-wave reflection coefficient changes with angle of incidence for the above gas model, figure from Ostrander (1984) with the permission to use granted by the Society of Exploration Geophysics.....	135
6.4 P-wave reflection coefficient at the top of class I, II, III and IV gas sands, figure from Castagna et al. (1998) with permission to use granted by the Society of Exploration Geophysics.....	136

6.5	AVO gradient versus AVO intercept crossplot showing the differing classifications within the A-B space. Quadrants of this space are numbered from I to IV in a counterclockwise fashion, figure from Castagna et al., 1993 with permission to use granted by Society of Exploration Geophysics.	142
6.6	P-P and P-SV reflection coefficient as a function of angle of incidence on a two layer isotropic interface. The V_p , V_s and density of the lower layer are the experimental values of sample SB007 at effective pressure 45MPa.....	146
6.7	P-P and P-SV reflection coefficient as a function of angle of incidence on a two layer isotropic interface. The V_p , V_s and density of the lower layer are the experimental values of sample SB007 at effective pressure 20MPa	146
6.8	P-P (Figure a) and P-SV (Figure b) reflection coefficient as a function of angle of incidence and pressure. The velocities in the lower layer are the Gassmann's equation predicted velocities of the water-saturated sample SB007.....	147
6.9	P-P (Figure a) and P-SV (Figure b) reflection coefficient as a function of angle of incidence and pressure. The velocities in the lower layer are the experimentally measured velocities of the water-saturated sample SB007.....	148
6.10	A and B as a function of effective pressure. The velocities in the lower layer are the dry, experimentally measured and Gassmann's equation predicted velocity values of the water-saturated sample SB007.....	149

6.11 The AVO gradient and AVO intercept for the simple two layer model using the velocities of dry and water saturated sands as calculated using Gassmann's Eqn. 2.13 at different pressure. The intercept (A) increases with the increasing effective pressures..... 149

Chapter 1

Introduction

1.1 Objectives

Over the last 50 years, the primary goal of seismic reflection exploration in the petroleum industry was to reveal prospective hydrocarbon ‘traps’. Some examples of traps range from large anticlines, through thinning sedimentary beds, to small faults. As such, the techniques employed focused on delineating the geological structures with great success in the development of both acquisition technology and computational algorithms that allow for well resolved 3-D images of the subsurface. These seismic techniques and particularly those associated with 3-D imaging, led to much higher rates of discovery and ultimate recovery that likely forestalled the now-looming potential shortfalls between production and consumption.

Geological structure by itself, however, only indicates potential locations for hydrocarbon accumulations; and reveals nothing directly as to the existence of such fluids. Further risk reduction requires that additional information, usually via the seismic amplitudes, must be employed. This additional information is usually obtained by analysis of the seismic amplitudes, the simplest being strong reflections, or ‘bright spots’, typically indicative of accumulation of free gas to more refined methods that analyze variations in reflection strength and polarity with angle of incidence. These latter

methods are often referred to as *amplitude versus offset* (AVO) or *amplitude versus angle* (AVA).

An oft-ignored corollary to AVA analysis is that, essentially, it depends on the mechanical rock properties and density of the rock on either side of the geological interface producing the seismic reflections. As expected, in a porous rock these physical characteristics are influenced by the state of saturation (i.e. what fluids inhabit the pore space of the rock). What is not yet well recognized, despite having been known by rock physicists since Adams and Williamson's (1923) pioneering high pressure and temperature experiments, is the degree to which these properties are influenced by a variety of factors that include the confining and pore fluid pressures, temperature, composition, and porosity.

The work reported in this thesis was originally undertaken to address these issues in the context of a conventional seismic exploration problem associated with a deep gas reservoir of the conglomeritic Cadotte formation of the Western Canada Sedimentary Basin. Briefly, this is accomplished by making measurements of the P-wave and S-wave velocities of the rocks under a variety of confining and pore fluid pressures and pore fluid saturation states. The results are then used to provide suggestions as to the behaviors of the seismic reflectivity of the Cadotte under different saturation states as an important goal of exploration is to attempt to reduce the risk in drilling by locating, for example, the existence of free gas (i.e. usually methane) instead of water.

In the course of these studies, however, the unique '*double-porosity*' pore structure and relatively simple composition became apparent; and in addition to serving their original purpose also yielded some more fundamental insights on velocity dispersion in

high frequency laboratory experiments and on the concept of effective pressure in the context of elastic velocities. While these aspects will be pointed out, a detailed analysis of them is beyond the scope of the current work.

The thesis begins with a more general review of the factors that influence seismic and ultrasonic velocities with particular focus on those factors relevant to the conglomerates studied here. This is followed by an overview of the petrophysical characterization and geological provenance of the conglomerates. The new techniques of simultaneous P- and S-wave ultrasonic velocity measurement when the pore fluid saturation is controlled, both developed specifically for this work, are then detailed. Measurements on a series of these conglomerates with a typical range of porosities under a variety of saturations and pore and confining pressures are presented. The more fundamental implications of these results are then briefly discussed. Finally, the thesis attends to its original motivation with a simple but illustrative case study of the influence of the factors of pressure and saturation on seismic reflectivity from this formation.

1.2 Chapter Descriptions

With the rapid increase in the price of natural gas, previously passed over reservoirs are now worthy of consideration; the conglomerate Cadotte deposits of West Central Alberta are one such example. In order to better understand the seismic response AVO anomaly of such formations, a series of laboratory velocity measurements on representative sandstones and conglomerates from three wells were carried out. In this thesis, the P-wave and S-wave velocities of eight such conglomerate and sandstone samples were measured under different confining pressure and pore pressure for the dry and water

saturated samples. These core logs have relatively low porosity (<10%) and low clay content.

Chapter 2 contains a review of previous work related to factors, such as the structure of the porosity, that influence the measurement of elastic wave velocities in porous materials particularly at ultrasonic frequencies. This includes a discussion of the concept of 'double porosity' and microcracks and their manifestation in the nonlinear elastic responses of rock. The existence of either dry or fluid filled cracks strongly influences the elastic responses of the rocks, particularly at low confining pressures. The concept of effective pressure is presented. Finally, velocity dispersion (i.e. the variation in elastic wave velocity with frequency) is one issue that continually confounds the interpretation and application of ultrasonic measurements on saturated porous rocks and is discussed in detail as the experimental observations in this thesis are able to shed some new light on this problem.

In chapter 3, the geological factors that affects the seismic velocities are characterized through standard microscope thin section, Scanning Electron Microscopy (SEM), and differing types of porosimetry. The pore geometry, particularly the microcracks, is of special interest in this study; therefore they are described in detail from the images and measurements of these samples. The geology of the Cadotte formation is also overviewed in the beginning of this chapter.

Chapter 4 describes the experimental configuration newly updated for these measurements, which now includes the pore pressure system, confining pressure system and the signal acquisition system. The new arrangement of the sample and transducers greatly improve the precision of the velocity. This chapter also describes the sample

preparation and velocity determination from the recorded signals and some experimental protocols for subsequent laboratory work.

Chapter 5 discusses the changes of seismic velocities, the elastic moduli, V_p/V_s ratio and Poisson's ratio as a function of the pore and confining pressure. The effective stress coefficient relating the pore and confining pressure is also discussed in this chapter. The velocities as a function of pressure measured in water-saturated samples are then compared with the theoretical values predicted from Gassmann's equation.

To better understand the time-lapse seismic data, the pressure sensitivity analysis of P-P and P-SV reflection coefficient on a simple two layer interface using complete Zoeppritz's equations were performed in Chapter 6.

Summaries of the chapters with a synoptic overview and directions for future work are described in the concluding Chapter 7.

Chapter 2

Background Concepts

During oil/gas production and enhanced oil recovery processes, pore fluid pressure will increase or decrease during fluid injection or depletion; the fluid saturation also changes during gas injection and water invasion. These changes in reservoir fluid pressure and saturation can induce changes in the reservoir acoustic properties of the host rocks such as the density, the compressional and the shear wave velocities. The changes in reservoir density and velocity can be reflected in the amplitude versus offset (AVO) responses and time shift of the time-lapse seismic data. Time-lapse seismic survey is important for monitoring the fluid movement in hydrocarbon depletion reservoirs. Therefore, appropriate knowledge of the in situ rock properties changes with the reservoir condition changes can provide an adequate interpretation of AVO responses and time-lapse seismic data.

Seismic properties are affected by many factors, such as stress, pore pressure, fluid state and pore geometry. Rock physics is mainly focused on the mechanisms affecting the rock properties. It is the bridge connecting seismic data and the reservoir characteristics. Laboratory measurements of the variations of the seismic properties with these parameters do provide information useful to the interpretation of the seismic data, particularly if pore fluid pressure effects cannot be ignored. In particular, the confining

and pore pressure dependence of the velocities and water saturation effect will be extensively studied using the conventional pulse transmission technique in this thesis.

2.1 Underlying assumptions and definitions

Some basic concepts of elasticity theory and elastic wave propagation are presented here in order to properly define some of the physical properties that will be used throughout the thesis. A basic knowledge of elasticity is presumed here including the solution of the elastic wave equation. The reader will find this in numerous introductory texts in Physics, Continuum Mechanics, Elasticity, and Geophysics and little is to be gained by reiterating this material here. Some basic assumptions employed here, however, are that the rock is isotropic (i.e. the properties are independent of direction) and that the rock is homogenous at the scale of the wavelengths of the elastic waves passing through. We realize that in reality these assumptions will break down to some degree. However, at the current state of this study these assumptions are presumed to hold. We hope in future studies to examine their validity. Under these conditions, a material will have a mass density ρ (in units of kg/m^3) and because of isotropy only two elastic properties of the bulk modulus (or incompressibility) K and the shear modulus μ , both in units of pressure $\text{Pa} = \text{N/m}^2$ are required. An alternative, but equally valid, way to describe a material's elastic properties is with the first $\lambda = K - 2\mu/3$ and second μ Lamé parameters also given in units of pressure. The dimensionless Poisson's ratio ν will also be employed and can be related to the moduli via $\nu = (2\mu - 3K)/(3K + 4\mu)$. Finally, although more useful in engineering contexts the Young's modulus $E = (3\lambda + 2\mu)\mu/(\lambda + \mu)$ will also appear occasionally when its use will simplify the equations.

These moduli are important as they are directly related to the speeds at which elastic waves propagate. The derivations of these speeds are again provided in many texts and only the final results are provided here. Through a fluid (gas or liquid) only one longitudinally polarized compressional P-wave will propagate with a bulk wave velocity (in units of m/s)

$$V_p = \sqrt{\frac{K}{\rho}} \quad (2.1)$$

and through a solid

$$V_p = \sqrt{\frac{K + 4\mu/3}{\rho}} = \sqrt{\frac{\lambda + 2\mu}{\rho}} \quad (2.2)$$

The transverse polarized shear S-wave travels at:

$$V_s = \sqrt{\frac{\mu}{\rho}}. \quad (2.3)$$

but only through materials that can support a shear stress. These relations are relatively simple and are all that is needed later to relate observed velocities to *effective* elastic moduli. We shall see, however, that the *effective* moduli are influenced by a number of factors that make understanding the velocities of rock challenging. Some of the relevant factors are described in the following subsections. Aspects of the strength of seismic reflections, also an important component of this thesis, are delayed to later chapters in order to first concentrate on the wave propagation issues.

Before continuing, it is useful to describe a few additional parameters that will arise repeatedly. Generally, the mass density of a rock from a petroleum perspective will be given by:

$$\rho = (1 - \phi)\rho_s + (S_w\rho_w + S_o\rho_o + S_g\rho_g)\phi. \quad (2.4)$$

where ϕ is the porosity (ratio of the void space volume to the total bulk volume) and the subscripts S, W, O, and G refer to the solid (i.e. mineral grain), water, oil (i.e. liquid hydrocarbon), and gas constituents. The saturations S_W , S_O , and S_G are the fractions of the void space taken up by the given fluid phase or water, oil, or gas. For example, a rock whose pore space is completely filled with water and no other fluid will have $S_W = 1$ while $S_O = S_G = 0$. Often, the term ‘dry’ will be used and this is usually taken to mean in the literature that the pore space is essentially empty or at most containing only a highly compressible gas at low pressure such that the fluid effects can be ignored. A final assumption is that if the rock is saturated with different fluids then the distribution of these fluids at the pore scale is homogenous.

There is one last point that must be addressed with respect to later discussions and this focuses on the usage of the term *effective* in the context of the elastic properties of a material. *Effective moduli* (and including Poisson’s ratio) are representative of the overall bulk response of a composite material, such as a fluid saturated rock. That is, what we really observe, particularly in seismic observations, is the bulk response of the ‘homogenous’ composite even though at the scale of the pores and minerals the material would look highly heterogeneous. For example, in these experiments both P- and S-wave velocities are measured. These observed rock velocities differ substantially from those for the rock’s fluid and mineral constituents as do the *effective* moduli that may be simply calculated using the above Equations. The difficulties lie in determining what controls the values of these *effective* moduli; the literature on this topic is vast and here the focus is on those situations most relevant in helping to explain the experimental results. Hereafter, unadorned symbols K , μ , λ , and v refer to the *effective* properties of the rock, that is these

will be what the seismic wave ‘senses’ and what needs to be used in the relationships between elastic properties and wave velocities above. We will see that these effective moduli will depend on the intrinsic moduli of the solid and fluid components as well as on the moduli of the rock’s framework.

Unfortunately, for historical reasons the term *effective* is also used later in the context of the extrinsic conditions of stress or pressure; the more casual reader will need to understand that this will have a different meaning which will be introduced in Chapter 5.

2.2 Effect of pore structure

Porosity is the most important single factor controlling the elasticity of a ‘dry’ porous material, and in general greater porosity ϕ leads to diminished K and μ . Past this comprehensive statement, however, there is no simple or unique relationship between the moduli and porosity. A number of additional factors must be considered but the most fundamental relate to the pore geometries with two broad classifications of stiff rounded pores and compliant crack-like pores.

One way to distinguish the type of pore is through a simple measure of the aspect ratio $\alpha = w/l$ of the width w to the length l . The aspect ratio for ‘open’ pores with more equant dimensions is close to unity. For crack like pores, however, $l \gg w$ and the aspect ratio approaches zero.

2. 2.1 Equant pores

It has long been known in engineering that round arc-like structures can support a considerable load; indeed many such Roman structures such as bridges, aqueducts, and

the Pantheon in Rome still stand after nearly 2 millennia. The same concept essentially applies directly to the stiffness of rounded pores in materials; such pores cannot be collapsed without irreversibly damaging the material. Hereafter they will be referred to as the ‘stiff’ porosity. Walsh (1965) provided straightforward relations for the effective bulk modulus of a solid of intrinsic (i.e. pore-free) bulk modulus K_s and Poisson’s ratio ν_s containing a dilute concentration of spherical pores

$$K = \frac{K_s}{1 + \frac{3(1-\nu_s)\phi}{2(1-2\nu_s)(1-\phi)}} \quad (2.5)$$

that agreed with the earlier results of MacKenzie (1950) and Eshelby (1957). MacKenzie (1950) also provided expressions for the effective shear modulus:

$$\mu = \mu_s \left(1 - \frac{15(1-\nu_s)\phi}{7-5\nu_s} \right) \quad (2.6)$$

Figure 2.1 is a plot showing the effect of pore porosity on the effective bulk and shear modulus using the equation 2.5 and 2.6.

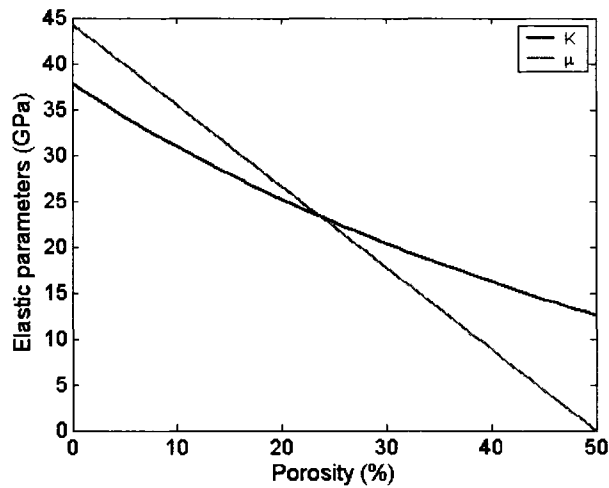


Figure 2.1: Illustrative variations in the effective bulk K and shear μ moduli with porosity for spherical pores within a quartz matrix according to Eqns 2.5 and 2.6. The bulk K_s and shear μ_s moduli of the solid mineral quartz grains are 37.8 GPa and 44.3 GPa.

2.2.2 Crack-like porosity

Most rocks in the upper crust contain cavities with shapes ranging from spherical to planar microcracks and grain contact. The microcracks can be introduced through the geological process such as pressure relief from erosion and cementation from circulating groundwater. They only represent an extremely small amount of porosity. The presence of flat, low aspect ratio microcracks has been identified for a long time as a pronounced effect on the elastic properties (Adams and Williamson, 1923; Simmons and Brace, 1965; Walsh 1965; Brace, et al. 1972). Velocities of rocks generally decrease with increasing porosity for certain kind of rock. However, this velocity-porosity relationship becomes complicated when microcracks exist in the rocks, because the elastic properties of a rock are more affected by the microcracks (Kuster and Toksöz, 1974). When fluids are present, the surface area of the low aspect ratio pores and cracks becomes more important than the porosity itself (Tatham, 1982) and they can cause velocity dispersion effect due to microscopic local fluid flow.

The evolution of the more compliant microcracks depends on the changes of the pore pressure and confining pressure. It generally closes with the loading of confining pressure. Batzle etc. (1980) observed microcrack closure in rocks under increasing pressure directly with a scanning electron microscope. It showed that the long and narrow cracks closed at relatively lower pressures. The closure of cracks will increase the compressibility of rock and the complete crack closure will result in an equal compressibility as that of the uncracked rock. The rock sample generally becomes stiffer as the cracks are closed with progressively increasing confining pressure. The establishment of the elastic properties and fracturing is of great interest for the

geophysicist to understand the seismic properties of producing reservoir. Several models (e.g. Walsh, 1965; O'Connell and Budiansky, 1974; Toksöz et al. 1976; Kozlov, 2004) have been proposed to describe theoretically the behavior of cracks and its effect on the elastic properties. The principle crack parameters affecting the elastic properties in these models are crack length and face roughness of the crack. Walsh (1965) concluded that the compressibility is independent of the aspect ratio of a crack and is more affected by the presence of a few long cracks. The theoretical calculations by Toksöz et al. (1976) showed that the small aspect ratio pores (cracks) would have a greater effect on the elastic properties than the higher aspect ratio pores for a given concentration of pores with other parameters fixed.

The presence of the cracks in the rocks has two common features. Firstly, the compressional and shear wave velocities and the rock stiffness are considerably reduced. Secondly, the increase of effective confining pressure will result in the closure of cracks. Small α cracks are first closed and the closure then proceeds to higher aspect ratio cracks with the increase of effective pressure. Walsh (1965) derived an analytic expression for the closure pressure P_χ of a 'penny-shaped' crack of aspect ratio α

$$P_\chi = \frac{\pi E_s \alpha}{4(1-\nu_s^2)} \quad (2.7)$$

For illustrative purposes, the closure pressure is plotted as a function of aspect ratio (Figure 2.2) and shows that the longest, thinnest cracks are easily closed while equant pores close only with difficulty. Walsh (1965) further derived a formula for the effective bulk modulus of a material containing such penny shaped cracks:

$$K = \frac{K_s}{1 + \frac{16}{9} \frac{1-\nu_s^2}{1-2\nu_s} \frac{\bar{c}^3}{\bar{V}}} \quad (2.8)$$

where for N cracks in volume V_o the average crack length is

$$\bar{c} = \sqrt[3]{\frac{1}{N} \sum_N c^3} \quad (2.9)$$

and the average region volume is

$$\bar{V} = \frac{1}{N} V_o \quad (2.10)$$

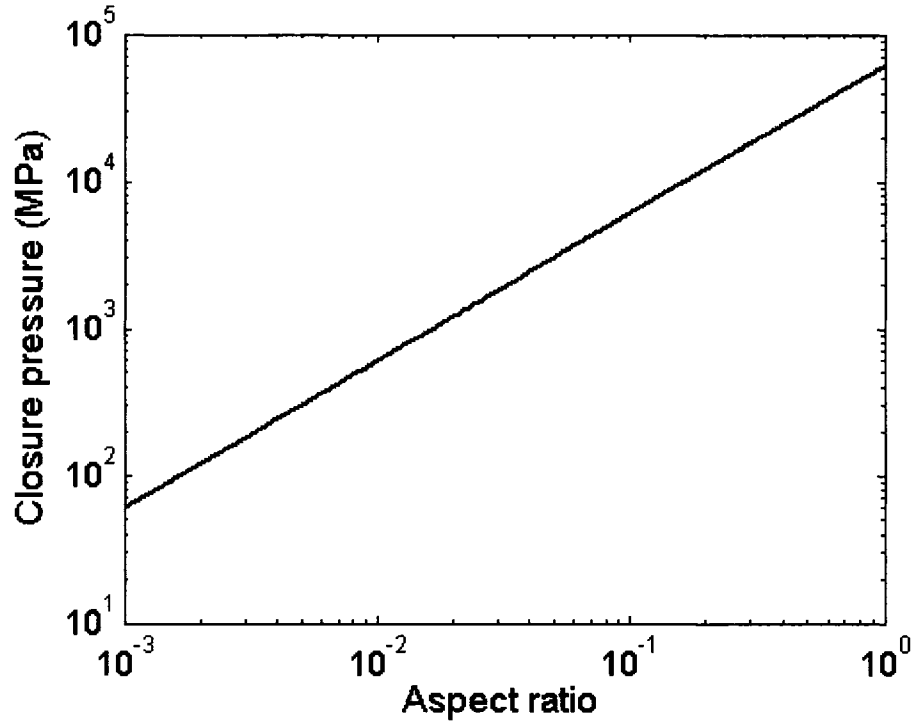


Figure 2.2: The closure pressure as a function of aspect ratio within a material with elastic properties of $E=74$ GPa and Poisson's ratio = 0.2.

As a result the elastic moduli, and hence the seismic velocities, of rocks are dependent on the external confining pressure P_c , the velocities will keep increasing with P_c until the microcrack porosity is closed at which point the increase slows substantially and is more indicative of the pressure dependent intrinsic changes of the minerals themselves. Looked at another way, in a rock subject to a confining pressure or stress the

more compliant cracks (i.e. those with the smallest aspect ratios) close at low pressures and upon closing the overall frame of the rock stiffens. As the pressure increases, progressively more of the cracks close and also progressively making the rock frame increasingly stiff (Figure 2.3). This process continues until all of the low aspect ratio, crack-like porosity is closed whereupon the rock's elasticity becomes that of its crack free frame.

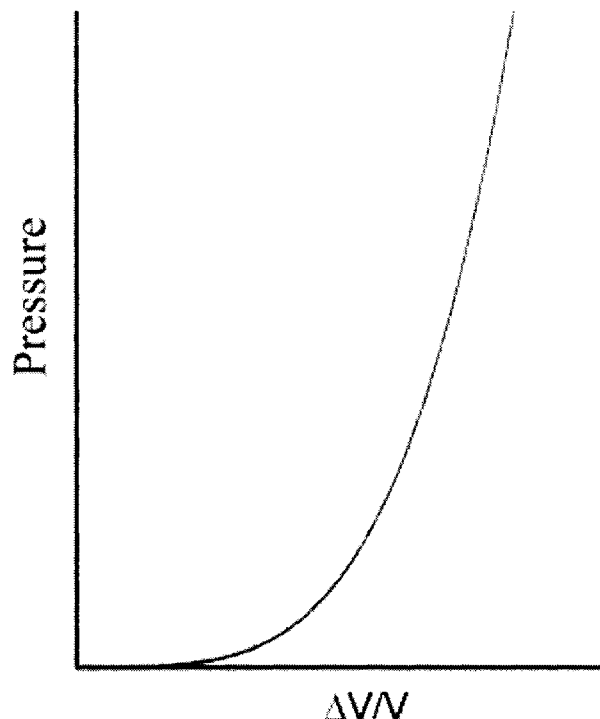


Figure 2.3: Graphic illustration of the volume change upon the increasing of confining pressure.

This nonlinear behaviour of rocks was noted in the very first measurements of velocity by Adams and Williamson (1923) who also suggested that the behaviour was due to the existence of crack-like porosity. While the underlying effect is understood, it is much less simple to understand in detail the physics of the nonlinear character of the rock and instead many authors (Zimmerman et al., 1986; Eberhart-Phillips et al., 1989;

Freund, 1992; Jones, 1995; Prasad and Manghnani, 1997; Khaksaret al., 1999; Carcione and Tinivella, 2001 Kirstetter and MacBeth, 2001; Shapiro, 2003) have just described parametrically the concave shape using a formula:

$$V = A + CP_e - Be^{-DP_e} \quad (2.11)$$

where V is the acoustic wave velocity; P_e is the effective pressure; A , C , B and D are the estimated constants using the least-square method for a given rock sample. This formula is applied later in the thesis to provide a compact representation of the results.

There are extensive theoretical developments to describe the effects of cracks on an otherwise elastic medium, and as is usually the case the number of theoretical models far exceeds the actual experimental tests. Examination of these theories are beyond the purposes of the current work but the reader is referred to the recent contributions of Mayr and Burkhardt (2006) for a brief review with links to many of the important papers in this literature. Again, the focus of the current thesis is on more direct use of the results towards an exploration problem; but it is hoped that these results can be used in future studies related to more fundamental effects.

2.3 Effect of clay

Clays are present in most of the reservoir sands and sandstones. The effect of clays on the elastic properties of the sandstone depends on the clay and sand particle contact and the clay type. The incompletely pore filling clays have little effect on the elastic properties other than changing the density, however the clay on the grain contact has a big effect by stiffening the matrix. For the high porosity sands, the material on the grain contact can strongly affect the seismic properties (Avseth et al., 2000).

The decrease of the seismic velocities due to clay is undisputed. The effect of clay content, porosity on the seismic velocities has been experimentally tested (e.g. Han et al., 1986; Eberhart-Phillips et al, 1989; Freud 1992; Khaksar et al., 1999). They showed that both P- and S-wave velocities decreases with increasing porosity and clay content. The empirical relationship can provide useful data for a group of samples of the same kind, but it cannot describe the velocity for all sandstones (Eberhart-Phillips et al, 1989). In order to provide more precise information for the in-situ seismic data, the velocity measurement of the dry rocks in a specific area are necessary.

2.4 Confining and pore pressure

Under undrained conditions (boundary conditions in which the mass of fluid within the pore space of the rock remains constant), large pore pressures P_p close to the lithostatic overburden and tectonic stresses can be introduced in some sedimentary beds sealed by impermeable rocks (Green and Wang, 1996). The pore pressure in the oil/gas producing reservoirs also changes during oil and gas depletion or fluid injection. Changes in the confining stress in the producing reservoirs can lead to the changes of seismic velocity, layer thickness, and fractures in the reservoir sands and the overburden layers. The understanding of how rocks respond to both pore pressure and total (or confining) pressure changes can provide important information in interpreting the velocity anomalies in drilling process and time shift of time-lapse data. Therefore, the knowledge of the variation of seismic velocities and elastic parameters as a function of the confining and pore pressure is very important for the well management and time-lapse studies.

This study is usually carried out using the concept of ‘effective pressure’ P_e which is often written as:

$$P_e = P_c - nP_p \quad (2.12)$$

where P_c is the total or confining stress that acts on the external boundary of the material and n is a coefficient that describes the influence of the pore pressure on the material properties. Many studies have shown that the seismic velocities and the elastic moduli are highly dependent on the effective pressure (e.g. Eberhart-Phillips et al, 1989; Carlson and Gangi, 1995; Prasad and Manghnani, 1997; Khaksar et al., 1999), while they remain constant at constant effective pressure. The effective pressure is dependent on the confining pressure and pore pressure. The relationship between velocity and effective pressure in most of rocks is nonlinear, and indeed this would be the curve for the rock with no pore pressure in it as discussed above. The velocity shows a rapid increase when the effective pressure initially increases from zero, then the rate of velocity increase with effective pressure decreases with the loading of effective pressure. The changes of the velocity with effective pressure are mainly attributed to the closure of the intra- and intergranular microcracks or some small aspect ratio pores during the loading of pressure. Most microcracks are closed below certain confining pressure that is defined as the “microcrack closure pressure” and the corresponding velocity is the crack-free velocity. Except for acting as the media for the wave propagation, the fluid in the pores also plays an important role by supporting the rock matrix against the lithostatic pressure so that the rock matrix cannot be squeezed upon the loading confining pressure. The effect of the pore pressure on the p-wave and s-wave velocities has been studied (Wyllie, etc., 1958; King, 1966; Christensen and Wang, 1985; Prasad and Manghnani, 1997), and it showed

that the increase of the internal pore pressure of the rocks will decrease both of the compressional (V_p) and shear wave (V_s), however an equal amount of pore pressure increase cannot completely cancel the confining pressure increase. Therefore an effective stress coefficient n is introduced to calculate the effective pressure. The effective stress coefficient can be estimated from the curves of the velocity as a function of confining and pore pressure. The empirical value of n is observed to be less than unity for the Berea and Michigan sandstones (Prasad and Manghnani, 1997). The data for Berea sandstone by Christensen and Wang (1985) showed that n is observed to be less than unity for P-wave but greater than unity for the S-wave and this was explained using a grain contact model which incorporates the effects of both of the clays lining quartz grains and the pores. Observation of the experimental data demonstrated that the effective elastic coefficient n is a function of pressure (Banthia, King and Fatt, 1965), the estimation of n generally decreases with increasing confining pressure (Prasad and Manghnani, 1997).

2.5 Pore fluids and saturation

Fluids and saturation are other important factors influencing the seismic properties of rocks. The acoustic velocities in rocks with fluid are affected by two of the most important modes of fluid and solid interaction, which are Biot mechanism and squirt-flow (Dvorkin and Nur, 1993). The Biot mechanism is caused by the fluid participating in the solid's motion through viscous coupling and inertial coupling due to the wave excitation. The squirt flow (also known as local fluid flow) happens when the fluid is squeezed out the thin pores induced by the pore pressure difference caused by the propagating wave. At lower frequencies, the fluid in the more compliant microcracks will be squeezed into

the less compliant pores and fractures when acoustic wave propagates in the saturated porous rock. At higher frequencies, the microcracks will be isolated. The confined fluid in these isolated microcracks will make the rock stiffer and hence cause the elastic properties to be frequency dependent.

It is a widely used assumption that the bulk moduli will change while the shear moduli remain fixed when the sample is fully saturated with fluid according to Gassmann's equation, however, an increase of the shear moduli after saturation are reported (Baechle etc., 2005; Khazanehdari and Sothcott, 2003) and the contradiction of the observed data with the theory has been attributed to a number of mechanism, such as viscous coupling, the reduction in free surface energy, and frequency dispersion due to local flow of the fluid in the microcracks (Khazanehdari and Sothcott, 2003). The P-wave velocity generally increases after the rock is saturated with fluid. The S-wave velocity in saturated rock is less than in dry rock because the shear moduli remains the same but the density increases after saturation. As predicted by Gassmann's equation, several authors (Nur and Simmons, 1969; Domenico, 1977; Winkler, 1985) observed velocities of dry, porous rocks generally show an increase in P-wave velocities and a decrease in the S-wave velocities upon full water saturation. However, Tao et al. (1995) observed higher S-wave velocities for brine-saturated sandstone than for the dry sandstone at low effective stresses. However, at high effective pressure, the S-wave velocities for the dry sample are higher than the brine-saturated sample.

2.6 Gassmann's equation

Fluid substitution is an important method to model changes of rock properties with the fluid saturation in the reservoir. The most commonly used theoretical approach for describing seismic wave propagation in porous rocks is to employ Gassmann's (1951) formula relating the bulk modulus of a fluid saturated rock to its porosity, the bulk moduli of the solid grain, fluid and the frame.

$$K_{eff} = K_d + \frac{(1 - K_d / K_s)^2}{\frac{1 - K_d / K_s - \phi}{K_s} + \frac{\phi}{K_f}} \quad (2.13)$$

where K_f is the bulk modulus of the saturating pore fluid; K_s is the bulk modulus of the solid mineral material; K_d is the bulk modulus of the rock's frame, and ϕ is the porosity of the rock sample. It is frequently stated that the shear modulus (μ_{eff}) of an isotropic material is assumed to be unchanged by fluid saturation and hence equal to the frame shear modulus (μ_d), but Berryman (1999) clarified that this can be derived from the assumptions used to derive Gassmann's equation. He showed the derivation of Gassmann's equation, especially for the true origin of the shear moduli results.

The derivation and successful application of Gassmann's theory is based on several assumptions. Firstly, the elastic porous rock is isotropic and homogeneous and the pore space is connected. Secondly, it is only valid at very low frequencies in order that the pore pressure has enough time to reach equilibration. Thirdly, there is no chemical interaction between fluids and rock frame and the sample is under undrained conditions. At high frequencies, the low frequency assumption may be violated. However, Biot's theory (Biot, 1956a, 1956b) was developed for predicting the elastic properties of the

fluid saturated porous rock at higher frequency. The Biot's theory doesn't contradict with Gassmann's equation and can be reduced to Gassmann's equation at low frequencies.

The intrinsic values of the bulk modulus of solid (K_s) and bulk modulus of fluid (K_f) are usually relatively easy to find (e.g., Batzle and Wang, 1992; Bass, 1995). The greatest uncertainty limiting the successful application of Gassmann's equation is lack of knowledge of bulk moduli (K_d) and shear moduli (μ_d) of the dry rock frame, which is highly dependent on pore structure, effective confining stress, and temperature. Some consensus has arisen that these values can be estimated from P- and S-wave velocities measured on the "dry" (i.e., unsaturated) sample in dynamic laboratory measurement. Because of the commonly accepted fact that velocity dispersion is negligible in the "dry" samples (e.g. Gist, 1994; King and Marsden, 2002), the elastic parameters attained from the P- and S-wave velocities can be used directly in the seismic frequencies (Spencer etc. 1994). If the dry density ρ_{frame} , P- and S-wave velocities are available from dynamic laboratory measurement or wireline log data, the frame bulk modulus (K_d), the shear modulus (μ_d) and the Poisson's ratio of the sandstone can be determined according to the following equations:

$$K_d = \rho_{frame} \left(V_p^2 - \frac{4}{3} V_s^2 \right) \quad (2.14)$$

$$\mu_d = \rho_{frame} (V_s^2) \quad (2.15)$$

$$v_d = \frac{1 \left(\frac{V_p^2}{V_s^2} \right) - 2}{2 \left(\frac{V_p^2}{V_s^2} \right) - 1} \quad (2.16)$$

We can calculate the effective bulk moduli with any desired fluid. With the saturated density given simply by:

$$\rho^{sat} = (1 - \phi)\rho_s + \phi\rho_f \quad (2.17)$$

For the case of partial saturation, the effective bulk modulus of a fluid mixture in the pore space must be calculated. Under the assumption that the pore pressure increments in each phase of the fluid equilibrate during a seismic period, the effective bulk modulus of the fluid mixture (K_f) can be determined using the Reuss average:

$$K_f^{-1} = S_w K_w^{-1} + S_o K_o^{-1} + S_g K_g^{-1} \quad (2.18)$$

where S_w , S_o and S_g are the water saturation, oil and gas saturation respectively. K_w , K_o and K_g are the bulk moduli of the water, oil and gas respectively. The saturated P- and S-wave velocities are given by the usual formulas with the appropriately substituted moduli:

$$V_P^{sat} = \sqrt{\frac{K_{eff} + \frac{4}{3}\mu}{\rho^{sat}}} \quad (2.19)$$

and

$$V_S^{sat} = \sqrt{\frac{\mu}{\rho^{sat}}} \quad (2.20)$$

A number of studies have observed both theoretically and experimentally the velocity dispersion of the low frequency Gassmann's equation predicted velocities and the high frequency experimentally measured velocities of the saturated rock. Ravalec and Guéguen (1996) calculated the high- and low frequency velocity using both of the "extended differential, self-consistent model" (EM) and Gassmann's equation for a cracked model saturated with fluid. The result showed that both of the P- and S-wave velocity could have dispersion as high as 20%. They also found that the rounded pores

have no effect on the dispersion, but the cracks have a significant effect on the dispersion. The flatter the cracks are, the higher the dispersion will be. Winkler (1986) and King and Marsden (2002) experimentally observed the velocity dispersion between the high- and low frequencies values on the assumption that any departures from the Gassmann's equation predicted values are caused by dispersion. They also attributed the frequency dispersion to the existence of cracks in the saturated rock.

At unstressed state, Geertz and Knight (1998) observed a remarkable reduction in both of the P-wave and S-wave velocities when the dry rock absorbed some moisture (10% water saturation). A 2-7% of water imbibitions by the dry rock can cause a reduction in both of the P- (2.3%) and S-wave velocities (2.9%) at effective pressure from 10 MPa to 20MPa, the 'dry' sample should be defined as when the dry sample absorbs a small amount of water (King et al., 2000; King and Marsden, 2002). When applying the dynamic laboratory measurement of the "dry" frame moduli, it is important to note that the 'dry' sample should be defined as when the dry sample absorbs a small amount of water because the softening of clay content upon fluid saturation will weaken the stiffness of the pore structure and the cement (King et al., 2000; King and Marsden, 2002). However, this is not applied to our case because most of grain contact is quartz overgrowth and the clay content of our samples is rather low, furthermore, most of the clay content is kaolinite and dicitie that are not prone to shrinking or swelling with changes in water content. Therefore, the "dry frame" in this thesis represents the absolutely dry frame.

2.7 Summary

In this chapter, some basic concepts such as the underlying assumptions and definitions of elasticity theory and elastic wave propagation are briefly presented and these definitions of the physical properties will be used throughout the thesis. The mechanism and review of previous work about different factors such as pore structure, clay content, confining and pore pressure, pore fluid and saturation affecting the rock elastic properties are also described. The Gassmann's equation, one of the fluid substitution theories and the calculation of the input parameters in this equation were also introduced in this chapter.

Chapter 3

Experimental configuration and procedure

In this chapter, the details of the experimental configuration and data acquisition are described. A large part of this work was the development of a means to carry out the measurement under different conditions of pore pressures ranging from low pressure to as great as the confining pressure. As well, a new system for the simultaneous measurement of both P and S waves was developed.

3.1 Experimental configuration

The conventional pulse transmission technique was used to determine compressional- and shear-wave velocity at ultrasonic frequencies (~1 MHz). Based on the experimental configuration described by Molyneux and Schmitt (1999), the high-pressure instrument was updated as part of this project to include pressurized pore fluids. The updated experimental configuration (Figure 3.1) now consists of two pressure systems, a confining pressure system and a pore pressure system where pore fluids can be introduced and the pore fluid pressure can be varied as needed. The pore pressure line also includes a vacuum that lowers the pressure of the pore space to 0.01 Torr during the ‘dry’ measurement. This also facilitates saturation of the sample for the later ‘saturated’

measurements. This ensures that the sample is fully saturated with water and removes the air in the system to avoid partial gas saturation.

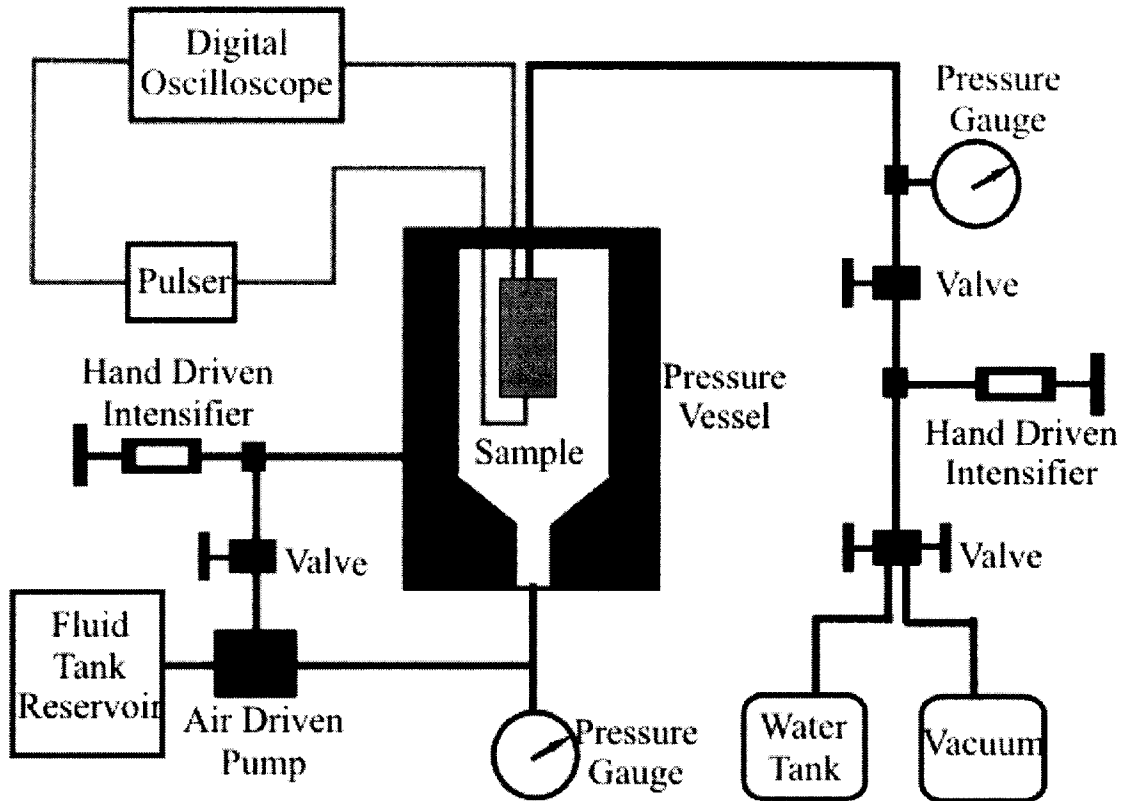


Figure 3.1: The experimental configuration mainly consists of the confining pressure system, the pore pressure system and the signal acquisition system.

3.1.1 Pressurization system

The cylindrical pressure vessel can be pressurized to apply the confining pressure (P_c) from room pressure up to 100 MPa with hydraulic oil pumped by an air-driven pump. These pressures can then be more finely adjusted with a hand driven intensifier. The confining fluid in the pressure vessel is hydraulic oil. The precision of the pressure can reach as low as 0.25 MPa with this hand-driven pump. The end cap of the pressure vessel contains a feedthrough that is connected to the digital oscilloscope (Gagescope Model

400-586-203) and an inlet for the water or air to be pumped in and out. In this study, velocity measurements were made to a peak pressure of 60 MPa that corresponds roughly to overburden lithostatic stress on these samples in situ at depths of about 2.5 km. One later measurement was made to confining pressures of 100 MPa to further test some of the observations with respect to microcrack closure.

The new pore pressure system (Figure 3.1) developed here is used to simulate the fluid pressure changes in porous formation. The water tank and vacuum are connected to the pore pressure line. The vacuum here is used to pump out the air in the pore pressure line before water saturating the sample to make sure that fully water saturated state can be fulfilled. The hand driven intensifier is used to push the water from the water tank to the pore pressure line to increase the pore pressure. In order to control the pore pressure, two aluminum buffers attached with transducers using conductive epoxy were made. On one of the aluminum buffers, there is a fluid inlet for the water to come through to control the pore pressure and saturate the sample (Figure 3.2). Two o-rings were put on each of the aluminum buffer for better sealing of the rock sample.

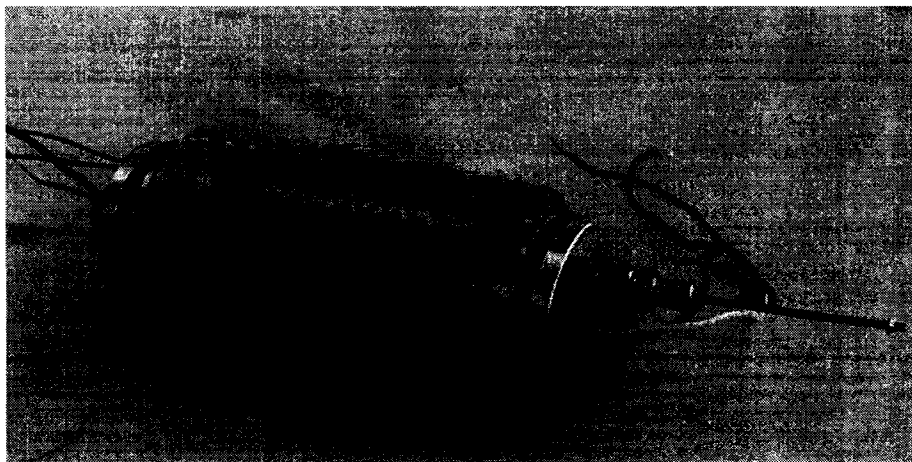


Figure 3.2: The sample is sealed with plastic tubing with two aluminum buffers on each end of the sample.

3.1.2 Piezoelectric system

The basis of velocity measurement system consists of piezoelectric ceramic materials. The project requires that both compressional (longitudinal) and shear (transverse) waves be generated. The compressional (P-wave) are produced by the axial expansion or contraction of an appropriately polarized piezoelectric material upon application of a charge in voltage. The shear (S-wave) is produced by lateral particle motions induced by transverse change in shape of a differently polarized piezo-electric material (Figure 3.3). Conversely, the shape of the piezo-electric material is changed by an arriving mechanical wave and then the ceramic would produce a voltage. Consequently, these ceramics can be used as both transmitters and receivers. Both of the P- and S-wave transducers with frequencies centered around 1 MHz are made of piezoelectric crystals (PZT-5H) from Omega Piezo Technologies Inc.. The diameter of the circular P-wave crystal is 2.54 cm and the length of the square S-wave crystal is 1.71 cm.

As part of the pore pressure design, a new method of making transducer was used for this project. In this method, both of the P- and S-wave crystals (Figure 3.4) are glued on a pair of cylindrical aluminum buffers with proper alignment with conductive epoxy. The diameter and height of the aluminum buffers are 3.81 cm 2.54 cm respectively. Because the end of the buffers lack of enough area, only half of the circular P-wave transducers were used. The damping material of these transducers is a mixture of flexible urethane putty (Flexane® manufactured by ITW Devcon) and iron powder.

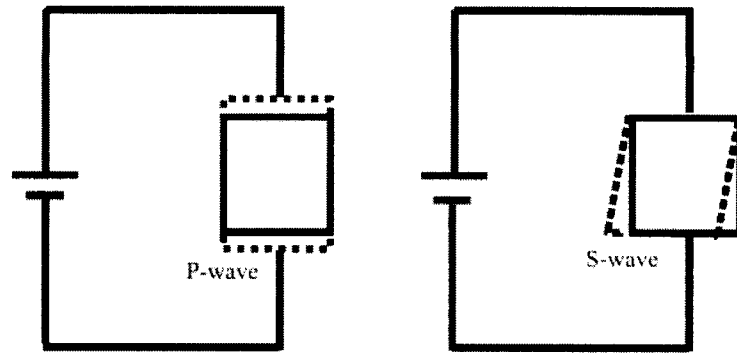


Figure 3.3: The changes in shape of the ceramic material generated by electric pulse for the P- and S-wave transducers. The solid line is the original shape and the dashed line outlines the shape after the particle motion.

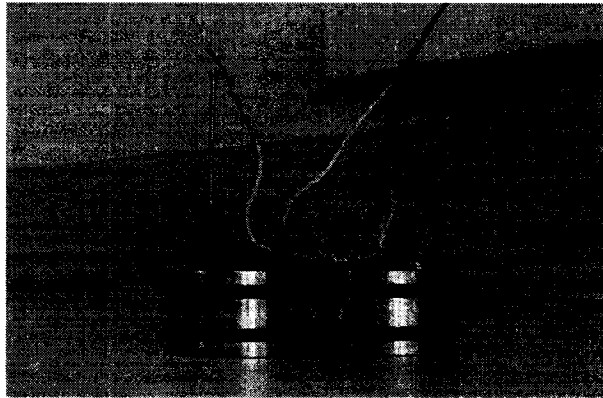


Figure 3.4: A pair of buffers attached with P- and S-wave transducers using conductive epoxy.

The experimental setup also consists of a pulse generator and a digitizing oscilloscope (Gagescope Model 400-586-203). The pulse generator is linked to an ultrasonic source transducer that uses longitudinally and transversely polarized piezoelectric (PZT) crystals to convert an electrical pulse into compressional and shear waves. The transmitting transducer is activated by a fast-rising, 200 V square wave and a mechanical compressional or shear wave is generated. The generated acoustic wave is transmitted through the sample and the received output that is digitized at an interval of 8

nanoseconds are recorded by the oscilloscope. The final waveform of a signal is the average of 256 progressively stacked records to reduce the random noise. The first extremum (peak or trough) was here defined to be the sample transit time. The transit time of the first extremum is picked to calculate the velocity.

3.2 Sample preparation

The eight cylindrical core samples were cut with lengths ranging from 5cm to 7cm (Figure 3.5). Five of the samples have a diameter of ~3.8 cm, and the other samples have a diameter of ~4.4 cm. The ends of the samples are surface ground to be parallel to within 0.02 mm. After cutting, the samples were dried in the vacuum oven for 24 hours at temperature of about 80°C and kept in desiccators before the velocity measurement.

Table 3.1 Sample dimensions of the eight cylindrical samples.

	SB002	SB003	SB004	SB005	SB006	SB007	SB008	SB009
Sample Length (mm)	5.481	5.553	5.725	6.473	5.308	5.789	5.716	5.066
Sample Diameter (cm)	4.39	3.774	4.394	4.388	3.774	3.788	3.81	3.774

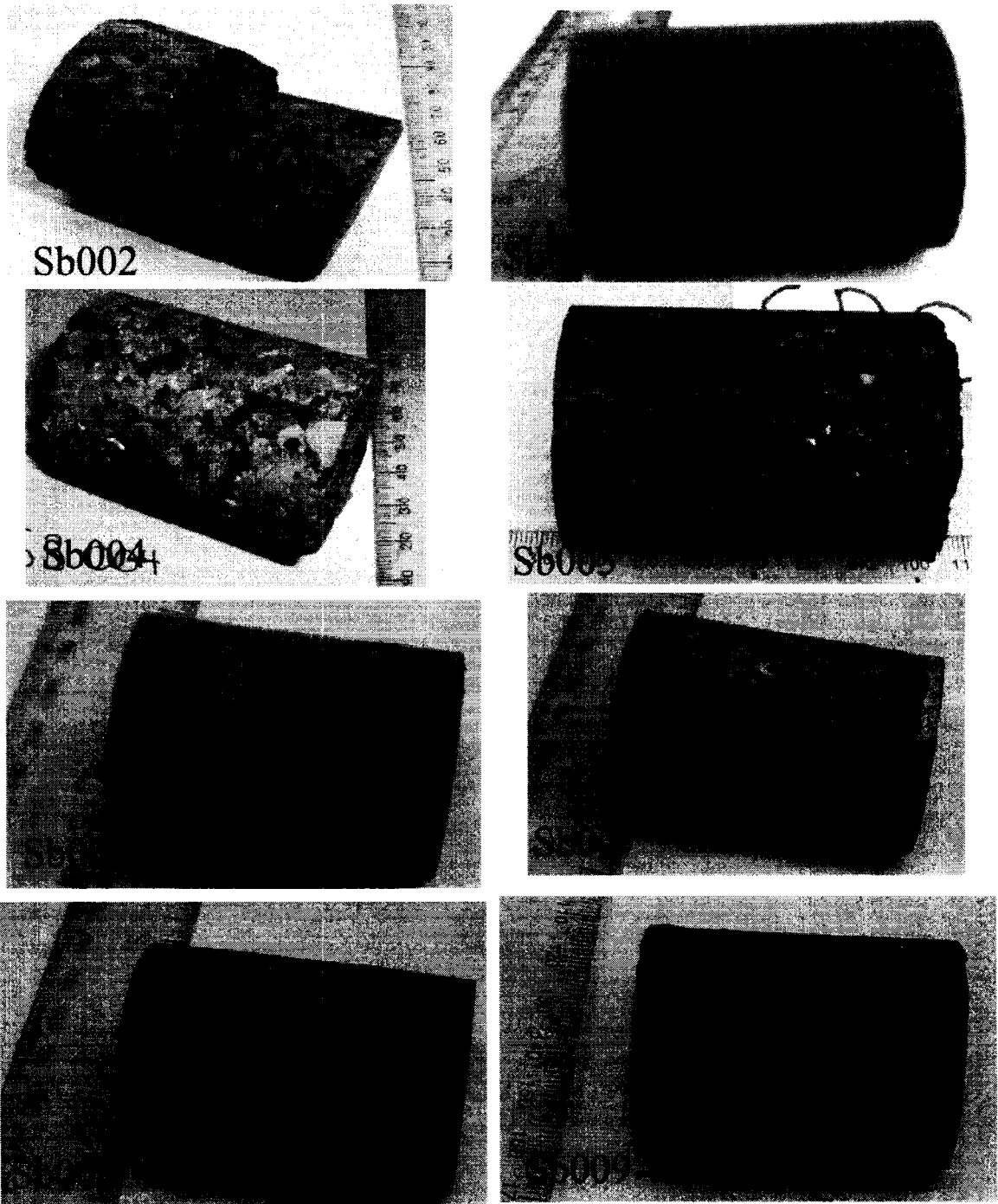


Figure 3.5: Pictures of the eight cylindrical conglomerate and sandstone from the Cadotte formation in central western Alberta.

The dried sample was pushed into the Tygon™ tubing jacket followed by the end caps (Figure 3.2). Care was taken to ensure that the P- and S-wave transducers on both

end caps were aligned with one another. The prepared sample was then put into the pressure vessel for the signal recording. Before the velocity measurement of the dry sample, the sample was evacuated down to a pressure as low as 0.01 Torr to remove any gas from the sample. After completion of the velocity measurement of the dry sample, the sample is then saturated with water using the pore pressure setup. Pressurized water was pushed directly into the vacuum pressure pore space in order to maximize saturation of the sample. We normally leave the pore pressure at 40 MPa overnight for the sample to be completely water-saturated.

3.3 Velocity Determination and Calibration

A standard pulse transmission technique is used here. In order to calculate the P-wave and S-wave velocities, the transit time taken for the generated pulse to travel through the rock sample must be determined. This transit time is usually found by picking up the travel time of a certain feature of a propagating wave signal, such as the onset or the first amplitude of the signal (Molyneux and Schmitt, 1999; Molyneux and Schmitt, 2000; King 1996). In this thesis, the wave velocities were estimated from picking the first amplitude extreme and the use of the two end caps help to simplify the travel time determination. First, the buffer travel time (t_1) is measured through the two buffers placed directly face to face. The sample is then placed between the buffers and the time t_2 through both of the aluminum buffers and the rock sample is determined (Figure 3.6 and 3.7). The travel time through the rock sample (Δt) is simply the difference $t_2 - t_1$. The velocity determined is simply the quotient of the sample length and the transit time:

$$V = L/\Delta t \quad (3.1)$$

where L is the length of the sample.

While this appears simple, the buffer transit time t_1 is not constant but depends on P_c . Figure 3.8 shows the transit time changes through the aluminum buffers with the confining pressure for the P- and S-wave. From the figure, we can see that both of the P- and S-wave transit time decreases with increasing confining pressure. Figure 3.9 and 3.10 show the typical P- and S-wave waveforms and their frequency spectra of the face to face end caps and with a 4cm acrylic Poly(methyl methacrylate) (PMMA) sample at $P_c=50$ MPa. The peak strength of the P-wave signal is centered around 1.1 MHz and the peak strength of the S-wave signal is centered on 0.9 MHz.

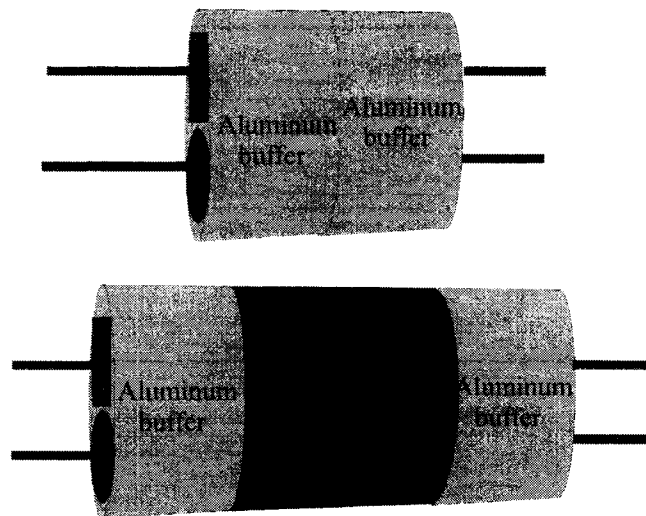


Figure 3.6: The upper figure shows the setup determining the travel time through the two aluminum buffers; the lower figure shows the setup of determining the travel time through the aluminum buffers and the rock sample.

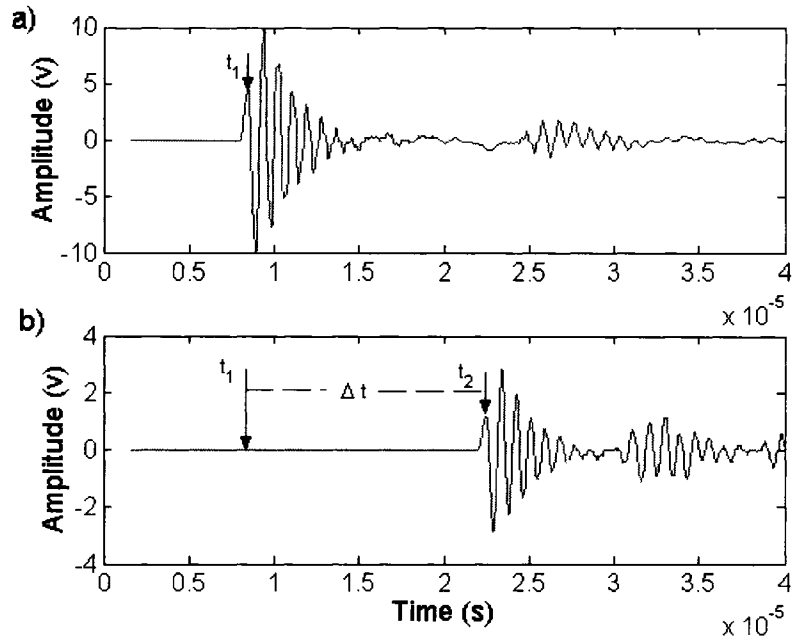


Figure 3.7: Two typical P-wave signals at confining pressure 40 MPa, Figure a is the signal through the two aluminum buffers; Figure b is the signal through the two aluminum buffers and the rock sample.

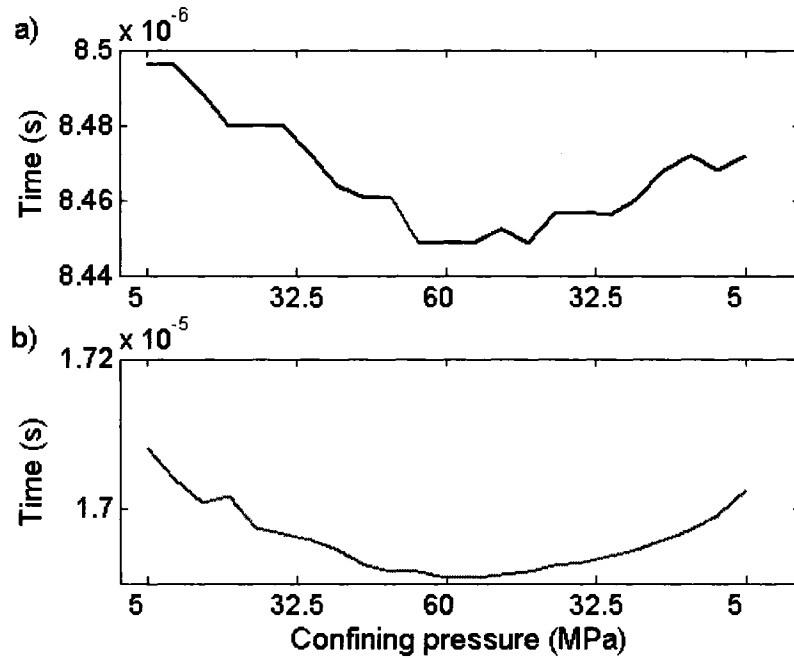


Figure 3.8: Figure a and b are the transit time changes through the aluminum buffers with the confining pressure for the P- and S-wave respectively.

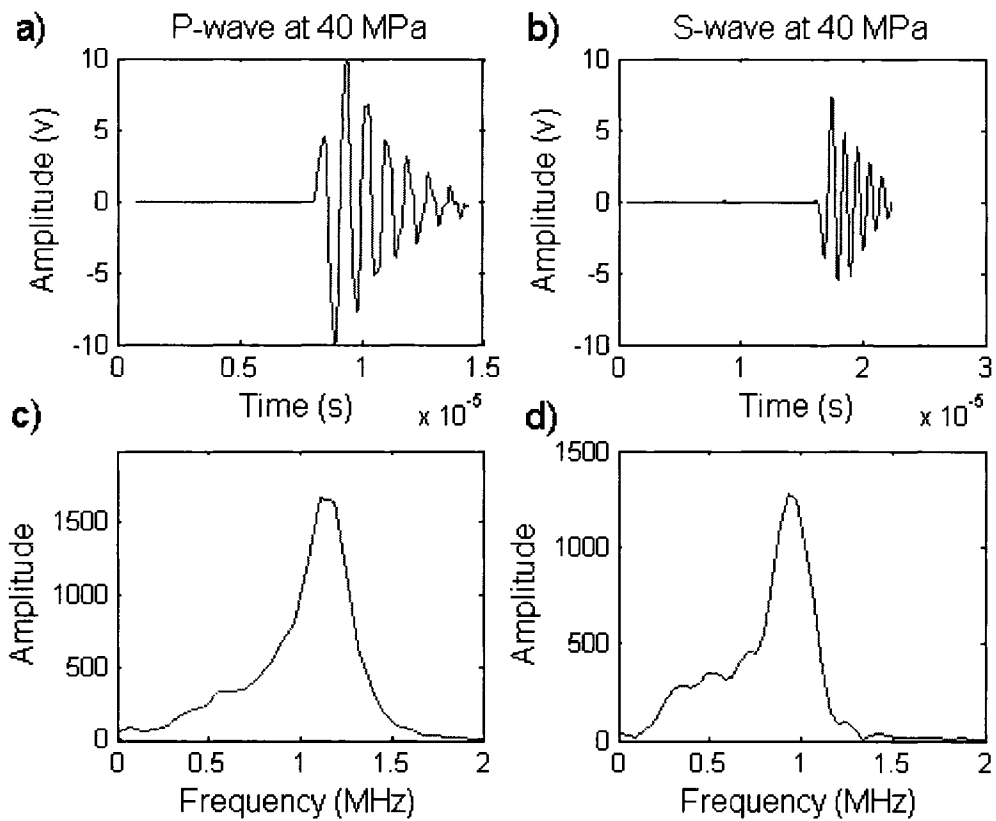


Figure 3.9: Typical P- (Figure a and c) and S-wave (Figure b and d) signals through the head to head transducers in time and frequency domain.

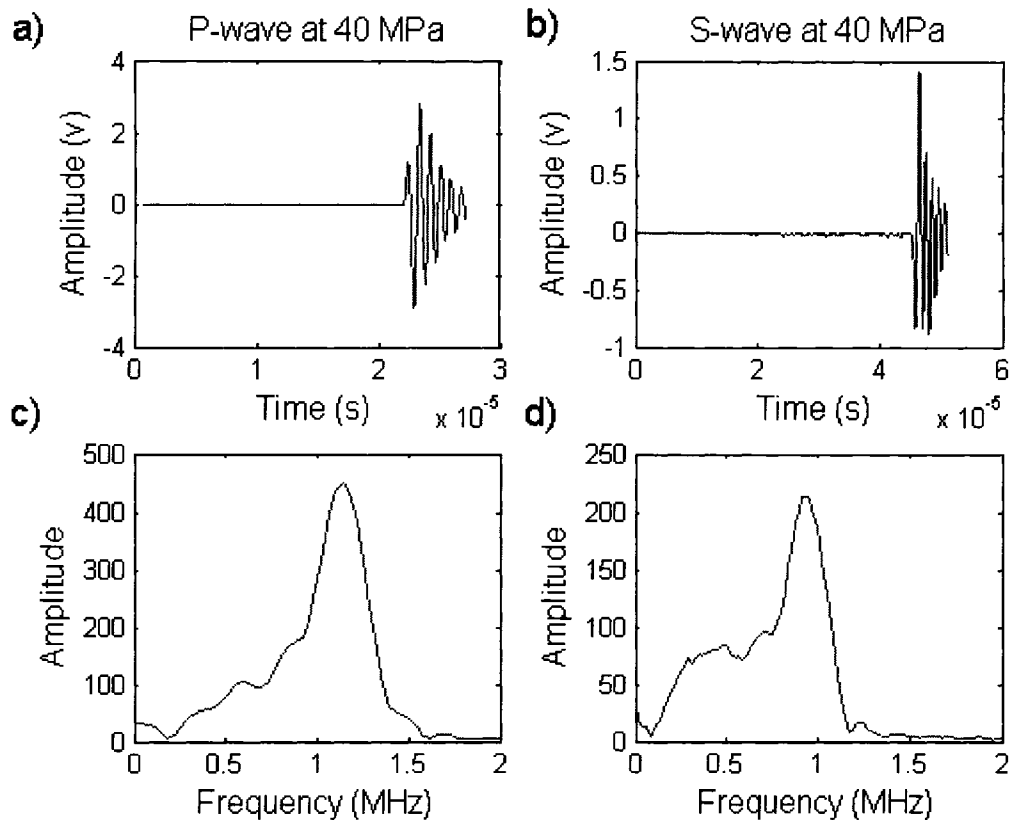


Figure 3.10: Typical P- (Figure a and c) and S-wave (Figure b and d) signals through the 4 cm plexiglass sample in time and frequency domain.

The precision of the velocity measurement is always an important issue in determining the bulk and shear moduli. The uncertainty of the velocity measurement is mainly affected by two factors: the sample length and the travel time. As mentioned before, the two surfaces of the rock sample are parallel to within 0.02 mm and this contributes to an uncertainty of velocity of about 0.05% for 5 cm long sample, which is typical for our samples. The time sampling period of the oscilloscope is 8 nanoseconds and this will give a maximum error of about 0.15% according to most of the typical velocity and length of our samples. These will give a total uncertainty of about 0.2%.

Other errors will be introduced by wave propagation effects, for this simple time picking method, if significant changes occur in the waveform shape due to attenuation.

A series of special tests were carried out in order to better assess the uncertainty of the velocity measurements directly. A set of four cylindrical standards with length of 2cm, 3cm, 4 cm and 5 cm and diameters of 3.8 cm were used for determining the repeatability of the ultrasound velocity measurement. These standards are made of the same relatively simple isotropic acrylic Poly(methyl methacrylate) (PMMA), so the velocities determined should not depend on the length. The variation in the P- and S-wave velocities with P_c for the four samples is shown in Figure 3.11 and Figure 3.12 respectively. The maximum deviation of both of the P- and S-wave velocity from the averaged velocity is only about 5 m/s. Note that the velocities are, however, pressure dependent and this further variable allows for additional testing of these uncertainties. It must be noted that no accommodation of the length of the samples due to the change in pressure was made in these calculations.

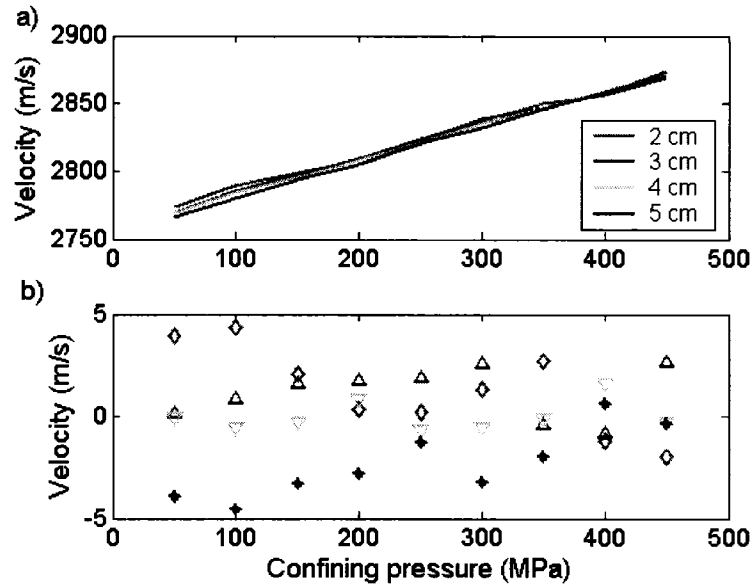


Figure 3.11: Figure a shows the P-wave velocity changes with effective pressure for four PMMA samples with different length. Figure b shows the deviation of P-wave velocity changes from the average velocities at given pressures of the four acrylic samples.

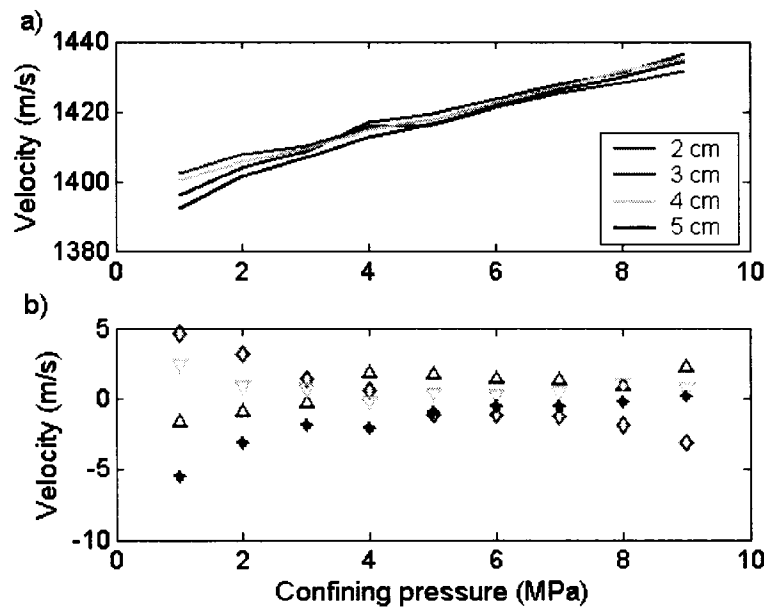


Figure 3.12: Figure a shows the S-wave velocity changes with effective pressure for four PMMA samples with different length. Figure b shows the deviation of S-wave velocity changes from the average velocities at given pressures of the four acrylic samples.

3.4 Experimental protocol

Our old sealing method is different from present one that was developed for this test due to the unique structure of the pores in these samples. For the old sealing method, the sample was attached with transducers with silver paint; it was then enclosed in the heat shrink and was simply wrapped with flexane (Figure 3.13). The wires that were attached to the transducers are a common source of hydraulic oil leakage because of the rigidity of the urethane compound. This method of sealing works, though a small percent of the samples fails, only when the pores are very small in the porous rock sample. Unfortunately the sealing jackets on samples with larger pores failed all the time with the pressurization medium (hydraulic oil) entering the pore space. When the confining pressure is very high, the hydraulic oil will penetrate both of the heat shrink and the rigid flexane, the white arrow pointing to the cavity in Figure 3.13 shows where the fluid breaks through. The more flexible high-pressure plastic tubing instead works very well even though the shape of the rock surface is not regular. From the last experiments, the samples never leaked using the new sealing method.

For the pore pressure setup, some large grain may block the inlet of the aluminum buffer and prevent the water flowing into the sample. A simple method to know whether this inlet is open is to see the changes in the amplitude of the signals. At constant differential pressure, the velocity and the attenuation are roughly consistent and don't vary significantly. Therefore a big increase of the amplitude with increasing confining pressure at constant differential pressure may indicate the inlet is blocked. The sample must be taken out and the position of the aluminum buffers moved until the large flat grains do not block the inlet.

In general the experimental protocol for the last four samples measured using the new technique followed:

1. Machining of cylindrical sample and measurement of dimensions.
2. Drying of sample under vacuum conditions in oven at 80°C.
3. Characterization including:
 - a. Measurement of dry mass.
 - b. He porosimetry (grain density determination) and calculation of ϕ_d .
 - c. Thin section preparation, photography, and high resolution scanning.
 - d. Hg porosimetry and calculation of ϕ_{Hg} .
 - e. Scanning Electron Microscopy on selected samples.
4. Preparation of dry sample for ultrasonic measurements.
5. P and S wave measurements – dry conditions
 - a. Vacuum applied to pore space of sample.
 - b. Simultaneous P and S waveforms acquired at series of pressures. Samples allowed to equilibrate at constant pressure for 15 minutes prior to acquisition of the waveforms.
 - c. Picking of travel times and calculation of velocities.
6. P- and S-wave measurements under saturated conditions. Pore space saturated with water as described.
 - a. Measurements cycled as for dry sample with pore pressure equal to room pressure.
 - b. Measurements carried out at constant differential pressures for effective pressure tests. To keep a constant differential pressure, the confining and

pore pressure were increased for the same pressure which is 50MPa in this thesis.

c. Sample removed, saturated mass m_{sat} immediately obtained and ϕ_{sat} calculated.

7. P- and S-wave measurements under partially saturated conditions.

a. Saturated sample placed in vacuum oven and was vacuumed at 20 °C.

b. Sample mass m was measured every 3 minutes in order that the sample is partially saturated with water at the desired percentage.

c. Sample rejaacketed and placed in pressure vessel.

d. P and S wave measurements repeated as with the pore pressure being the room pressure.

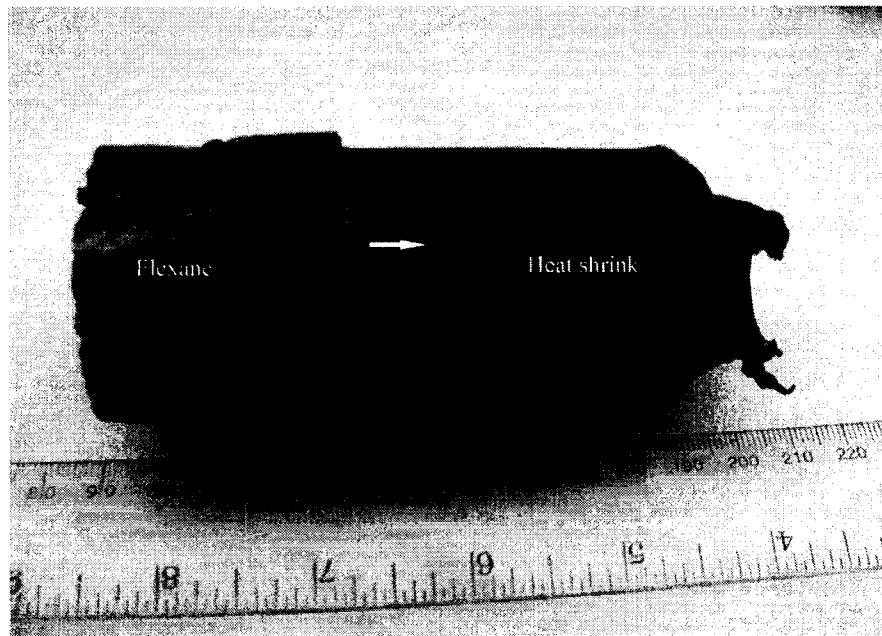


Figure 3.13: Sealed sample using previous method showing the sealing material and where the fluid can break through the assembly. The white arrow points to one of the holes of the heat shrink after leaking.

3.5 Summary

The experimental configuration here was developed to allow velocity measurement with pore pressure changes up to 100 MPa from room pressure and under water saturated conditions. A new method of transducer and sample arrangement was also designed for the particular samples with big pore size and this method allows for simultaneous velocity measurement of both of the P- and S-wave velocity. This method also simplified the sealing procedure. From a set of plexiglass samples, we have verified that the new velocity determination method gives a better repeatability of the velocity measurement with the sample length changes.

Chapter 4

Material Characterization

4.1 Geological Characterization

West-central Alberta offers huge hydrocarbon reserves. This is particularly true in the area of the 'Deep Basin' (Figure 4.1) where the existence of gas appears to not be in doubt but the productivity of the reservoirs is low. The Deep Basin went mostly ignored until the mid-1970's when some smaller companies, notably the smaller independent Canadian Hunter Exploration, investigated the hydrocarbon potential of this westernmost segment of the Western Canada Sedimentary Basin. Their search for hydrocarbons was unique in that the basis of their large economic success was careful scientific examination and integration of a wide variety of geological, petrophysical, and geophysical data. Canadian Hunter's initial 1976 discovery in the Ellmsworth field produced 20 MMscf per day of gas¹ of the scientific work that went into these discoveries is compiled in the monograph edited by Masters (1984) who suggested that the Deep Basin could contain as much as 440 Tcf (Masters, 1979). While this potential has not been realized, and indeed, recent reports refuse to even make estimates of how much gas there might be, exploration

¹ The terminology used in describing quantities of gas can be confusing. Tcf is one trillion and 1 MMscf is one million standard cubic feet of methane at 60° F and 1 atm of pressure and is a typical measure of gas in the United States and Canada, each scf has nearly 1.1×10^6 J of energy. One normal cubic metre of gas (Nm^3) is measured at 0° C and 1 atm of pressure and equals 37.326 scf. A more natural unit is the ultimate energy produced upon combustion with, for example, consumer sales in Alberta being provided in GJ; at the end of June, 2006 the price of gas at the AECO-O hub in Southern Alberta was just over \$5.00 CAD per GJ while daily spot prices exceeded \$14 CAD per GJ in December, 2005. (see <http://www.ngx.com/marketdata/NGXIASDIDX.html>)

in this area has increased dramatically in the last few years. Evidence for this interest is in the greatly increased oil and gas rights land sales to the Province of Alberta during the last year, much of this motivated by Shell Canada's recent discovery of a Tay field estimated to hold from 500 Bscf to 800 Bscf of gas south of Rocky Mountain House in December, 2005. This was found at a depth of 5.1 km in the Deep Basin. The Tay River find, which is expected to be a prolific producer, may not be most representative of gas exploration in the Deep Basin which has instead begun to focus on the lower porosity, tighter (i.e. lower permeability) sands and conglomerates which at current prices can be economically produced.

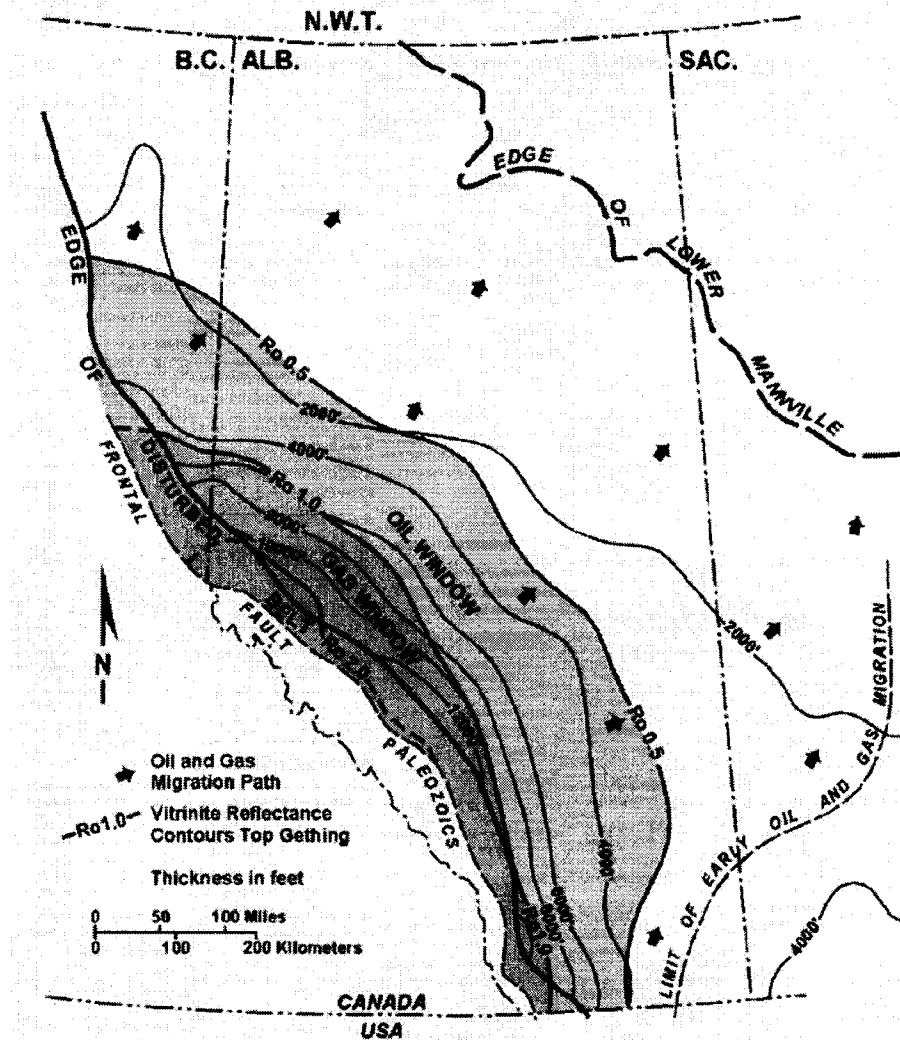


Figure 4.1: Isopach (i.e. thickness) map of the total Cretaceous and Paleocene section with oil and gas-generating areas (after Masters, 1984). The area of the Deep Basin was redefined by Masters (1984) to be delineated by the 'gas window', i.e. the zones in which the thermal maturity of the basin only allows for the existence of free gas. Figure from Masters (1984) with permission to use granted by the American Association of Petroleum Geologists.

The geological framework of these rocks is interesting. In addition to the monograph edited by Masters (1984) already mentioned, the recent M.Sc. thesis of Reinprecht (2005) has useful detailed reviews. Briefly, however, the sedimentary rocks studied are from what is referred to as the Cadotte formation of Cretaceous mid-Albian age (112 Ma to 99 Ma). The series of events that led to the deposition of these rocks is not simple but the larger history of the basin may be summarized by (Mossop and Shetsen, 1994):

1. A passive margin on the western coast of North America (Late Proterozoic to Late Jurassic, ~900 Ma to ~ 144 Ma). This consisted of slow chemical and material deposition of both carbonate and clastic sediments from the northeast on the present North American craton that produced the limestones and the clastic rocks that today can be seen in the fronts of the Canadian Rocky Mountains.
2. Development of a foreland basin (Late Jurassic to Early Eocene, ~144 Ma to 50 Ma). In this stage, the passive margin was disrupted by the collision of various terranes pushed against the original North American craton by oceanic lithospheric subduction and resulting closure of ocean basins. This resulted in the collision of these portions of crust 'accreted' to the North American craton which pushed the formerly passive margin rocks to the northeast. During this deformation phase of what is broadly referred to as the Cordilleran orogeny, the crust was shortened and thickened resulting in both an uplifted range of mountains and the consequential down-warping of the over-thrusted crust. This down-warping was due to flexure of the North American plate in isostatic response to the new heavier crustal load of

thickened material to the west. This bent crust resulted in a topographically low depression that was subsequently filled with sediments from the growing Cordilleran mountains to the west. This down-warping produced the 'foreland basin', the deepest part of course being to the west near the overthickened crust. This basin thins progressively to the north-east with the sedimentary materials completely removed in the NE corner of Alberta where Precambrian (~ 2 Ga) metamorphic rocks of the Canadian Shield first come to the surface.

3. Modern day tectonic regime (Early and Middle Eocene to present day, ~ 55Ma to present). The end of the Cordilleran orogeny effectively occurred at the time and is noted by a period of crustal extension in the Cordillera that resulted in the current plate tectonic regime. At this time sea-levels were sufficiently low that erosion of the earlier deposited sediments occurred.

The Deep Basin is immediately to the east or is overthrust by the edge of the rocks deformed by various pulses of the Cordilleran orogeny, and is deep precisely because this region of the North American crust experienced the greatest down-warping. The present day 'young' sediment wedge (rocks of Cretaceous or younger, i.e. < 144 Ma) in the foredeep for example exceeds 3.7 km. However, it is likely that already as much as 10 km of the overlying sediments have been eroded away (Beaumont, 1981).

The geological history of the basin is quite complex with many periods of high and low sea levels that influenced erosion and styles of sedimentation (Smith et al, 1984). Some of the complexity of the basin is indicated by the general stratigraphic chart (Figure

4.2) for the area which lists numerous geological formations². The rock samples here are taken from the Cadotte member of the Peace River Formation. Immediately preceding the formation of the Cadotte member in the earliest Middle Albian time (~112 Ma) sea levels are thought to have risen globally causing the Boreal sea to transgress (i.e. advance across) to the south the evidence for which is the Harmon member marine shales. Rapid sedimentation from the southwest provided abundant high wave energy materials (i.e. large grained) that formed both the Cadotte and the overlying Paddy members. One characteristic of the Cadotte is that the grain sizes coarsen upwards. Another is that the Cadotte appears to contain erosional surfaces. These observations suggest the Cadotte formed as a high wave energy barred coastline, a modern day analog for which is thought to be in the nearshore, wave and storm-dominated bars of Southern Oregon (e.g. Hunter et al., 1979).

² A geological formation (or more properly geological stratum or unit) is defined on the basis of the rock type (lithology) and is usually recognizable as a contiguous layer over a region. A given lithology is indicative of the conditions existing at the time of the rock's deposition.

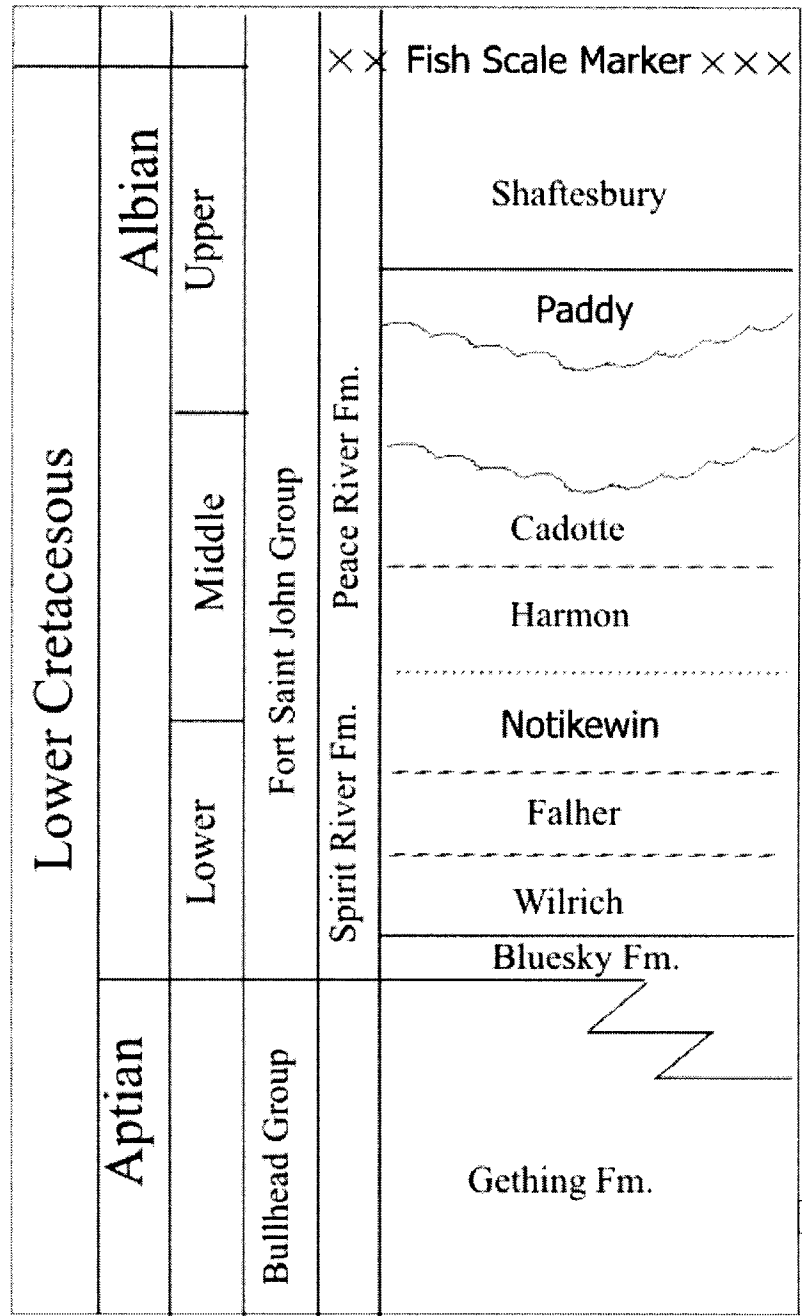


Figure 4.2: Generalized stratigraphic chart for the Lowermost Cretaceous section of the Deep Basin area studied. Chart is based on the work of Hayes et al. (1994). It indicates the geological timing of the various regional geological units. The rocks here are sampled from the Cadotte member.

That the Cadotte member formed as a high wave energy bar deposit is supported directly by visual examination of an example conglomerate (Figure 4.3) and a sandstone (Figure 4.4) from two wells in the region. The conglomerate with the large rounded clasts is particularly indicative of strong wave action necessary to transport such gravel sized pieces. The rounded clasts are almost entirely composed of siliceous cherts. The source of these cherts, which are often hard and as such are more resistant to erosion, was likely within the older rocks formed during the passive margin stage discussed above that had been uplifted to the west of the foreland basin.

The well logs of Figure 4.2 are typical of the study area. The Cadotte member in this area has a distinct natural gamma-ray radioactivity that steadily decreases upwards to low values. At its bottom, there is a sharp change in the GR values which distinguishes the silica rich Cadotte from the underlying, high-radioactivity Harmon shale. The overlying Paddy member, thought to be formed from eroded Cadotte materials is also more radioactive.



Figure 4.3: Thin section of Cadotte conglomerate sample SB002 (depth of 2403.7 m in 15-29-66-11W6) showing rounded clasts predominantly of chert and quartz. Image acquired using high resolution scanner in back-lit mode at 1200 dpi resolution.

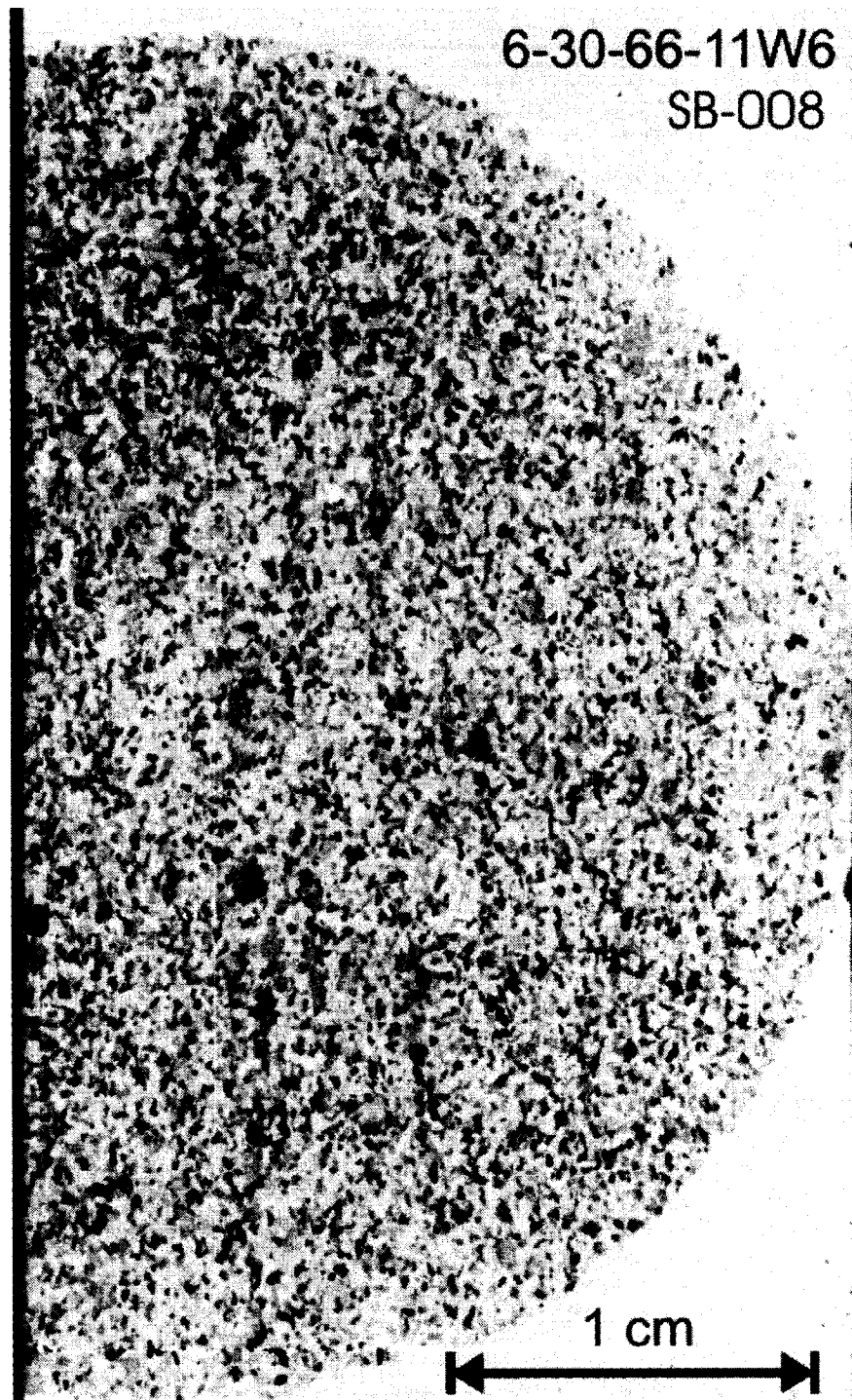


Figure 4.4: Thin section of Cadotte sandstone sample SB008 (depth of 2455.1 m in 15-29-66-11W6).

There are two additional characteristics of the gas saturated sediments in the Deep Basin, including the Cadotte, that are unusual. First, for a given member, the more westerly gas-saturated portions are actually down-dip (i.e. at a lower elevation) from the water-saturated portions of the same contiguous member as indicated in Figure 4.5. Second, the pore fluid, or reservoir, pressure is lower in the deeper gas-saturated zones relative to the equivalent water-saturated zone at the same depth as indicated in Figure 4.6. This is unusual because: 1) water is denser than gas and almost all natural liquid hydrocarbons and as such if allowed to flow will normally lie beneath gas, and 2) the pressure in the gas reservoirs is even less than that in the corresponding water saturated zones and if these are connected one would expect this pressure gradient to equalize over time by pushing the water into the gas zones. The reasons for this situation are not completely known but may be associated with low permeability and capillary forces (Walls et al., 1982; Nur et al, 1980; Cant, 1986).

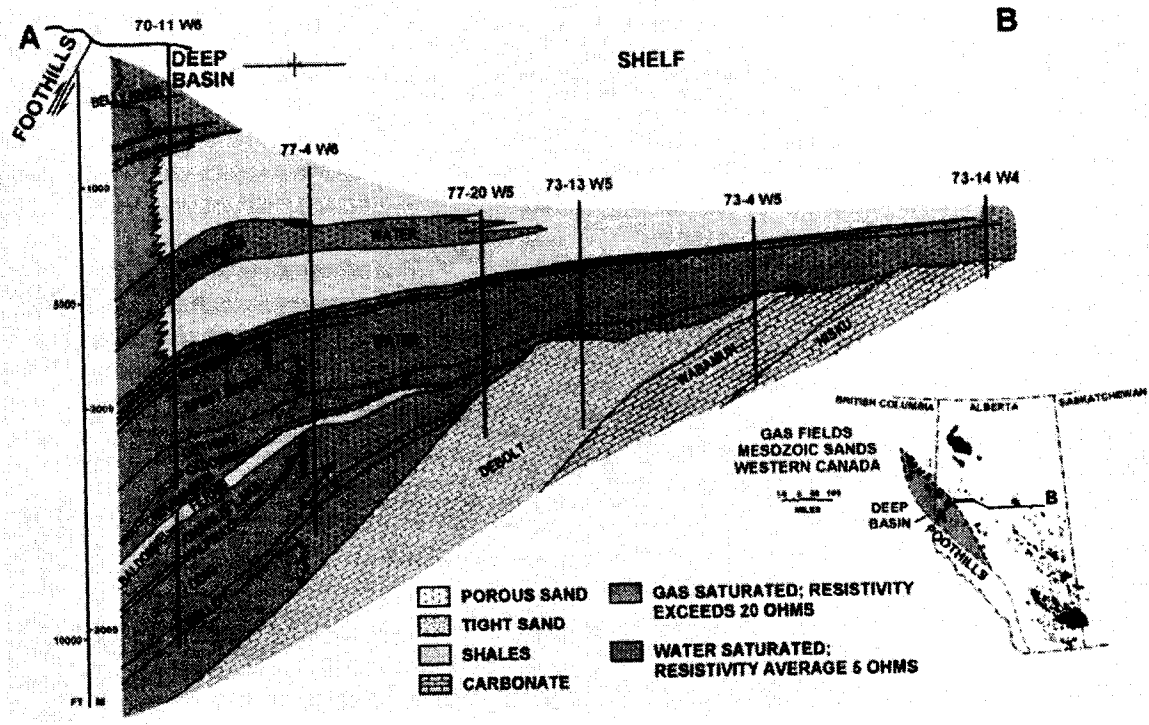


Figure 4.5: Simplified cross section A-B across Alberta through the Deep Basin highlighting the unusual behaviour of water-saturated zones up-dip from gas-saturated zones. Figure from Davis (1984) with permission to use granted by the American Association of Petroleum Geologists.

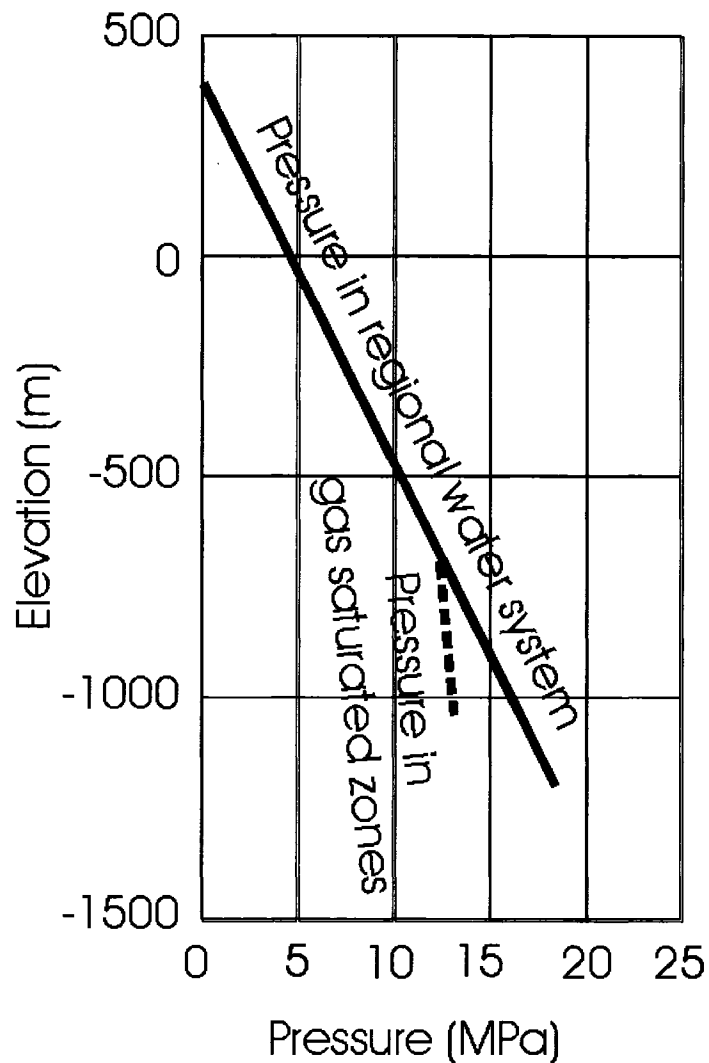


Figure 4.6: Pore fluid pressure in water and gas saturated zones of the Cadotte member as a function of elevation relative to sea-level. Figure is developed after that of Davis (1984) with permission to use granted by the American Association of Petroleum Geologists.

4.2 Core Sampling

Eight representative cores of sandstone and conglomerate from the Cadotte member were obtained at the Core Research Facility in Calgary (Table 4.1). The eight cores are from three wells representing three locations: Township 66 Ranges 9 and 11 West of the 6th Meridian (Figure 4.7). Although eight samples were collected, only four of the samples all from one well are studied extensively due to failure with the first four during velocity measurements as will be mentioned later. The available well logs of natural radioactivity, Compton-scattering gamma-ray density estimate, and P-wave velocity are shown in Figure 4.8 with the Cadotte formation highlighted.

Table 4.1: The well location, lithology and depth of the eight samples

Project Sample ID	Other ID	Sample type	Specific Location	Lithology	Sample Depth (m)
SB004	4P	half core	EOG Wapiti 10-17-66-09W6	Conglomerate	2437.45 - 2437.75 core depth (Core 1, Box 1)
SB005	9P	half core	EOG Wapiti 10-17-66-09W6	Conglomerate	2438.21 - 2438.42 core depth (Core 2, Box 1)
SB002		half core	Cdn Hunter et al. Wapiti 15-29-66-11W6	Conglomerate	2403.7m, (Core box 6/7, 2401-2409.65 m)
SB006	8P	core horizontal plug,	Ulster 6-30-66-11W6	Conglomerate	2450.5 (Core Box 2/8)
SB007	7	core horizontal plug,	Ulster 6-30-66-11W6	Conglomerate	2451 (Core Box 2/8)
SB008	24	core horizontal plug,	Ulster 6-30-66-11W6	Sandstone	2455.1 (Core Box 5/8)
SB009	20P	core horizontal plug,	Ulster 6-30-66-11W6	Sandstone	2457.7 (Core Box 8/8)
SB003		half core	Cdn. Hunter et al. Wapiti 15-29-66-11W6	Sandstone	(Core box 6/7, 2401-2409.65 m)

These cores are from a depth of about 2500 meters and have undergone various degrees of diagenesis. These sandstone and conglomerate are mainly composed of quartz and chert, which have been subject to intense silica cementation (quartz overgrowth development) because of pressure solution along grain contacts (Hutcheon, 1990).

Pressure solution is driven by stress differences and involves dissolution at grain contacts during high stress and precipitation at grain contact on pore spaces under low pressure. This process has greatly reduced the porosity and permeability by filling of material in the pore space and pore throat.

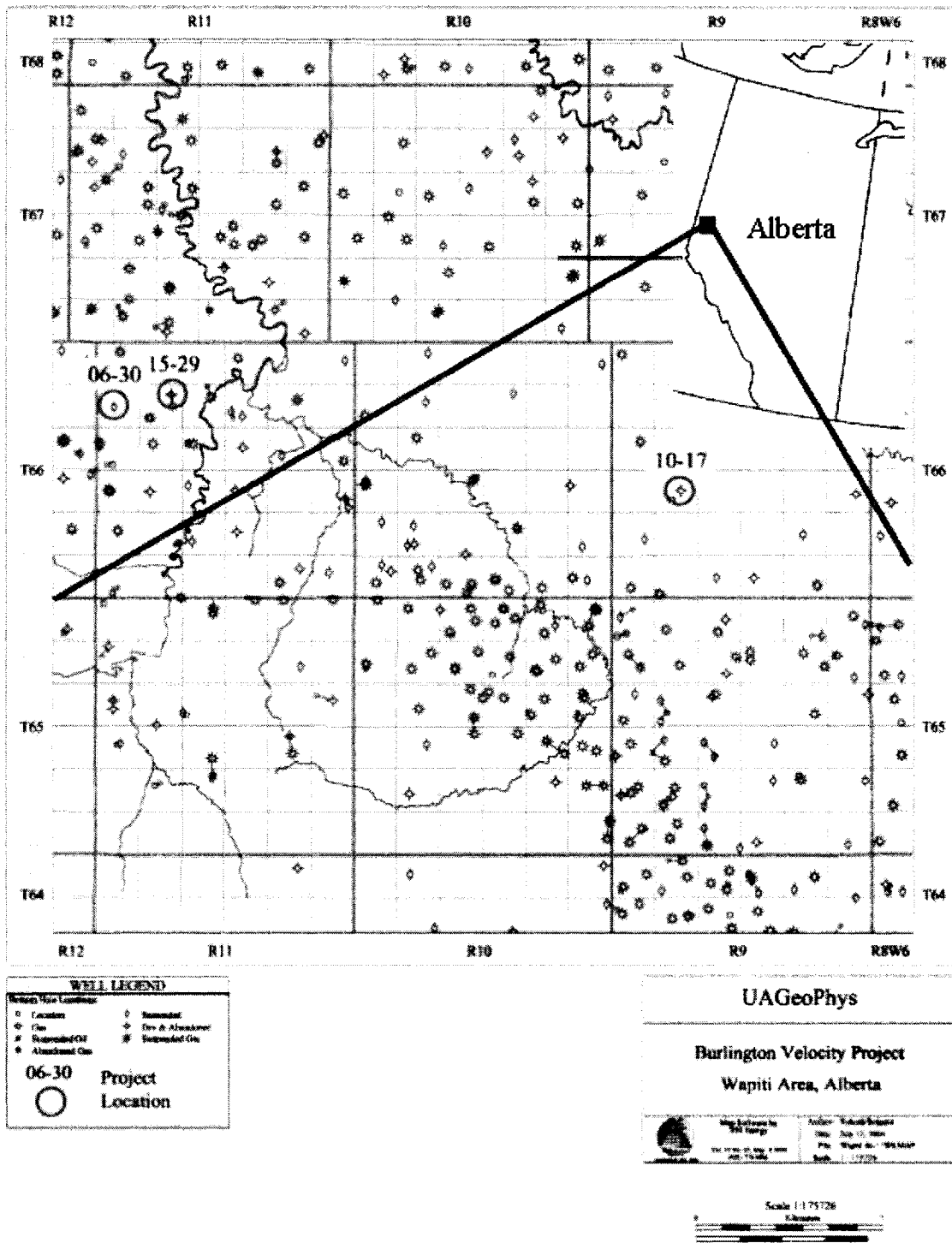


Figure 4.7: Location of the three wells where the eight cores of sandstone and conglomerate are taken from. The red circles represent the three wells where the samples are from.

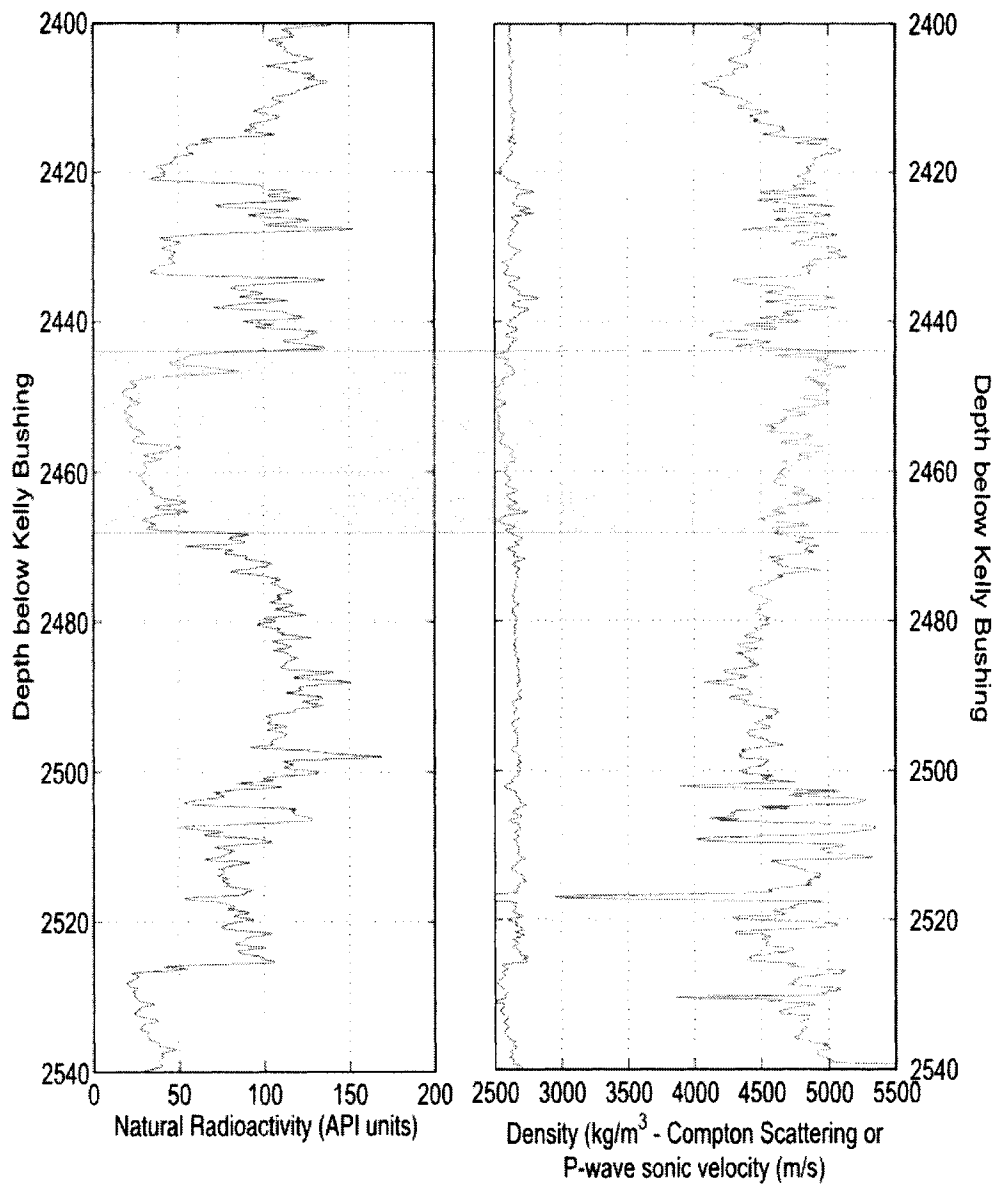


Figure 4.8: Available geophysical well logs for 6-30-66-11W6 (Latitude 54.74111° N, Longitude -119.65222° W) Left Panel: Natural gamma ray intensities (in arbitrary API units) versus depth from the kelly bushing (i.e. the drill rig floor). Right panel, Bulk density as estimated by active gamma-ray log via Compton scattering effect in kg/m^3 and compressional wave velocity in m/s versus depth from kelly bushing.

4.3 Determination of grain density

The grain density is that of the average of the solid portions of the rock only. The grain (or skeletal) density is obtained for porous materials when the volume measured excludes the pores, microcracks as well as the void spaces between grain particles. This is determined using a He Pycnometer (Micrometitics Model MVP-6DC). The Helium Pycnometer is an instrument that operates by detecting the pressure changes resulting from displacement of helium by the sample. That is, in operation a reservoir of He gas at known pressure and temperature is connected to a voided and calibrated volume that contains the porous sample. The combined volume available to the He is the sum of the original reservoir plus the voided volume less that of the solid material of the porous medium. Hence, the skeletal (or grain) volume (V_S) of the sample can be determined from the pressure changes before and after the displacement though the perfect gas law. The solid, or grain, density is then simply the ratio between the measured mass of the solid and this grain volume. The relevant parameters used in determining these grain densities for the samples are provided in Table 4.2.

There are two interesting observations in Table 4.2. First, the ‘grain’ density of all four of the spoiled samples of $2545 \text{ kg/m}^3 \pm 25 \text{ kg/m}^3$ is substantially less than that for the unspoiled samples of $2624 \text{ kg/m}^3 \pm 34 \text{ kg/m}^3$. This is further evidence that the oil inadvertently injected into the first four samples during the tests remained locked as this irreducible oil essentially became part of the volume detected by the He gas. Second, the grain density of the unspoiled samples is close to that for the perfect single crystal value for quartz of 2648 kg/m^3 under standard conditions (Bass, 1994); this correspondence further indicates that quartz strongly predominates the mineralogic composition.

However, as will be seen later there is some evidence for small amounts of much denser dolomite (3795 kg/m^3) in some of the chert grains and even a small amount of this could make the overall grain density in Table 4.2 exceed that of pure quartz as it has done for sample SB009.

Table 4.2: Grain volume as determined from He porosimetry, weight and grain density of the eight samples.

Sample	Grain volume (cm^3)	Mass (g)	Grain density (kg/m^3)
SB002	68.68	175.6	2556
SB003	61.70	158.2	2563
SB004	81.52	205.5	2520
SB005	94.54	240.4	2543
SB006	55.66	145.2	2608
SB007	60.86	158.6	2606
SB008	61.42	161.1	2623
SB009	54.07	143.9	2660

4.4 Bulk density and porosity

Final cutting and sample preparation were carried out at the University of Alberta due to the lack of appropriate cutting equipment for harder rocks at the Core Research Facility. Most of the samples, except for SB002 which was too irregular to cut properly, were formed into right cylinders, with ends made parallel by surface grinding to better than 0.02 mm. The final dimensions and dry mass (i.e. the mass after drying in the vacuum oven below 0.05 torr for 80°C for 24 hours) are given in Table 4.3. The envelope volume was determined from measurements of the cylinder dimensions and is given in Table 4.3:

Table 4.3: The bulk density and the porosities determined using different methods.

	Length (cm)	Diameter (cm)	Dry Mass (g)	Saturated mass (g)	Bulk density kg/m ³	Intrusion volume (ml/g)	ϕ_d (%)	ϕ_s (%)	ϕ_{Hg} (%)
SB002	5.481	-	175.55	-	2559	0.0039	-	-	1.00
SB003	5.553	3.774	158.20	-	2547	0.0220	0.67	-	5.60
SB004	5.725	4.394	205.46	-	2367	0.0238	6.09	-	5.63
SB005	6.473	4.388	240.41	-	2456	0.0293	3.42	-	7.20
SB006	5.308	3.774	145.15	148.55	2445	0.0248	6.27	5.73	6.06
SB007	5.789	3.788	158.58	162.83	2473	0.0273	6.72	6.55	6.75
SB008	5.716	3.810	161.13	164.67	2473	0.0238	5.75	5.43	5.88
SB009	5.066	3.774	143.85	146.25	2538	0.0210	4.59	4.23	5.33

The bulk (or envelope) density is determined for porous materials when pore spaces within the material particles are included in the volume measurement. This requires measures of the dry mass m_{dry} of the rock sample and its ‘envelope’ volume (i.e. the volume of the porous material including solid and void). The bulk, or dry, density ρ_d is simply the ratio of the sample mass to its envelope volume and is given in Table 4.3. The bulk, or ‘dry’, porosity ϕ_d is defined as the ratio of the volume of void space to envelope. Given envelope V_E and solid V_s volumes from Table 4.2 then

$$\phi_d = (V_E - V_s)/V_E \quad (4.1)$$

with the dry porosities calculated using this method are provided in Table 4.3.

A second and similar measure of the porosity is provided by comparisons of the masses of the sample both dry m_{dry} and after full saturation with water m_{sat} . The samples were saturated as part of the laboratory velocity measurements to be described in Chapter 3 and more details will be provided there. Briefly, however, this saturation was carried out by first placing the sealed sample under hydrostatic pressure and evacuating the pore space to a pressure of 0.01 torr (1 torr = 133.322368 pascals). Pressurized water was then allowed to invade the pore space and this was then permitted to equilibrate for many

hours. Since water typically wets the dry mineral surfaces (i.e. is preferentially attracted to) and since the pore space is initially under vacuum, it is assumed that the pore space is then nearly completely saturated with water. The mass m_{sat} of this saturated sample is then measured and the saturated porosity ϕ_s will be given by (assuming no change in volume of the sample before and after saturation):

$$\phi_s = \frac{\rho_d}{\rho_w} \frac{m_{sat} - m_{dry}}{m_{dry}} \quad (4.2)$$

where ρ_w is the density of the water (here assumed equal to 1.000 g/cm³). The saturated porosities are also provided in Table 4.3.

4.5 Mercury porosimetry

The pore structures of the samples are further characterized using a mercury porosimeter (AutoPore IV[®] by Micromeritics) by applying different levels of pressure up to 413 MPa (60,000 psi) to a sample immersed in mercury (Brakel, 1981). The pressure required for the mercury to intrude to the pores increases with the decreasing pore size. The mercury moves into the pores of the sample when pressure increases, and this is called intrusion. Intrusion of pores with different size happens at different pressures.

Mercury porosimetry is based on the capillary law governing liquid penetration into small spaces. For a non-wetting liquid like mercury, the penetration can be expressed by the Washburn equation on the assumption that all pores of the material are cylindrical and connected (Washburn, 1921). The pores in the real world are irregular and are rarely cylindrical; however, this equation is assumed to provide a practical description of pore structure. The Washburn equation can be expressed as:

$$D = -\frac{1}{P} 4\gamma \cos \phi \quad (4.3)$$

where D is the pore diameter, P is the applied pressure, γ is the surface tension of mercury (483.5 dyne/cm = 0.483.5 N/m at 25 °C) (Nicholas et al, 1961) and ϕ is the contact angle of Hg (140°). Figure 4.9 shows that the smallest pore size (~3 nm) that can be invaded using the Hg porosimeter is limited by the peak pressure of 413 MPa.

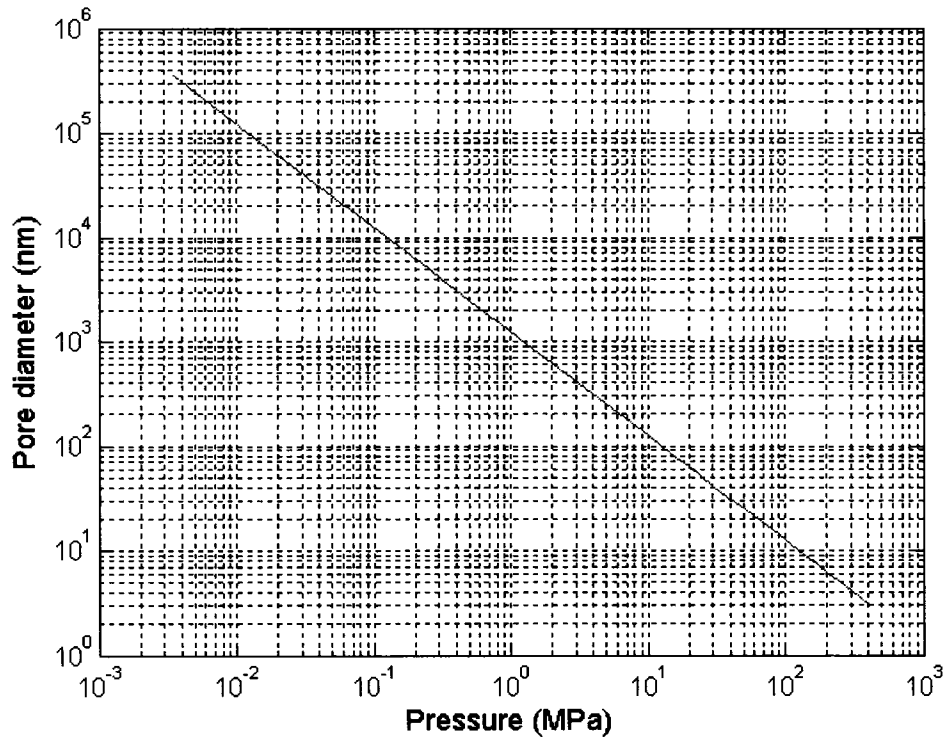


Figure 4.9: The pore diameter versus the corresponding intrusion pressure curve. The pressure required for the mercury to intrude into the pores increases with the decreasing pore diameter.

More accurately, D is really a measure of the pore throat dimensions which the pressure must overcome in order to push the Hg through. The cumulative volume of mercury $V_{Hg}(P)$ penetrating the pores is measured progressively as a function of applied pressure. The pore structure of a material can be estimated by this P-V curve. During

analysis of a sample, the pore size corresponding to each pressure point is calculated from the volume of mercury filled in these pores when the pressure is increased. Taking the derivative dV_{Hg} further provides some measure of the proportion of the porosity at a given range of pore dimension D . $V_{Hg}(P)$ was measured to the peak pressure of the Hg Porosimeter and ΔV_{Hg} was subsequently calculated for each sample in this study. The resulting curves are plotted in Figure 4.10-4.17. It is important to note that Sneider et al. (1984) have previously published $V_{Hg}(P)$ curves from a variety of Deep Basin layers including the Cadotte but their porosimeter was limited to a maximum pressure of only 13.8 MPa (2000 psi) which cannot penetrate as small pore dimensions as our current system.

As one of the example, the P-V curve of sample SB007 is shown in Figure 4.15. About 85% of the porosity has been intruded with mercury at pressure 5 MPa. These pores are the relatively larger pores with high cavity to throat ratio. When the pressure increases from 5MPa to 400 MPa, only 15% of the porosity was penetrated in the pores, which represent smaller pores with lower cavity to throat ratio and microcracks. From the incremental intrusion curve versus pressure, we can see that the highest incremental rate happens below pressure 0.01 MPa, which roughly corresponds to a pore size over 0.03mm. The second higher incremental rate is from pressure 0.2 MPa to 5 MPa, which roughly corresponds to a secondary porosity with pore size from 0.13-4.0 μm . Most of these samples have this kind of secondary porosity as demonstrated in the following figures.

The total porosity of the sample can also be estimated on the basis of the cumulative volume of Hg injected. This will not be the total porosity as only the void space of

sufficient dimensions that has been intruded by Hg at the peak pressure will be detected. However, this does provide an additional estimate of the porosity of the rock. Some errors that can arise are that occluded porosity (i.e. that isolated portion not connected in any way to the pore network) will not be included and that some large pores which can only be accessed via small pore throats maybe missed. The Hg porosimeter provides the amount of Hg injected to the pore space as a function of the injection pressure but it reports this in terms of ml of Hg per gram of sample referred to here as the normalized Hg volume V'_{Hg} . This may be converted to the intrusion porosity ϕ_{Hg} via

$$\phi_{Hg} = V'_{Hg} \rho_d \quad (4.4)$$

which is also reported in Table 4.3 using the peak value of V'_{Hg} in the measured porosimetry curves of Figure 4.10-4.17. The second curve shown in Figure 4.10-4.17 is called the incremental intrusion $\partial V'_{Hg}$ curve calculated via:

$$\partial V'_{Hg} = \frac{dV'_{Hg}}{dP} \Delta P \quad (4.5)$$

where ΔP is the increment of pressure. This curve reveals the relative distribution of the porosity that is intruded by pores of a given dimension. Consequently, examination of the curves of Figure 4.10-4.17 is suggestive of the dual porosity mentioned in Chapter 2. The rocks include large (> 1 mm) macroscopic pores which in the conglomerates are easily visible to the naked eye in hand sample examination, as well as microscopic pores that are intruded at pressures above ~ 0.5 MPa which suggest pore dimensions of $< \sim 30$ μm with a decreasing but smooth proportion of pore dimensions down to ~ 3 nm, the minimum pore throat dimension accessed by the U of Alberta porosimeter.

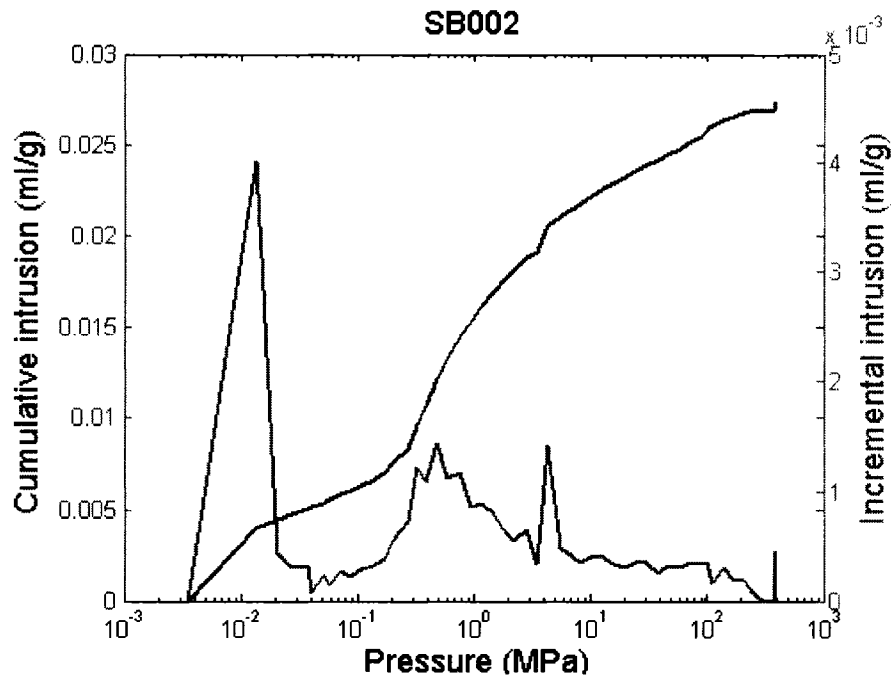


Figure 4.10: Cumulative (blue line) and incremental intrusion (green line) of mercury versus increasing pressure for sample SB002.

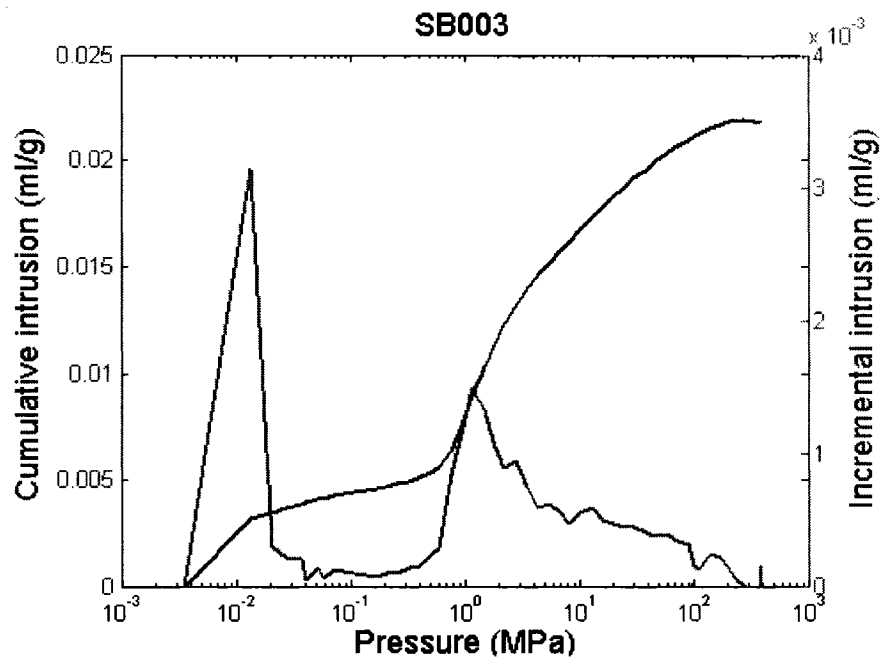


Figure 4.11: Cumulative (blue line) and incremental intrusion (green line) of mercury versus increasing pressure for sample SB003.

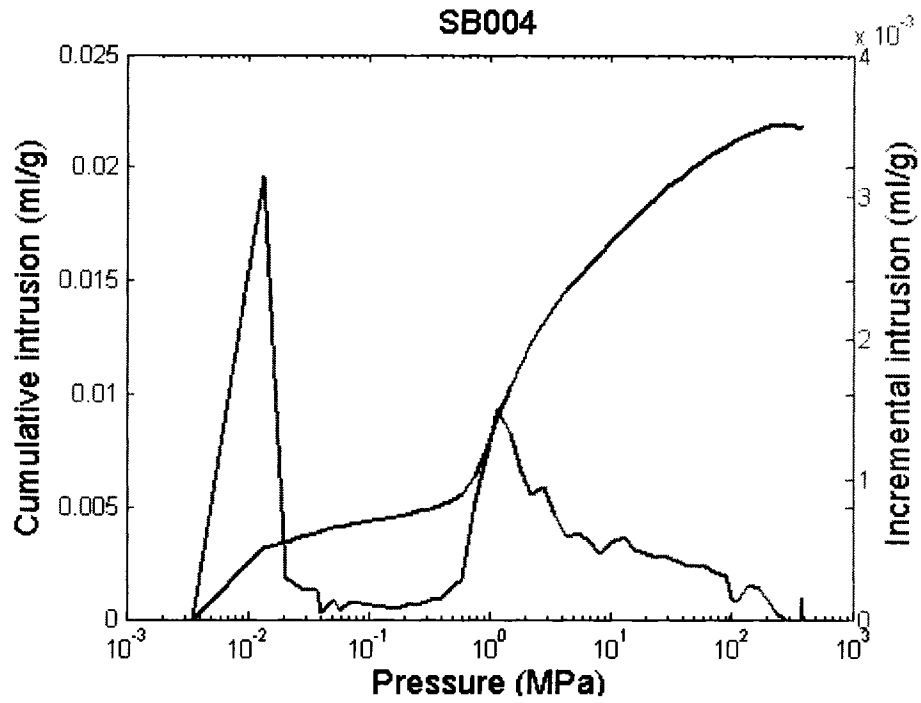


Figure 4.12: Cumulative (blue line) and incremental intrusion of mercury versus increasing pressure for sample SB004.

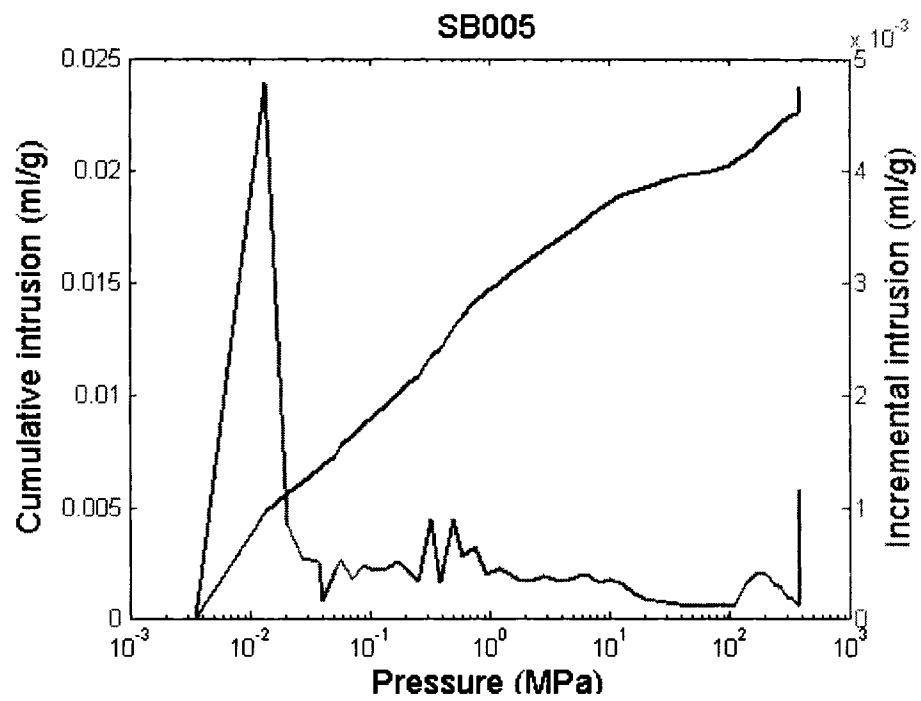


Figure 4.13: Cumulative (blue line) and incremental intrusion (green line) of mercury versus increasing pressure for sample SB005.

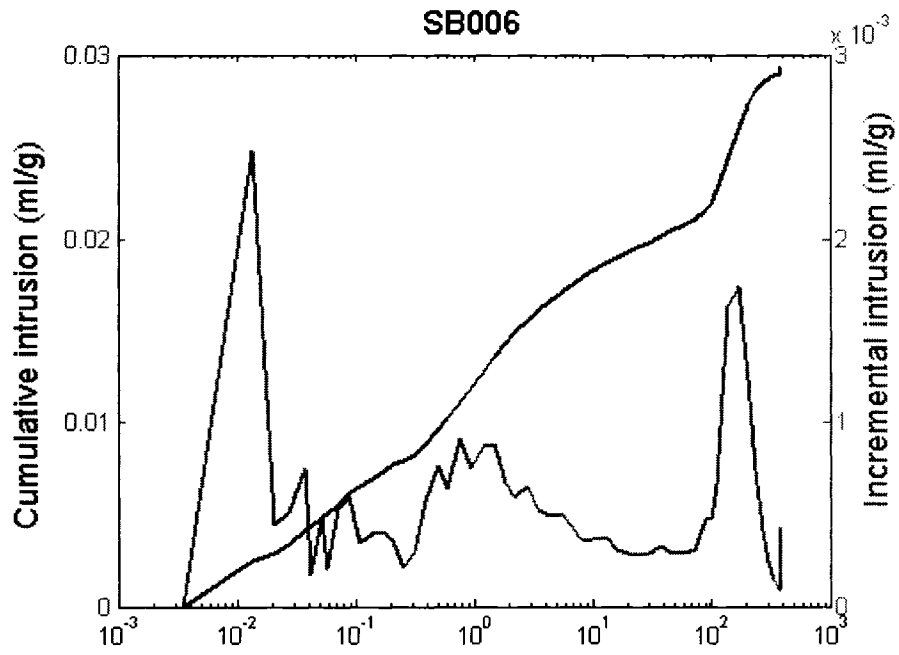


Figure 4.14: Cumulative (blue line) and incremental intrusion (green line) of mercury versus increasing pressure for sample SB006.

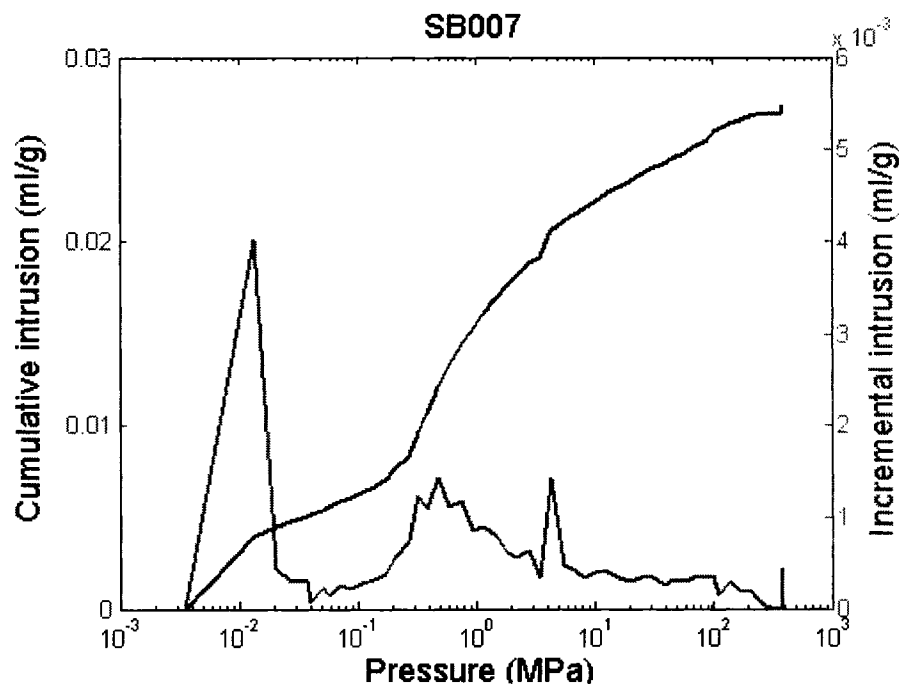


Figure 4.15: Cumulative (blue line) and incremental intrusion (green line) of mercury versus increasing pressure for sample SB007.

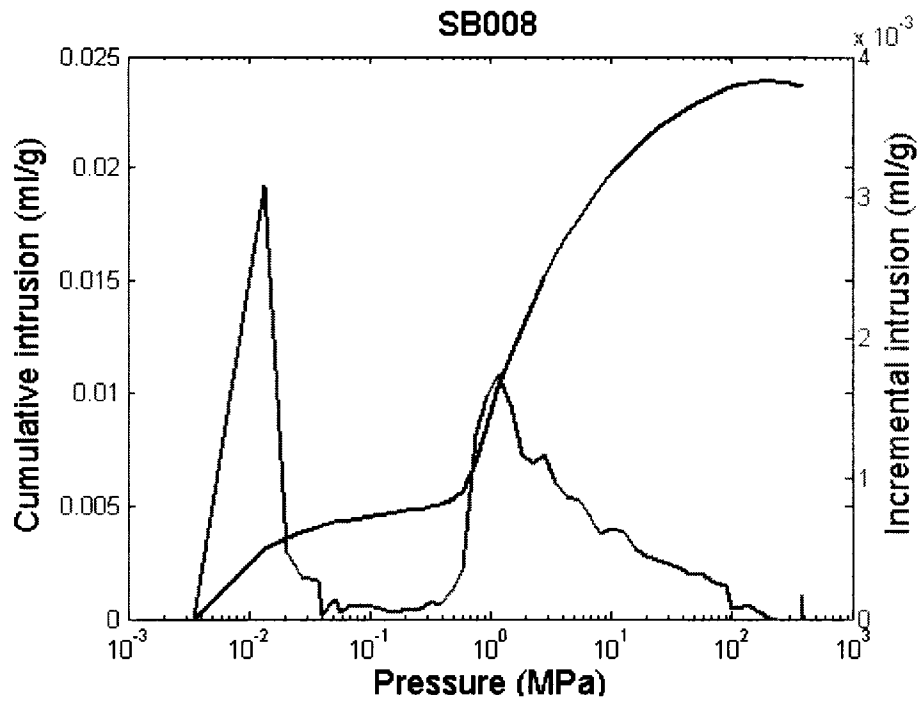


Figure 4.16: Cumulative (blue line) and incremental intrusion (green line) of mercury versus increasing pressure for sample SB008.

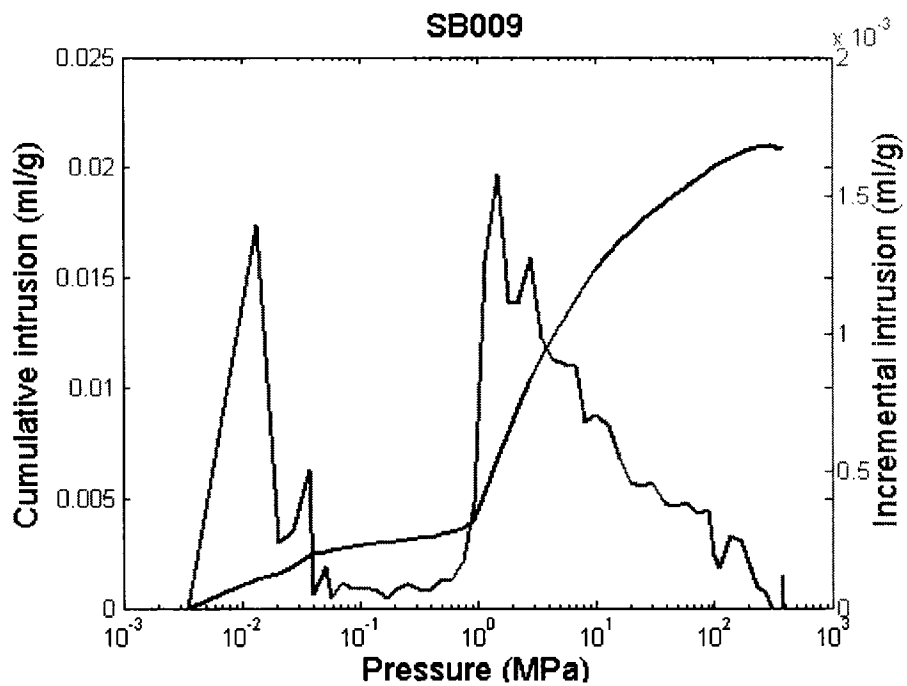


Figure 4.17: Cumulative (blue line) and incremental intrusion (green line) of mercury versus increasing pressure for sample SB009.

4.6 Optical thin section analysis

Thin sections of the eight conglomerate/sandstone samples of the Cretaceous Cadotte Formation were made in the Earth and Atmospheric Science department at University of Alberta. According to the standard petrographic practice, the thin sections were polished to a thickness of 30 μm . The ground and polished films of rock are about 0.03 mm and thin enough to allow light to pass through. The thin sections were taken perpendicularly to the wave propagation direction. The textural characteristics such as the pore space, microcracks and minerals are observed using an optical microscopy. From the optical microscopic observation, the samples appear to be primarily composed of 1) crystal quartz, 2) cryptocrystalline³ siliceous cherts⁴ that may or may not contain accessory minerals such as dolomite, 3) minor amounts of authigenic (i.e. formed in place after the deposition of the rock) clays, and 4) pores spaces with a variety of dimensions.

The grain size ranges from 0.1mm for the small grain size sandstone up to 0.5 cm for the large grain size conglomerate. The samples are moderately poorly sorted, consisting of angular to rounded silica rich quartz, chert. The cement between the grains is caused by water precipitation and forms a well-consolidated rock by binding the grains together. The cement will be looked at in detail in the SEM microphotograph. The pore throat is quite small because of the quartz overgrowth on the grain contacts, this effectively reduces the porosity and the permeability of the sample. The pore space is also filled with some small grains that diminish the porosity.

³ Cryptocrystalline refers to a rock texture that consists of extremely small mineral crystals that are not readily observable even under optical microscopic magnification.

⁴ Cherts are primarily a fine grained rock rich in microcrystalline and/or amorphous SiO_2 formed from the deposition of silica skeletons of microscopic marine organisms such as diatoms. Chert appears in a variety of colors that are dependent on the chemical composition of the material. Chert is usually hard and has a glassy texture, these materials were often used by early man in the manufacture of sharp tools by chipping.

Examples of thin section images (Figure 4.18 and 4.19) of Cadotte conglomerates and sandstones, provided courtesy of Mr. Curtis Lettley of the Dept. of Earth and Atmospheric sciences, illustrate this composition. Additional features that are often found in the Cadotte are also apparent in these illustrative images.

The chert pebbles are distinguished by their motley appearance, particularly under crossed polarized illumination in Figure 4.18c. One of the chert pebbles shows the existence of small single crystals of dolomite (a mineral with chemical composition $\text{CaMg}(\text{CO}_3)_2$) as manifest by the perfectly rhombohedral grains particularly visible in the lower right hand corner of the crossed-polar image of Figure 4.18c. Authigenic crystalline quartz is also apparent in this sample as indicated by the grain with the more uniform appearance on the left side of Figure 4.18b and also appearing in the top-left corner of Figure 4.18c. This quartz, which essentially fills the pore space, was likely deposited by the flow of high temperature waters through the initially porous conglomerate. The chert grains themselves provide an ample supply of silica to make this quartz. One trapezoidally shaped pore, visible at the top but right of centre in Figure 4.18b, is essentially filled with authigenic clays. These clays, however, appear to hold still a noticeable but small porosity as indicated by the blue pore-filling epoxy.

The finer grained sandstone thin sections in 4.19 shows some different features. First, this sample appears to contain a much higher proportion of crystalline quartz, again believed to have been authigenically deposited. Second, the fewer remaining cherts show evidence of porosity as indicated by the blue coloration throughout the grains. Finally, and perhaps of most significance to this study, the plane polarized light images at the two different scales (4.19 a, b) both show the existence of large pores and, in the boundaries

between the mineral and chert grains, thin low aspect ratio, crack-like porosity. This image is in good qualitative agreement with the results of the Hg porosimetry which suggest that the rocks contain the large and the small pore dimension distributions. That is, these pore rocks could be characterized as having 'double-porosity'.

Figure 4.20 shows a high degree of pressure solution as evidenced by the irregular suturing at the grain boundaries. The arrows on the right side of the image point to dark material that has precipitated along the suture (lower arrow) or in a fracture (upper arrow). Quartz cement (Qc) has occluded porosity between grains and appears to have precipitated along a suture (right side of the image). Note the Feldspar in the middle left, which brown areas indicating alteration to clays.

An excellent thin section of sample SB002 (Figure 4.21) shows the internal fractures in a quartz grain. A chert grain is in the upper right quadrant of the image. The most significant observation is that the fractures are lined with relatively small particles (see arrows) that may keep the fractures open, to some degree, at depth. This observation assumes that the small particles have not formed as a result of the coring or handling. A pressure solution boundary (PS) is observed along the upper right boundary of the main crystal. The dominant fracture trend is from bottom left to top right. A probable late, vertical stylotitic fracture with a slightly grayish boundary cuts across the fractures in the middle-right of the picture.

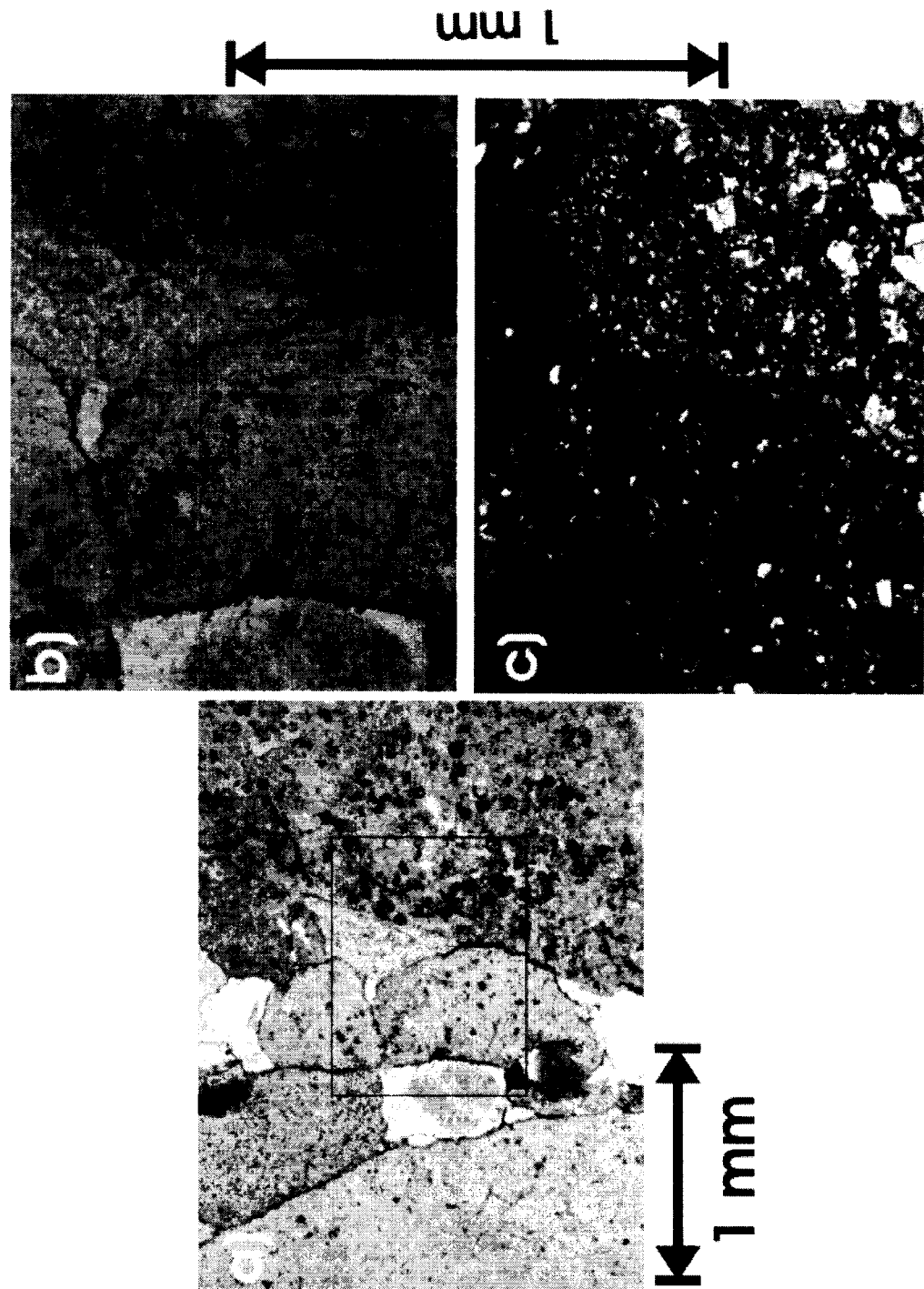


Figure 4.18: Typical thin section images of a Cadotte conglomerate with the pore spaces saturated with blue died epoxy viewed a) under plane polarized light, rectangle represents areas of higher magnification in b) magnified view under plane polarized light and c) magnified and rotated view under cross-polarization.

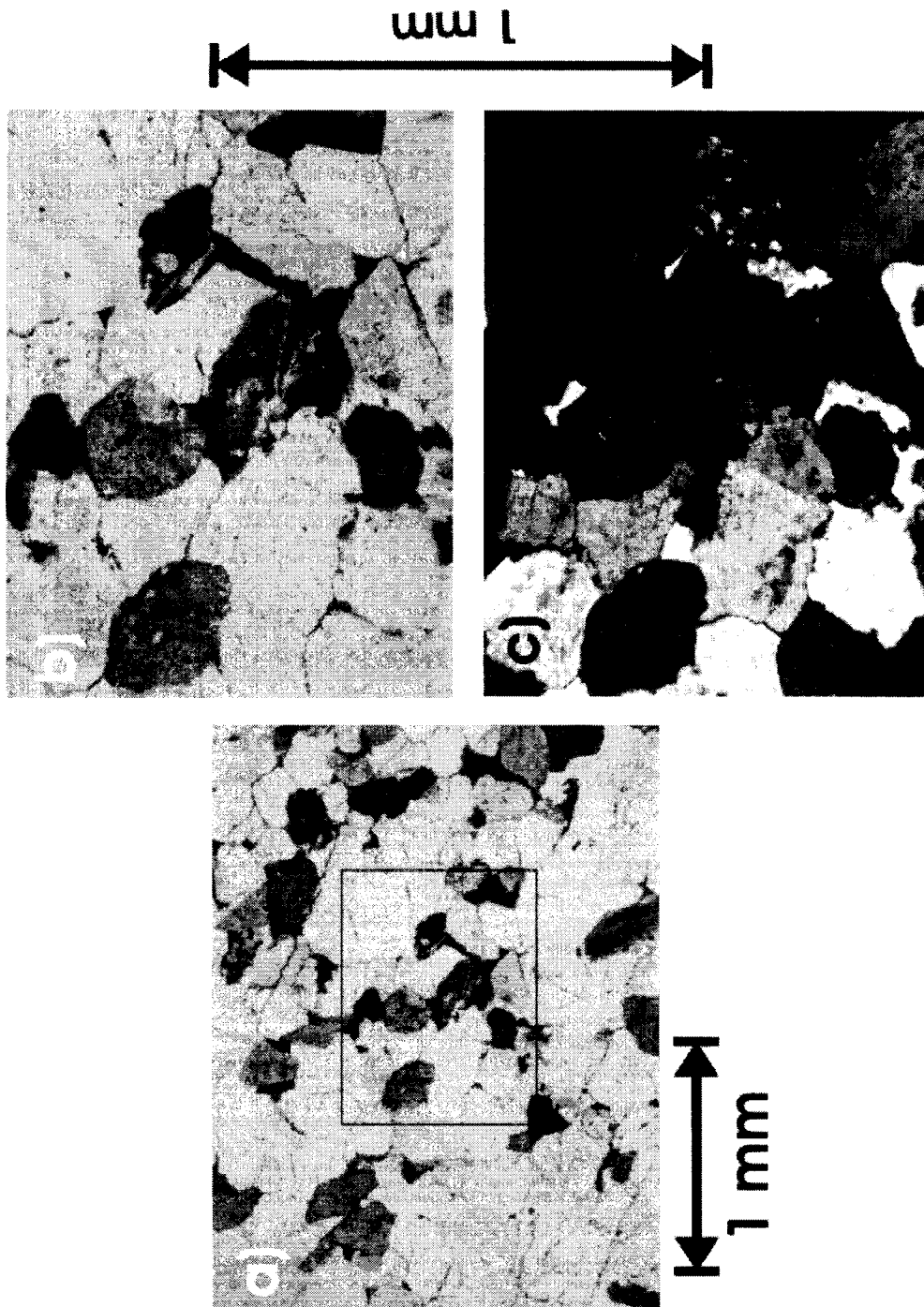
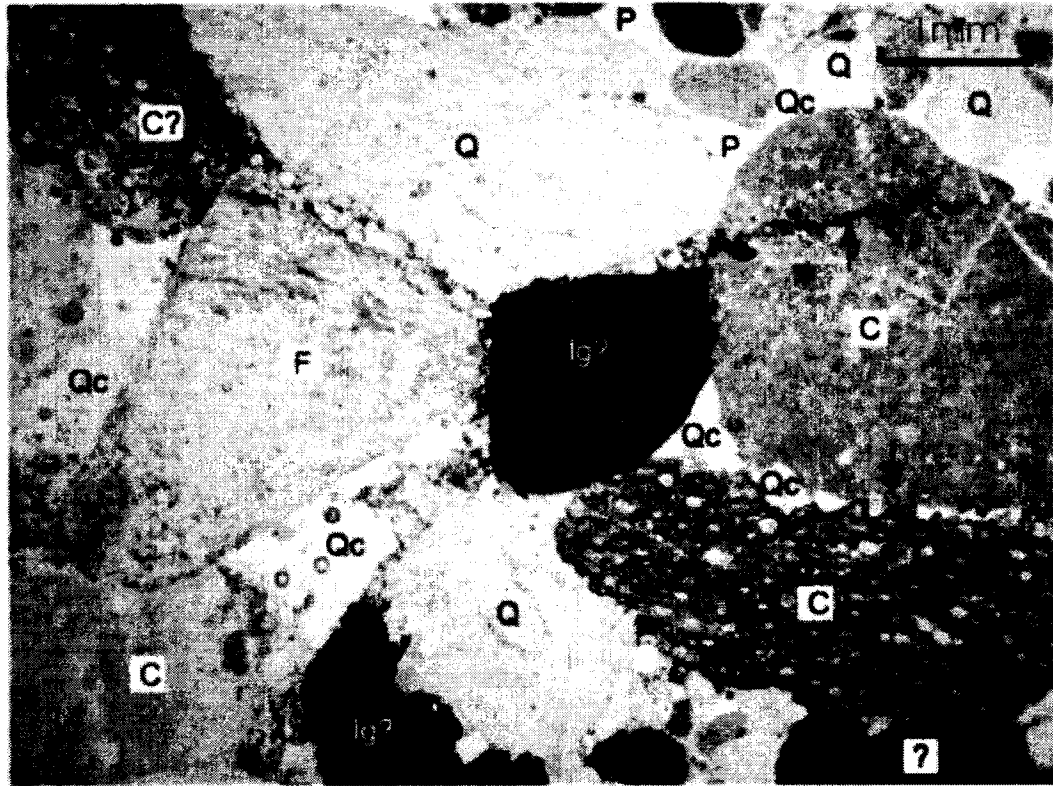


Figure 4.19: Typical thin section images of a Cadotte sandstone with the pore spaces saturated with blue died epoxy viewed a) under plane polarized light, rectangle represents areas of higher magnification in b) magnified view under plane polarized light and c) magnified and rotated view under cross-polarization.



Ig = Igneous fragment; Q = quartz grain; Qc = quartz cement;
 PCQ = Polycrystalline Quartz (metamorphic or Igneous); C= Chert;
 F = Feldspar; P= Porosity

Figure 4.20: The thin section of sample SB005. It shows a high degree of pressure solution as evidenced by the irregular suturing at the grain boundaries.

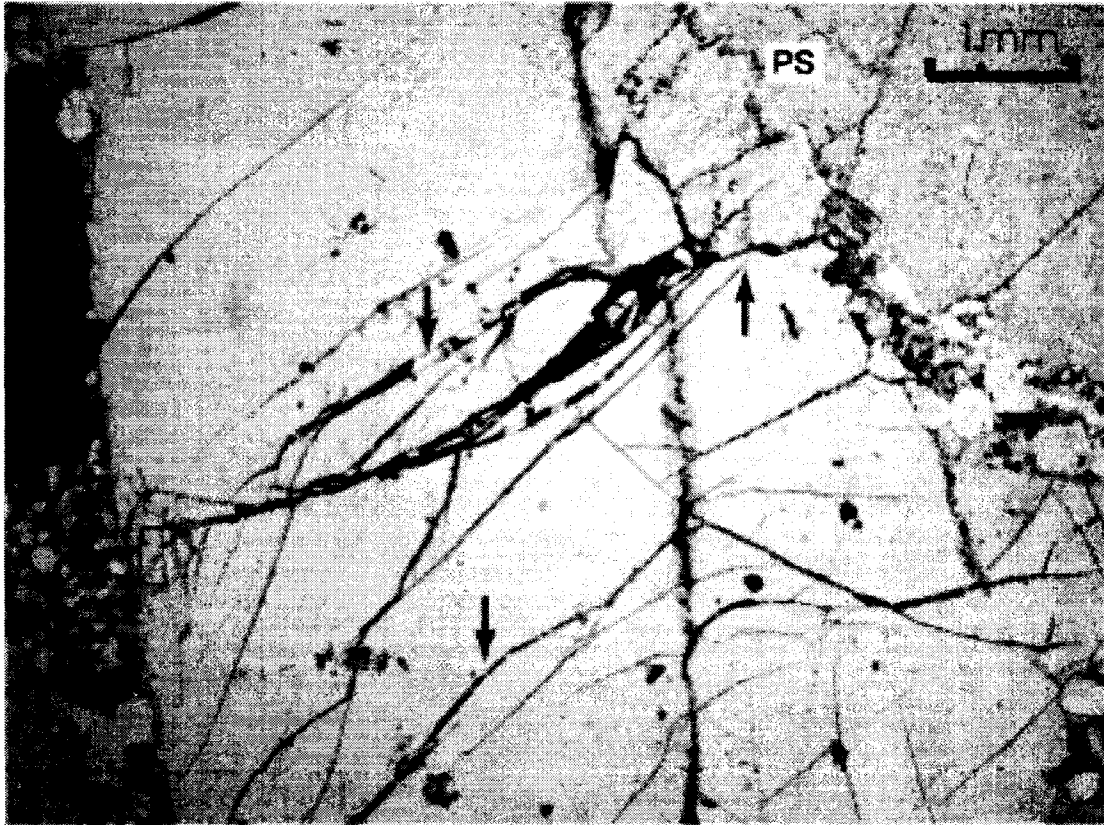


Figure 4.21: A thin section of sample SB002, an excellent thin section showing internal fracturing in a quartz grain.

4.7 SEM/ESEM and X-ray analysis

The Scanning Electron Microscope (SEM) is a microscope that uses electrons rather than light to form an image. By scanning an electron probe across specimen, it can produce very low or high resolution images so that the very closely spaced features can be examined at high magnification. Compositional analysis of a material may also be obtained by monitoring secondary X-rays produced by the electron-specimen interaction. When the beam interacts with the sample, energy is released in the form of radiation over a variety of wavelengths. The portion of radiation in the X-ray part of the spectrum can be collected and plotted as a spectrum. Each peak on the spectrum represents an element because each element has its unique peak, therefore, we can also identify the minerals in the sample through the X-ray spectrum.

In this thesis, the SEM is used for inspecting the surface of the sandstone and conglomerate to look at the grain contact, pore space and grain surface. It must be noted that the material presented on SEM studies here is only a distillation of a much more extensive study carried out by the author in collaboration with Dr. C.D. Rokosh. The preparation of the samples is not difficult because most SEM instrument only require the sample to be conductive. The sample is coated with a very thin film of gold powder to conduct electricity. During SEM imaging, a beam of electrons emitted by an electron gun is focused on a very fine spot of the sample through a series of scan lenses in a vacuum. Near the bottom of the column, a set of scanning coils moves the focused beam back and forth across the specimen. As the electron beam also called primary electrons hits each spot on the sample, secondary electrons are generated from the sample surface. These electrons are then collected and counted by a detector and sent to an amplifier. The final

image is developed from the number of scattered electrons emitted from each spot on the sample. Because an electron beam is used for imaging instead of light waves, all images are rendered black and white. White areas on the image represent intense scattering of the electrons.

The Environmental SEM (ESEM) operates on a similar principal to the SEM, but allows for differential pressure in the vacuum chamber and gun columns, and uses a proprietary gaseous secondary electron detector (GSE) that is capable of imaging in a gaseous environment. Hence, no sample preparation is necessary; the sample can be viewed in its natural environment. In our case, the conductivity of the samples in their natural state was rather poor; so the samples were coated with gold for better imaging. The quartz overgrowth is prevalent on all these samples, which effectively reduces the porosity.

Microscopic examination and X-ray diffraction analysis was performed on the eight sandstone and conglomerate samples. They were also imaged using the Environmental Scanning Electron Microscope (ESEM) and the Scanning Electron Microscope (SEM). X-ray diffraction of the samples was done during SEM imaging. The purpose is to characterize the geological factors that affect rock properties and acoustic velocities of the samples, especially mineralogy of grains and cement, and to observe textural variations, especially grain packing and the presence of fractures. The minerals were labeled on the images while observing the rocks using the X-ray diffraction data. The samples used in the SEM analysis are relatively small (less than 0.5cm^3) compared to that used for ESEM. The ESEM was done in biological science department while the SEM

and X-ray diffraction was done in the Earth and Atmospheric Science department at the University of Alberta.

In the most porous sample SB004, the big silica grains are mostly covered by quartz overgrowth and silica materials (Figure 4.22). Quartz crystals and silica cement are present in the most porous samples (SB004 and SB005). In SB005, which is the sample with the second highest porosity, quartz crystals are viewed as lining the pores along with the silica which has a massive appearance (Figure 4.24). Silica cement and euhedral crystals rarely line the pores of the most porous sample, SB004. In the less porous samples, the pore space is not so obvious and the grain boundaries are not easy to locate because of the silica cement (Figure 4.26 and 4.27). The silica cement between the grains left small space for the pores. The pores are not as obvious as that of sample SB004 and SB005. The micro-porosity is evident in these samples and the micro-pores are well connected, however the absence of the large pore throat will definitely decrease the permeability of the samples. Kaolinite, dickite and illite are the most common clays (Figure 4.23, 4.25 and 4.27). A rough estimation of the collective content of the clay minerals would be no more than 1-2%. Figure 4.28 shows the microcracks in sample SB004. Above the upward-pointing white arrow on the right appears to be braided microfractures, which are likely to be natural rather than induced.

In conclusion, all samples are well indurated with grain locking being a common texture indicating that pressure solution and re-precipitation of silica has occurred. The pores and pore throats in low porosity samples are occluded largely with euhedral quartz crystals along with cryptocrystalline or amorphous silica cement. Note that our X-ray diffraction equipment cannot differentiate between amorphous and cryptocrystalline

cement. Cementation is pervasive in the low porosity samples to the degree that it is difficult to see grain surfaces, even with an electron microscope. The high porosity samples exhibit silica cement along grain contacts and coating some of the grains, however pore walls are largely absent of cement, perhaps due to early migration of hydrocarbons. Clay minerals such as kaolinite, dickite and to a lesser extent illite, are a minor constituent of the total volume of the rock. The kaolinite-dickite ratio (dickite is a high pressure polymorph of kaolinite) has been used in basin analysis studies and to evaluate the timing of hydrocarbon migration. Such research is beyond the scope of this study. Most of the clay particles appear to be fresh with well-formed crystals indicating the clay is authigenic; however a small amount of the clay may be detrital. Microfractures are common throughout the samples. Many of the fractures are fresh and open and likely formed during core expansion, however there are definite indications of old fractures that pre-date coring and thus are present at depth.

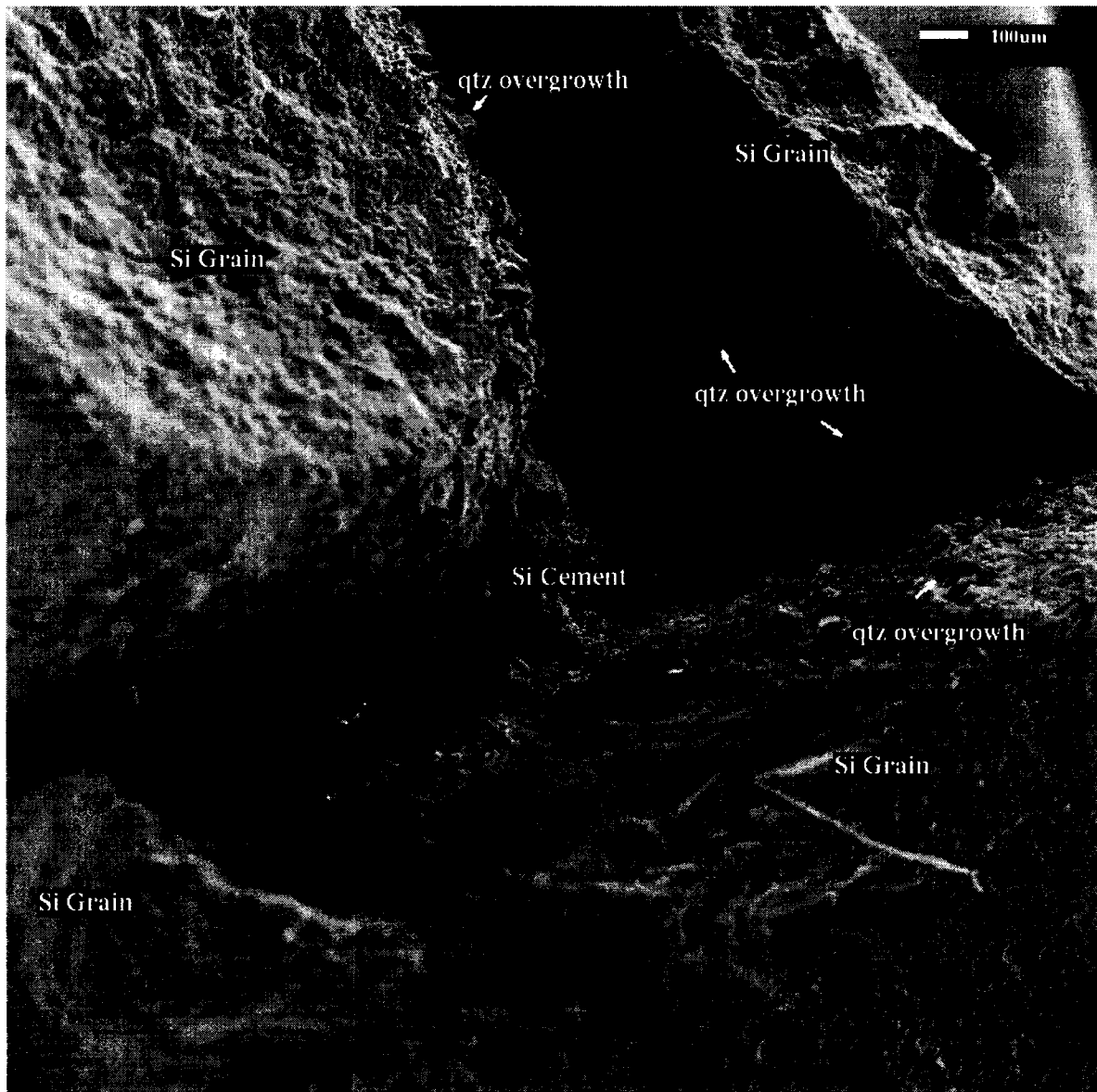


Figure 4.22: SEM image of the highest porosity and permeability sample SB004. There are no non-silica/quartz minerals in this image. Pressure solution of quartz and chert gains would have provided the chemical material for precipitation of euhedral quartz overgrowth crystals and the finer grained silica cement.

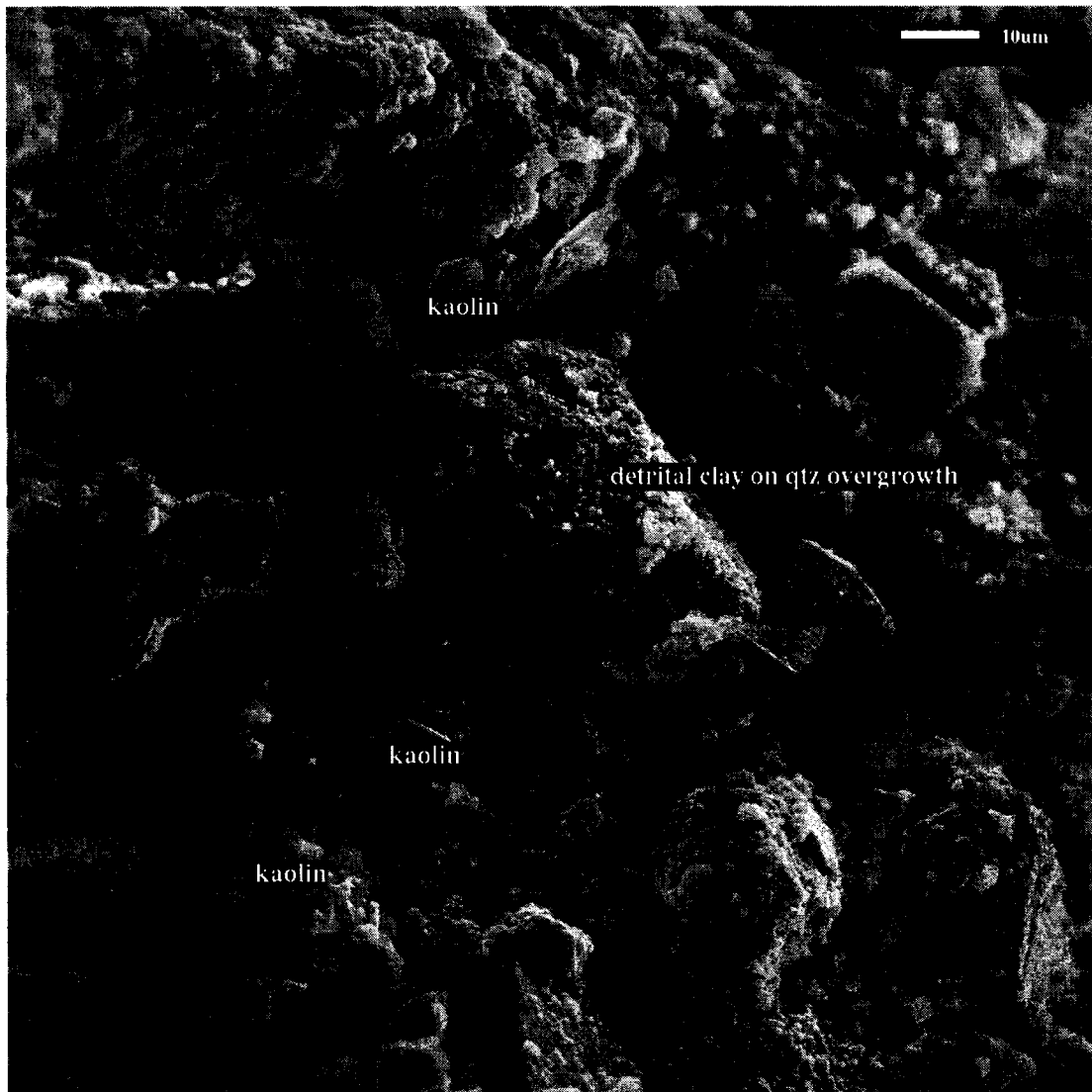


Figure 4.23: SEM image of sample SB004 showing kaolinite on quartz overgrowth. Here, most of the quartz overgrowth is not well-formed euhedral crystals.



Figure 4.24: SEM image of SB005 shows an abundance of quartz overgrowth crystals in a variety of shapes and sizes. Note that the scale of 100 microns (0.1 mm) is the lower size limit of a fine sand grain; hence, some of the overgrowth crystals in this reservoir grow to substantial size and occlude porosity.



Figure 4.25: SEM image of sample SB007 showing a low magnification view of kaolin booklets nestled against fine to medium grained sand. A fracture is evident in the lower left of the image.

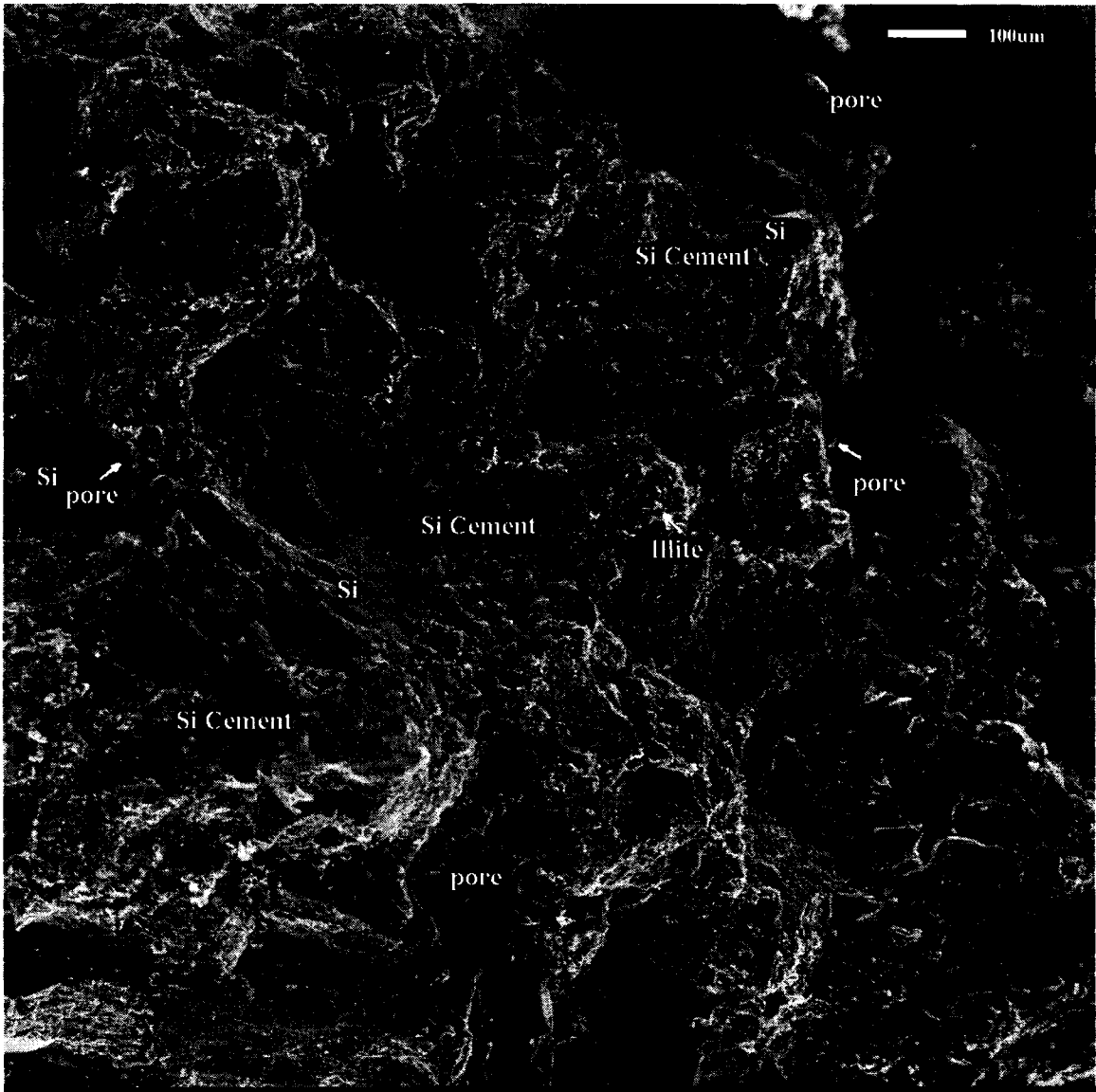


Figure 4.26: SEM image of sample SB008 showing silica cement and illite in tight sandstone along with a few small pores that are not connected

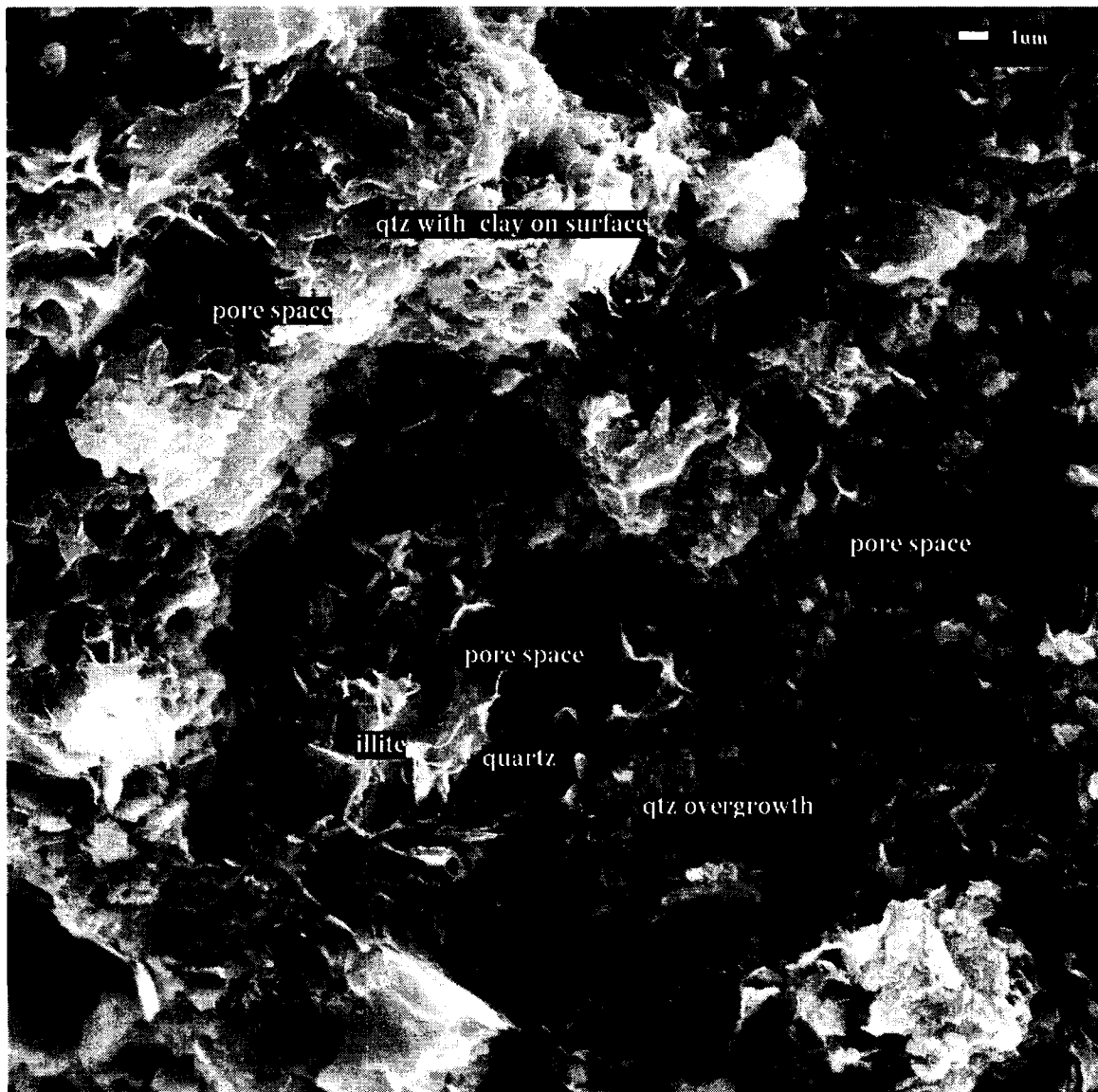


Figure 4.27: SEM image of Sample SB008 showing clay-sized crystals of euhedral quartz overgrowth, with indeterminate white clay, along with illite in tight sandstone. As indicated in the image, microporosity is evident.

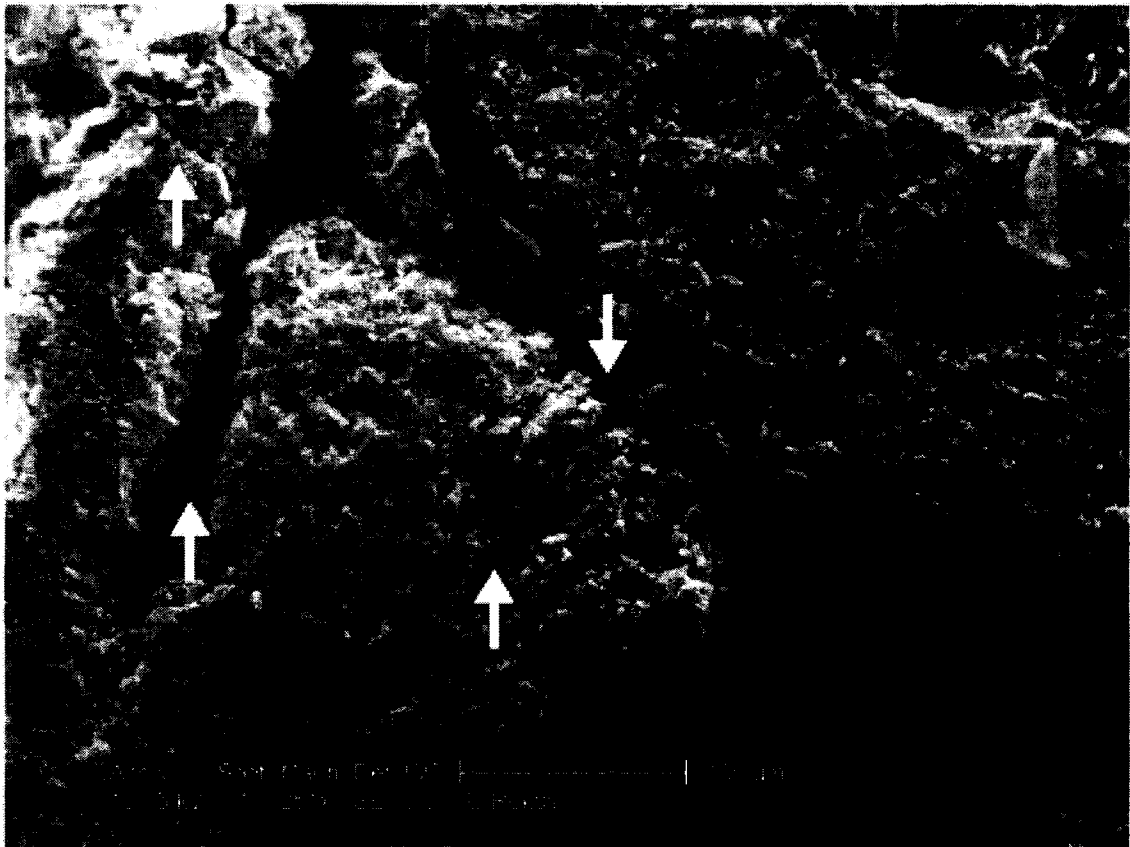


Figure 4.28: ESEM image of sample SB004 showing multiple fractures (white arrows), some of which are open. Above the upward-pointing white arrow on the right appears to be braided microfractures, which are likely to be natural rather than induced.

4.8 Summary

The geological settings of the rocks are briefly reviewed in the beginning of this chapter. The Cadotte conglomerates and sandstones are primarily composed of quartz either in large authigenic crystals that filled the initial pore space or in crypto-crystalline form in the chert pebbles. The porosimetry measurement suggests that secondary porosity which is most likely microcracks and grain boundaries exists in these rocks. They will be flooded with mercury at relatively higher intrusion pressures. Both of the images of thin section and SEM also demonstrate that microcracks exists in these rocks, which only represent only a small portion of total porosity. The SEM also shows that quartz overgrowth and quartz cement constitute most of the materials between the grain contact and on the grains. Some of the quartz overgrowth is covered with clays.

Chapter 5

Experimental results

5.1 Introduction

The P- and S-wave velocities of a series of Cadotte member conglomerates and sandstones are measured as a function of different confining and pore pressure under both vacuum dry, partially saturated, and fully water-saturated conditions. As well, effective pressure influences were studied by making measurements at a variety of constant differential pressures (i.e. the difference between the confining and the pore fluid pressures).

From these velocities, the bulk and shear moduli, Poisson's ratio, and the V_p/V_s ratio were calculated using the equations described in this chapter. In this chapter, some of the raw waveforms of a series of signals under different confining and pore pressure are shown. The pressure dependence of the rock properties such as the compressional and the shear velocities, the bulk and shear moduli, Poisson's ratio and the V_p/V_s ratio were studied. From the known properties of the water and the dry frame properties determined from the experiments, the theoretical values of velocities of water saturated sample were also calculated by Gassmann's equation.

As noted in the previous chapter, the original sealing method used on the first four samples (SB002, SB003, SB004 and SB005) failed and the confining pressure fluid hydraulic oil leaked into the samples during the initial velocity measurements in the

summer in 2004. We tried to clean these four samples with toluene; unfortunately, the hydraulic oil in SB002 and SB003 could hardly be removed because of the small pore geometry and capillary effects. The mass of the samples could not be returned to the original dry mass indicating that the samples retained a substantial amount of hydraulic oil in the pore space. For SB004 and SB005 with big pore size, about 90% of the hydraulic oil in the pores of the samples was removed. The “dry” in the tables of Appendix may mean partially saturated (10%) of hydraulic oil for SB004 and SB005 and completely hydraulic oil saturated for SB002 and SB003 because we initially wanted to measure the samples with water saturation. As such, while we report the results for these samples, we do not believe they are reliable due to the oil contamination.

All of the results for the last four samples in this chapter are measured using the newly updated sample arrangement and sealing method and the newly built pore pressure setup. Most of the samples were cycled up to a peak confining pressure of 60 MPa, which should be close to the values of the confining pressure at depths of 2.5 km. We were conservative in this pressure range initially because in some cases sandstones can be damaged by such pressures; as noted below this was not the case with these materials. Upon completion of the measurements, one sample was taken to a greater confining pressure of 100 MPa in order to provide additional information.

5.2 Example of Raw Waveforms

The full set of normalized P- and S- wave waveforms of dry sample SB007 is given in Figure 5.1. The sample is subjected to pressurization from 5 MPa to 60 MPa and then depressurization from 60 MPa to 5 MPa as noted in the protocols in the previous chapter.

The normalized P- and S- wave waveforms of water saturated sample SB007 at constant differential pressure 30 MPa are given in Figure 5.2, the confining pressure changes with an increment of 5MPa from 35MPa with a maximum confining pressure of 60 MPa. The travel time through the aluminum buffers has been removed from the original waveform. Therefore, the travel time picked on the first extreme of the signal is the transit time through the rock sample. The frequencies of both of the compressional and shear transducers used in this experiment are centered near 1MHz.

From Figure 5.1, we can see that both sets of waveforms display a remarkable reduction of travel time with the increase of confining pressure, which means both of the P- and S-wave velocity increase with effective pressure. This is not unexpected as the velocities, and hence elastic moduli, of such material are known to be highly dependent on the effective stress. However, there is no remarkable reduction of travel time with the increase of confining pressure for the waveforms (Figure 5.2) of the water-saturated sample SB007 at a constant differential pressure of 30 MPa. This is because of the commonly accepted fact that the equal amount of increase of pore pressure almost or more than cancels the equal amount of confining pressure increases. In this sample, the effective pressure is almost equal to the differential pressure, the velocity and hence the transit time is almost constant with the changes of the confining pressure. The waveforms in Figure 5.1 noticeably narrow with the increase of pressure. For each traces of the waveforms at certain pressure, the transit time of the first extreme was picked to calculate the velocity as discussed in the previous chapter.

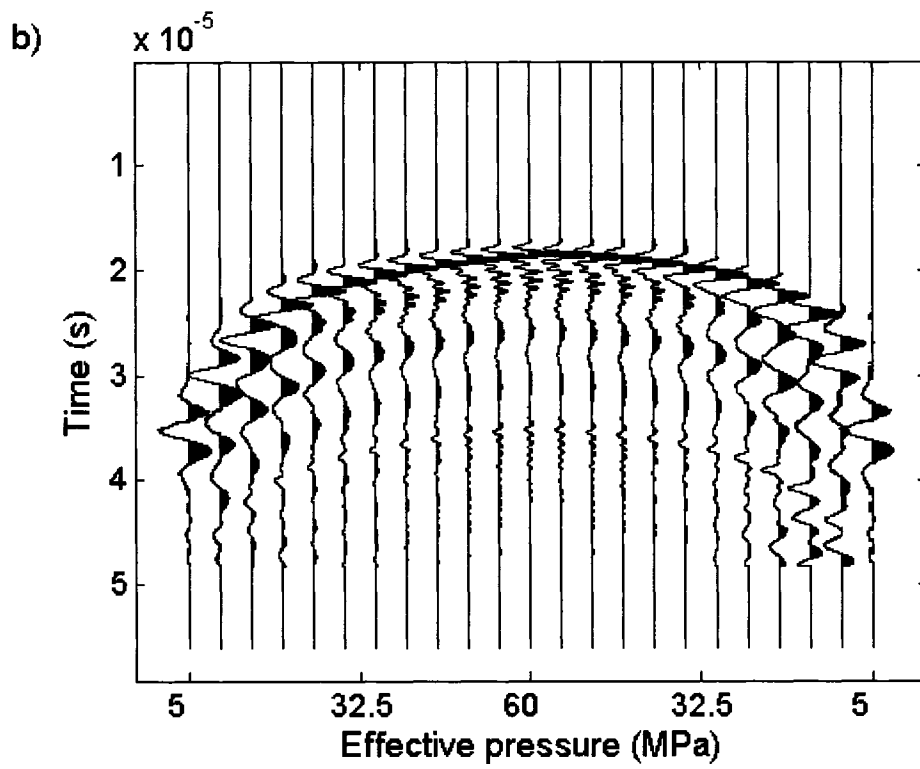
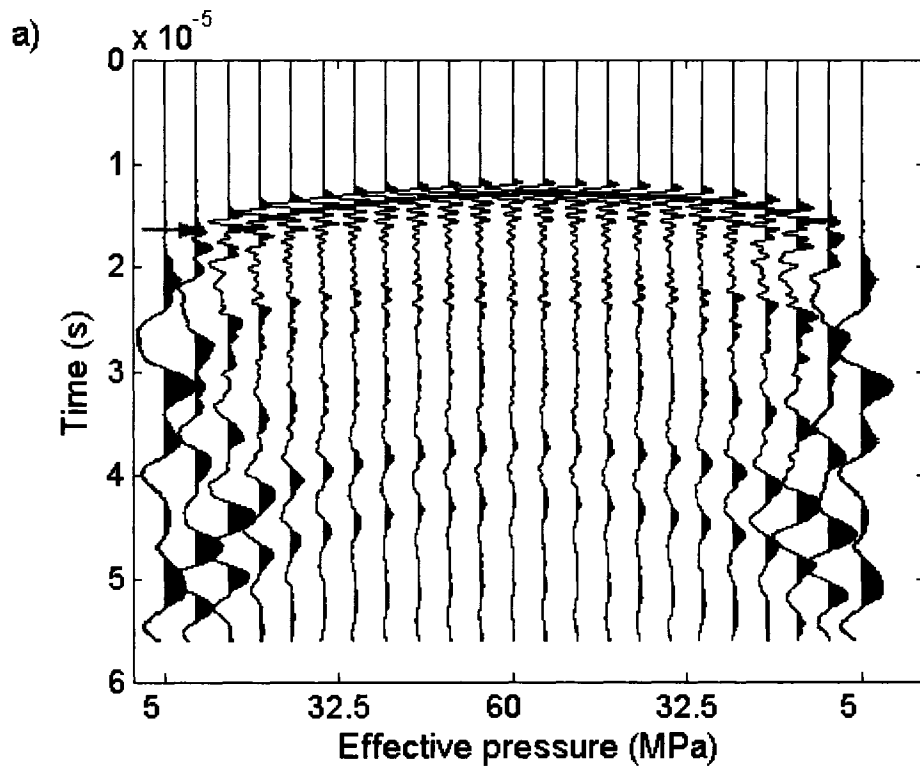


Figure 5.1: The full set of waveform of P-wave (Figure a) and S-wave (Figure b) traces of the dry sample SB007 at different confining pressures.

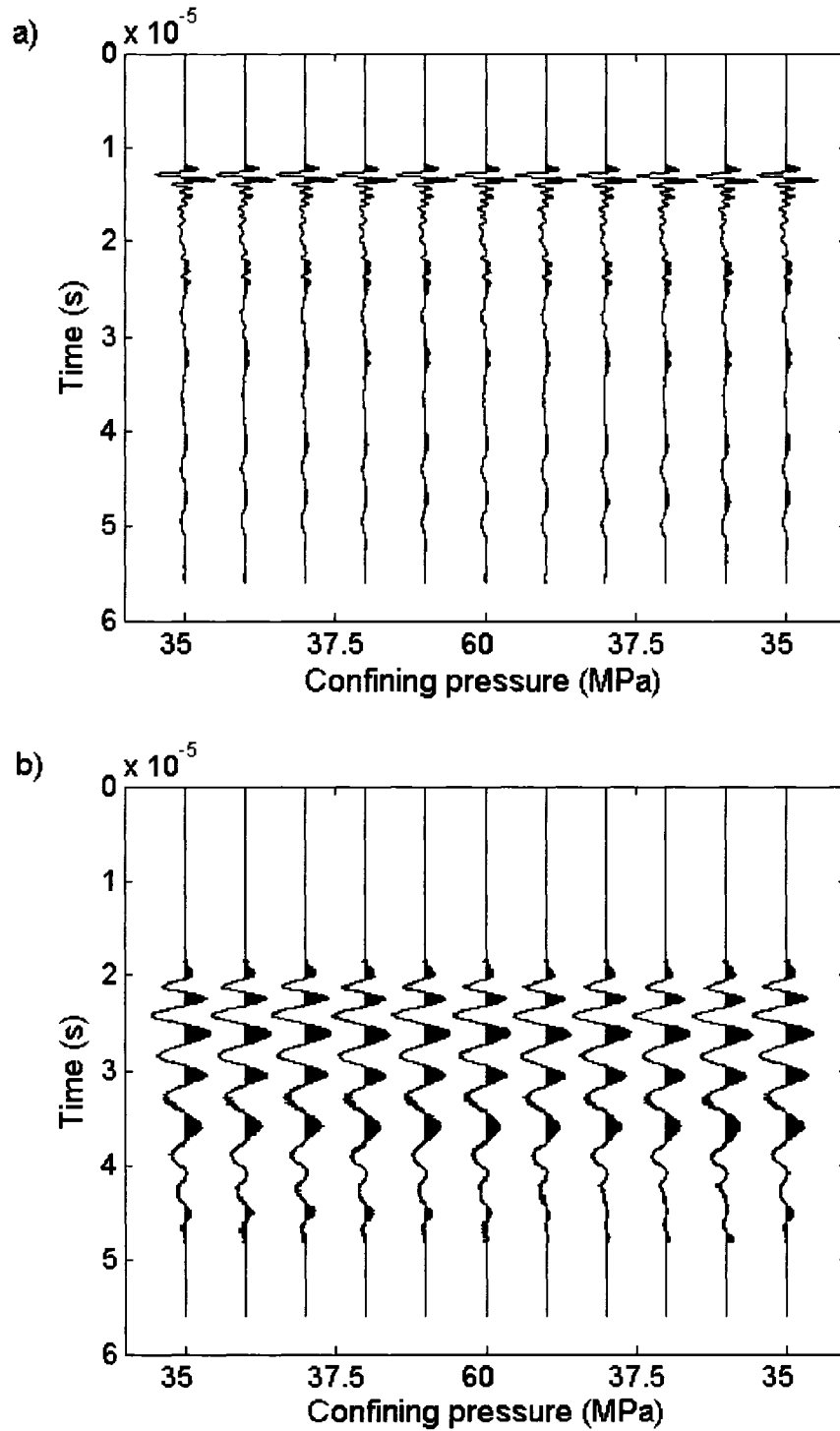


Figure 5.2: The waveform of P-wave (Figure a) and S-wave (Figure b) traces of the water saturated sample SB007 at different confining pressures when the differential pressure was constant at 30 MPa.

5.3 Changes in P-wave and S-wave velocities with pressure

The P-wave and S-wave velocities are measured at three full cycles with progressively increasing peak pressure of 20 MPa, 40 MPa and 60 MPa for the dry sample SB007. The in-situ effective pressure is estimated to be about 45 MPa (under the assumption that in-situ pore gas pressure is ~ 15 MPa, see Chapter 2), so the samples are measured with a maximum pressure of 60 MPa.

As noted, the pressures were cycled up and down three times. In this sample there was little evidence for strong consolidation as the velocities for the up cycles were repeatable. An example of the pressurization for three cycles on sample SB007 (Figure 5.3), which remained vacuum dry throughout the measurement sequence, illustrates a nonlinear increase in both P- and S-wave velocities upon pressurization and normal hysteresis upon depressurization. Notably, the velocity versus pressure curves are highly repeatable upon subsequent pressurization cycles; this suggests the rocks have not been damaged by pressurization. Weaker sandstones, for example, display a substantial consolidation and irreversible hardening upon pressurization; this behavior motivated carrying out the pressurization cycles in the experiment.

The velocities of the sample SB007 during depressurization (Figure 5.3) are a little bit higher than the velocities during pressurization because the micro-cracks are not closed or opened instantly upon the pressure changes. In these experiments, the time interval between pressure changes and signal recording is 15 minutes. The time scale over which the pressure changes in these tests is much shorter than the time scale over which the production occurs in the field. Longer time may allow the sample reach an equilibration of deformation. The velocity observed in the laboratory may differ a little

bit from the velocity observed in-situ. In order to minimize the effect of opening and closing effect of the micro-cracks on the velocities, the following analysis in the next chapter is mainly based on the average velocities of the velocities of the pressurization and depressurization.

From Figure 5.3, we can see that the velocity is highly dependent on the confining pressure. Both of the P- and S-wave velocities increase with confining pressure. At low pressures, the velocities increase sharply because the micro fractures are mostly closed at lower pressures. The velocities are then relatively stable for higher effective pressures. This suggests that the flat low aspect ratio microcracks can have a pronounced effect on the P- and S-wave velocities even though they contribute little to the total porosity.

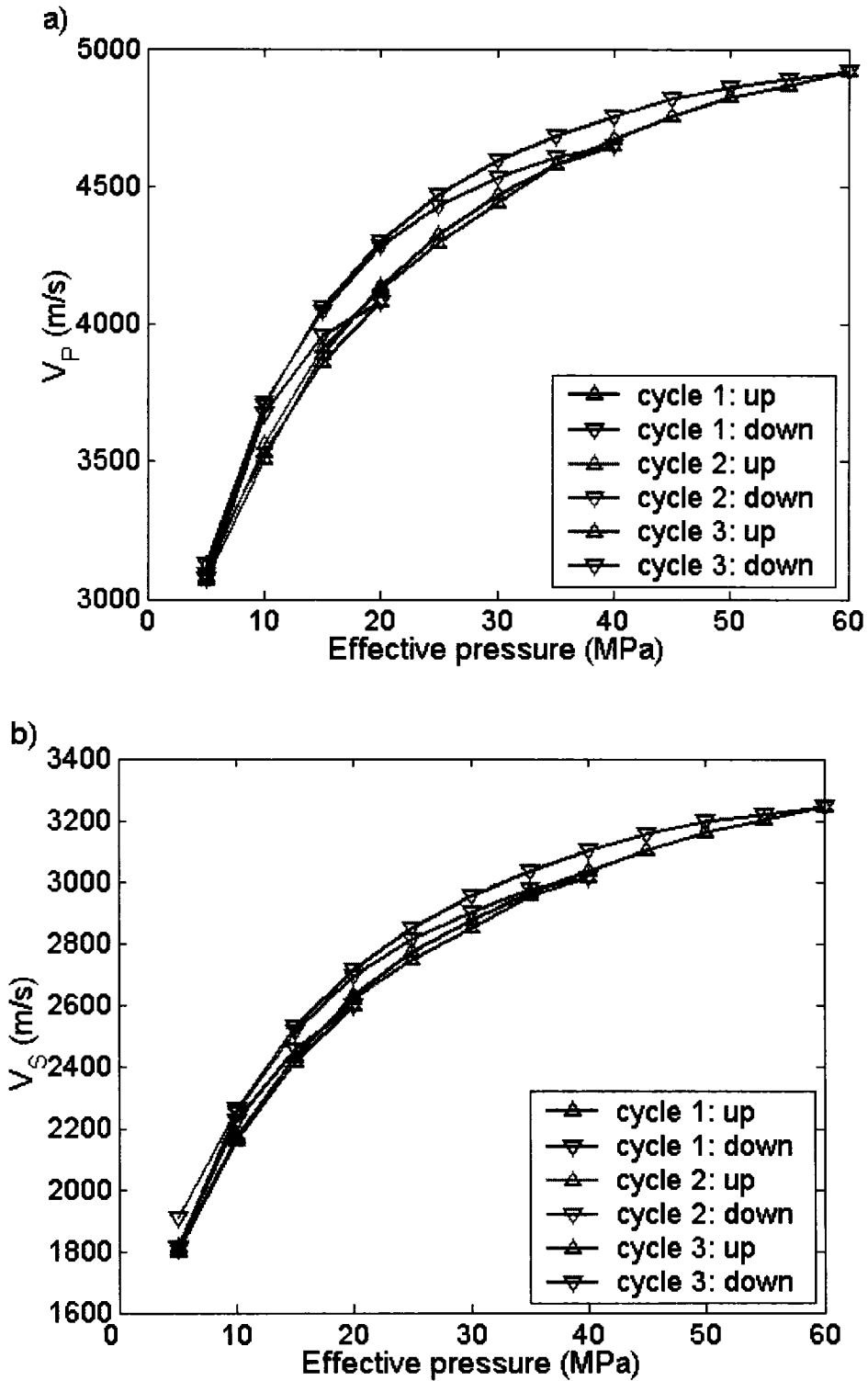


Figure 5.3: The P- (Figure a) and S-wave (Figure b) velocities versus effective pressure curve showing some consolidation upon repeatable pressurization and depressurization less than 60 MPa.

The entire set of velocities determined in the experiments for the 0 to 60 MPa runs only are shown in Figure 5.4-5.7 below. These plots include i) the dry velocity, ii) the fully saturated velocity, iii) the partially saturated velocity, and iv) the velocity calculated on the basis of Gassmann's formula (Eqn 2.13). The dry, or frame, bulk modulus, K_d , is derived from dynamic ultrasonic measurement, the bulk modulus of the mineral (quartz) K_s and the water K_f is are taken to be 40 GPa and 2.25 Gpa respectively (Wang and Nur, 1992; King and Marsden, 2002). The porosity used here are the He pycnometer determined values. There are some general observations from these plots. Many of the implications of these observations are beyond the scope of this present thesis the objective of which was to focus on the implications of the laboratory measurements towards gas exploration in the Deep Basin. However, it is worthwhile pointing out these observations here as they will be important for future work.

1. Both P and S wave velocities are all highly nonlinear functions of confining pressure in all of the tests. This is suggestive of the existence of microcrack porosity and is consistent with the material characterization of Chapter 4.
2. In all cases, the observed fully saturated P-wave velocities exceed those estimated using Gassmann's formula (Eqn. 2.13) at pressures below 60 MPa of confining pressure.
3. In all cases at low confining pressures the partially saturated P-wave velocities are all slightly lower than the dry velocities. This is in agreement with previous work by King and Marsden, 2002 and is thought to be in part related to changes in the surface energy between the quartz grains in the rock

which results in a more compressible medium. The observed and calculated values begin to converge in the two coarser conglomerates (SB006 and SB007) at 60 MPa. A weaker convergence is seen for the two finer grained sandstones (SB008 and SB009). This may suggest that the influence of microcracks is larger in the sandstones consistent with the greater proportion of microcracks as indicated by the Hg porosimetry and as seen in the thin section photographs.

4. In all cases, the saturated observed S-wave velocity at low pressures exceeds substantially that predicted using Gassmann's formulas and that observed for dry conditions. However, the observed and calculated values converge at pressures in excess of 50 MPa.

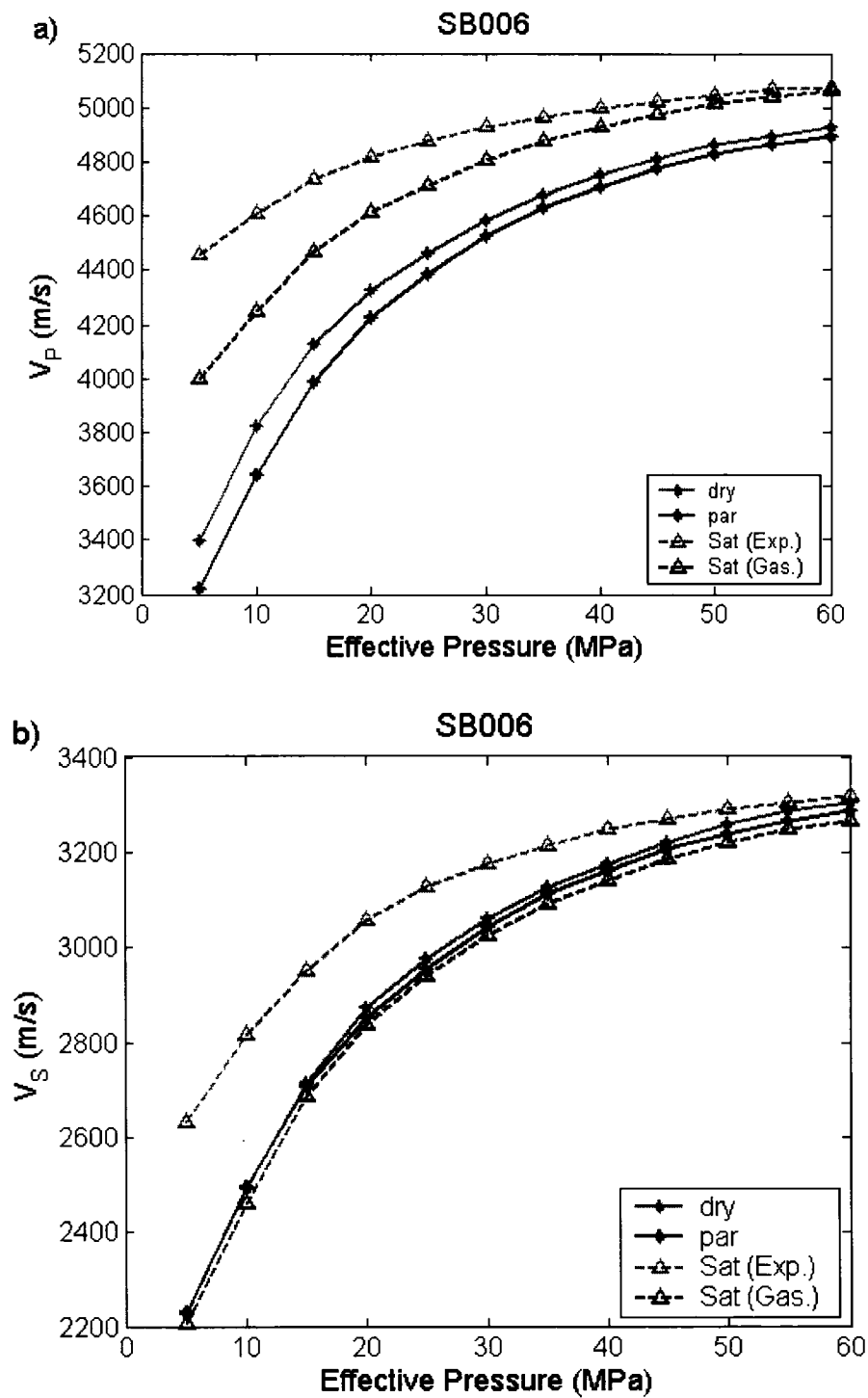


Figure 5.4: The P- (Figure a) and S-wave (Figure b) velocities of dry, partially saturated (~7%), experimentally determined and Gassmann's equation determined water saturated sample SB006 as a function of effective pressures.

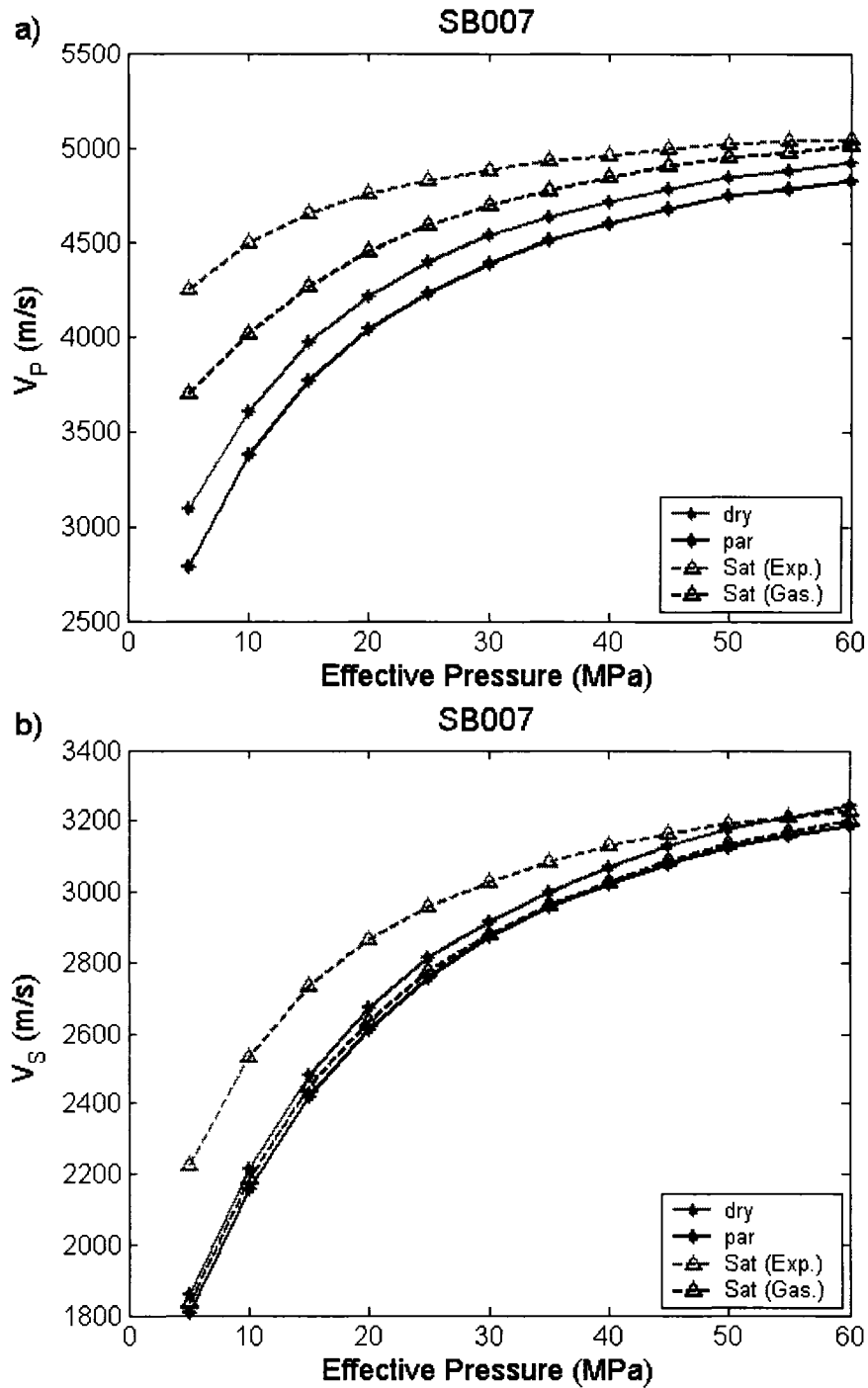


Figure 5.5: The P- (Figure a) and S-wave (Figure b) velocities of dry, partially saturated (~7%), experimentally determined and Gassmann's equation determined water saturated sample SB007 as a function of effective pressures.

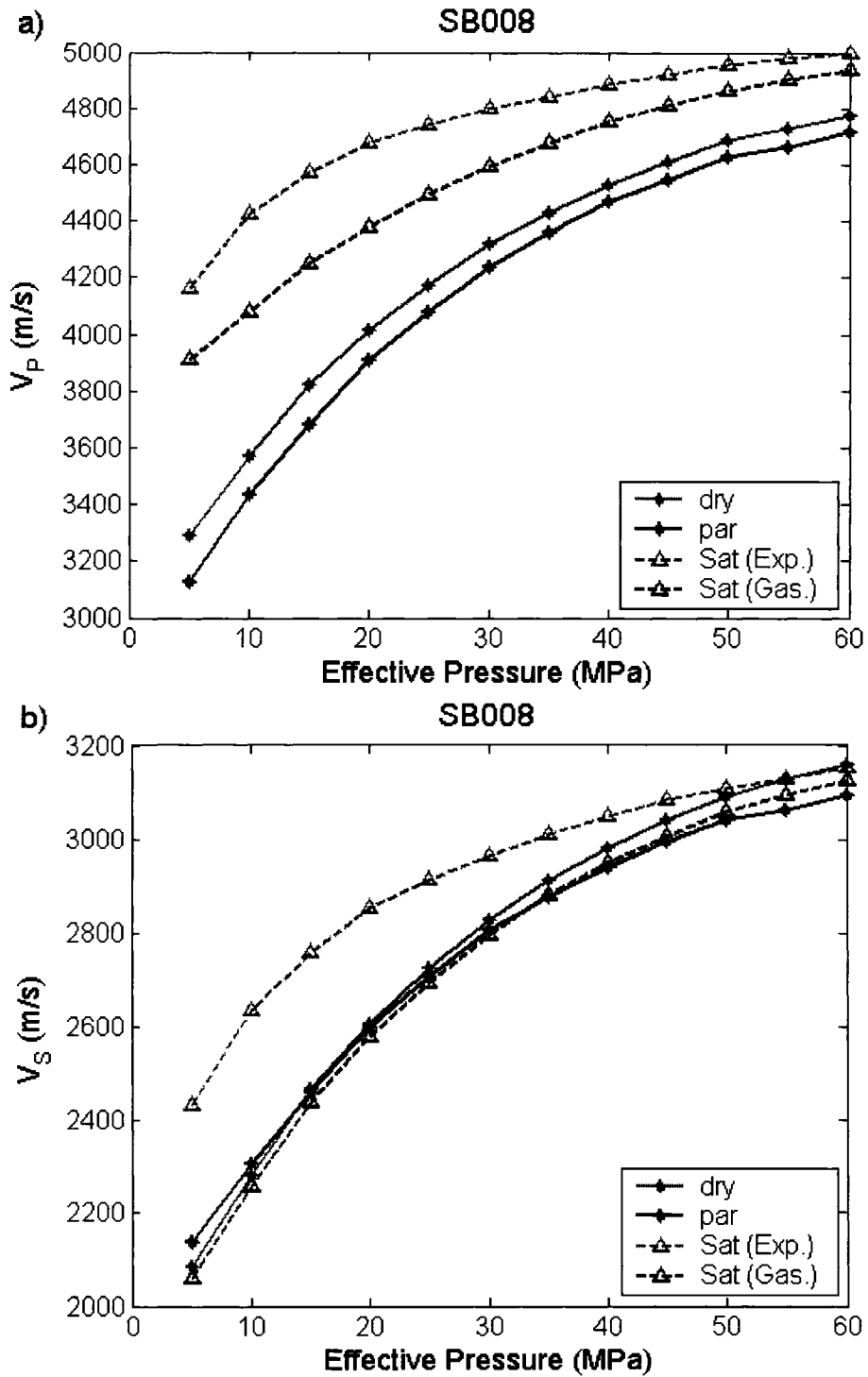


Figure 5.6: The P- (Figure a) and S-wave (Figure b) velocities of dry, partially saturated (~7%), experimentally determined and Gassmann's equation determined water saturated sample SB008 as a function of effective pressures.

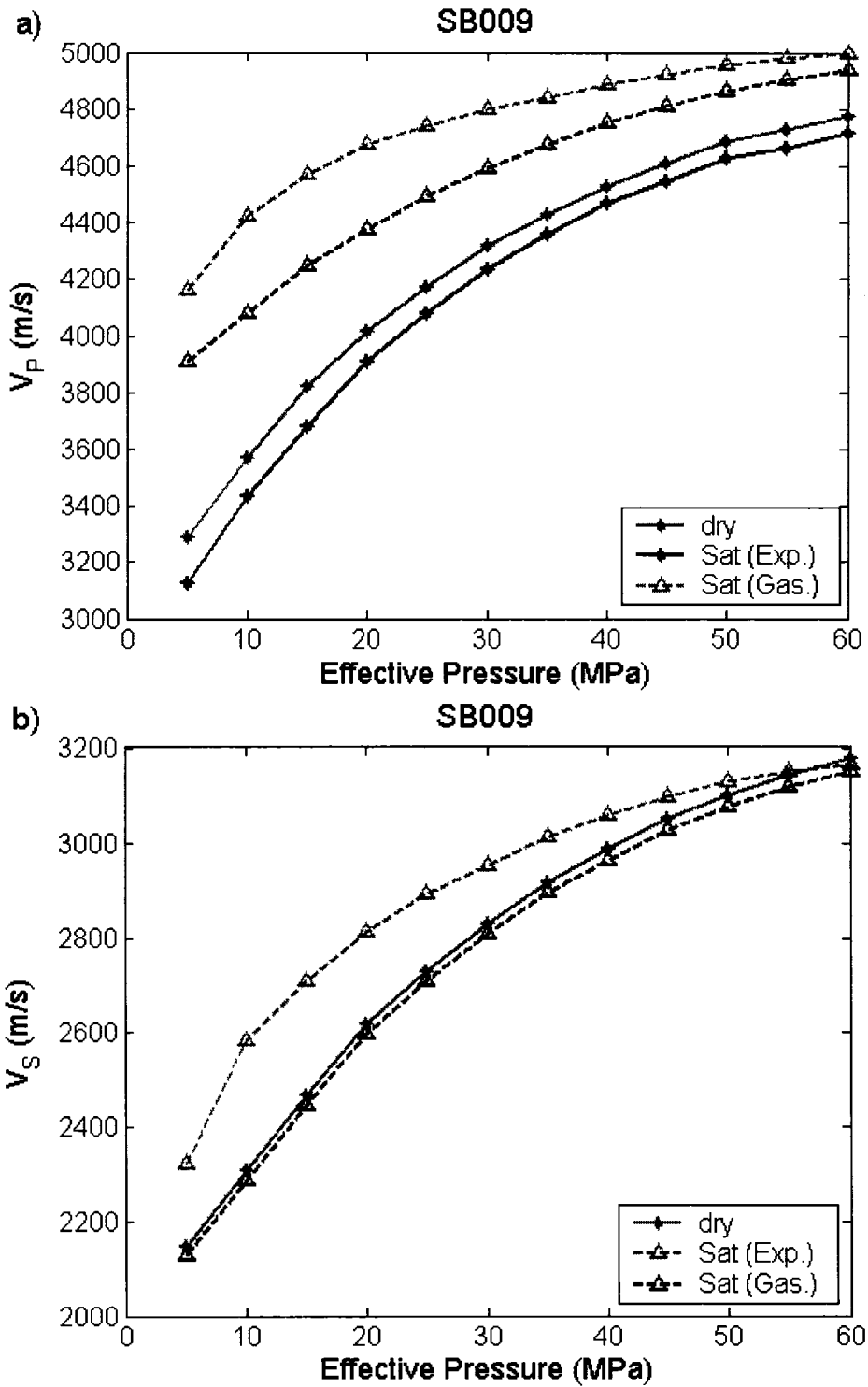


Figure 5.7: The P- (Figure a) and S-wave (Figure b) velocities of dry, experimentally determined and Gassmann's equation determined water saturated sample SB009 as a function of effective pressures.

An empirical relationship between the velocity and effective pressure for a given rock may help us determine the pore pressure and confining pressure from the in-situ velocity measurement. This empirical relationship can also be used to predict the velocity other than the available laboratory data at given pressures. Eberhart-Phillips et al. (1989) first establish an empirical relationship containing a constant, a linear part and an exponential part between velocity and effective pressure for individual rocks. Afterwards, it has been demonstrated by several other authors (Freund, 1992; Jones 1995) that this generalized relationship can give a good fit to the measured velocities. This generalized relationship is shown as follows:

$$V = A + CP_e - Be^{-DP_e} \quad (5.1)$$

where V is the acoustic wave velocity; P_e is the effective pressure; A , C , B and D are the estimated constants using the least-square method for a given rock sample. The best-fit parameters are selected with the least root-mean-square residual in the velocity. The parameter A is not pressure dependent; hence A is representative of the velocity after all the microcracks and small porosity are closed and should only dependent on the mineral type and porosity. C is the velocity slope at higher pressure. B indicates the crack density and the importance of the crack closure. D is related to closing rate of the cracks. A negative or large positive C may not accurately predict the velocity values and give physically meaningless values at high confining pressure (Khaksar et al. 1999). Therefore, Khaksar et al. propose a simplified equation without the linear part to relate the velocity and pressure:

$$V = A - Be^{-DP_e} \quad (5.2)$$

Using equation (5.2), the constant parameters have been calculated for both of the P-wave and S-wave under dry and water saturated conditions and are listed in (table 5.1). Here, A is the pressure independent velocity, which means the velocity at very high effective pressure. The difference between the constant parameters A and B ($A-B$) is the velocity at zero effective pressure.

Figure 5.8 shows the experimental data and best-fit curves of sample SB007, the star, diamond, represent the experimental data for the dry V_P and V_S respectively. The red line and black line indicate the best-fit curves using equation 5.1 and 5.2 respectively. Despite the meaning of the parameters in the equation, the best-fit curves using equation 5.1 fit much better within the experimentally measured values than equation 5.2. The standard deviation of the predicted velocities by equation 5.2 is only around 30 m/s. The standard deviation of the predicted velocities by equation 5.1 is only around 13 m/s, which is very close to the system error of the experimental velocity data that has maximum value of 10 m/s.

In order to understand the predictability of these two equations, we use eleven data points from 5 MPa to 55 MPa with an interval of pressure increase of 5 MPa to predict the best-fit curve, then all the experimental data up to 90 MPa were plotted to check how well these best-fit curve can predict the velocities at higher pressures. The results (Figure 5.9) show that the best curve using both equation 5.1 and equation 5.2 cannot accurately predict the P-wave velocity and the S-wave velocity at higher pressures, although they can give a very good interpolation within the measured velocity data.

Figure 5.10 shows the relationship between density and both of the P- and S-wave velocity data at 45 MPa, the calculated best-fit coefficient A , $A-B$, which represents the

pressure independent velocity and zero stress velocity respectively. Although the predicted parameters using Equation 5.2 are not very precise, the pressure independent parameter A shows an increase with density. However, the velocities at 0 MPa and 45 MPa don't show a clear velocity density trend, because the presence of the microcracks.

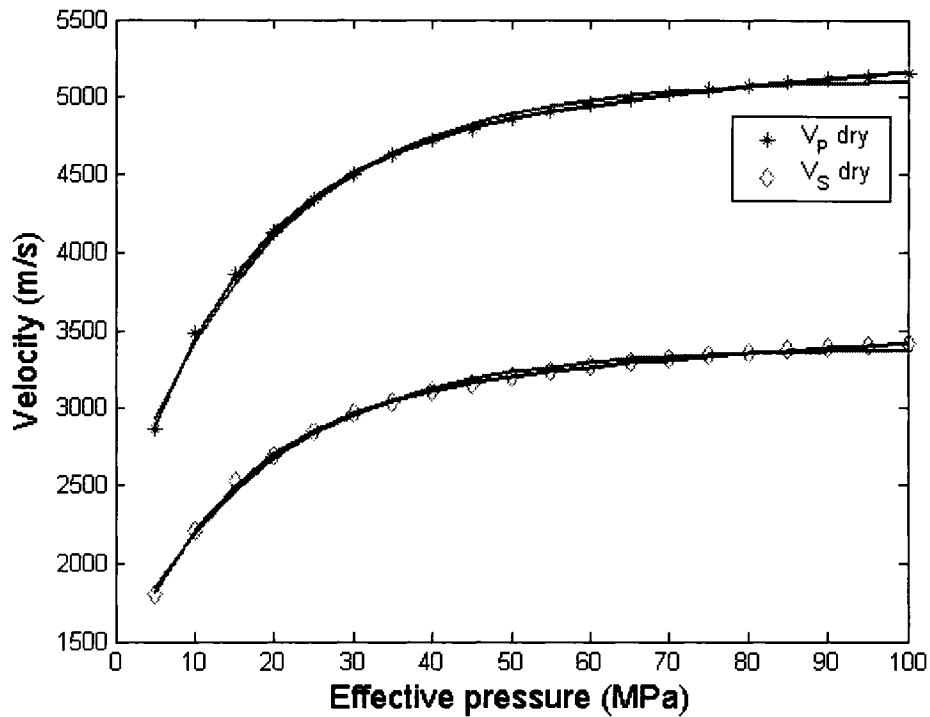


Figure 5.8: Experimental data and the best-fit curves for SB007. The star and diamond lines represent the experimental data for the dry V_p and V_s respectively. The red line and black line indicate the best-fit curves by least squares fitting method using equation 5.1 and 5.2 respectively.

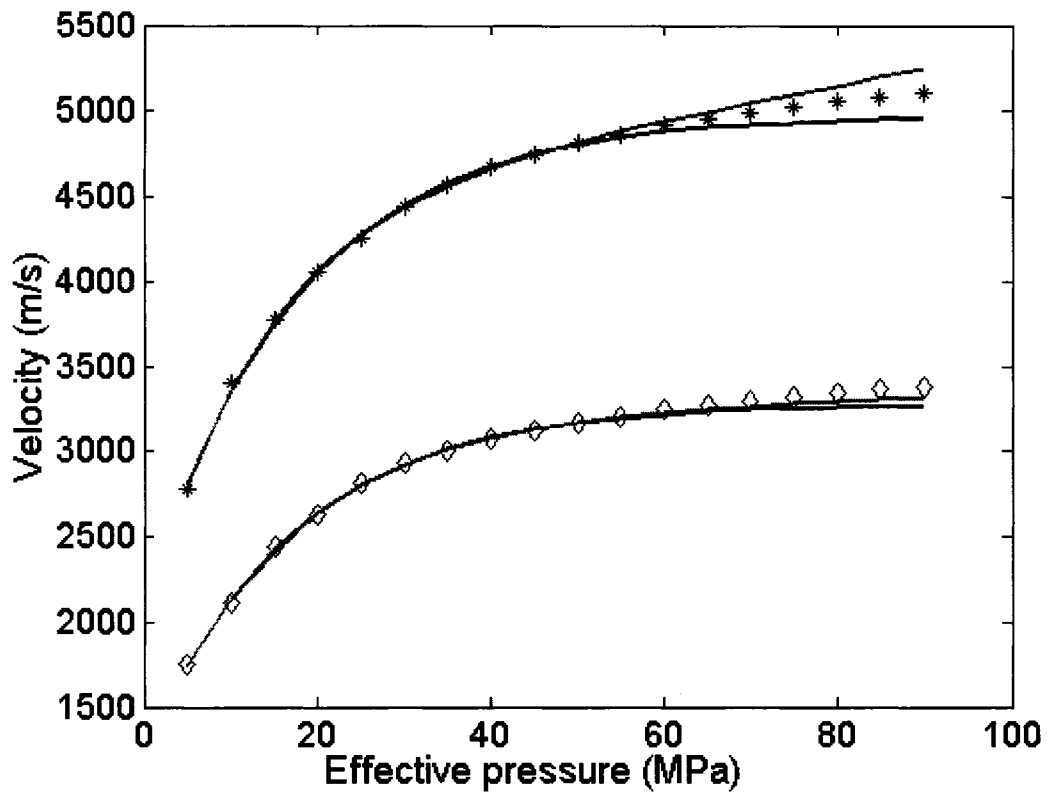


Figure 5.9: Test of the predictability of the empirical equations. The actual experimental data to 100 MPa is compared against the empirical curves determined from the observed velocities to 60 MPa for sample SB007. The star and diamond represent the experimental data for the dry V_p and V_s . The red line and black line indicate the best-fit curves by lsqr method using equation 5.1 and 5.2 respectively.

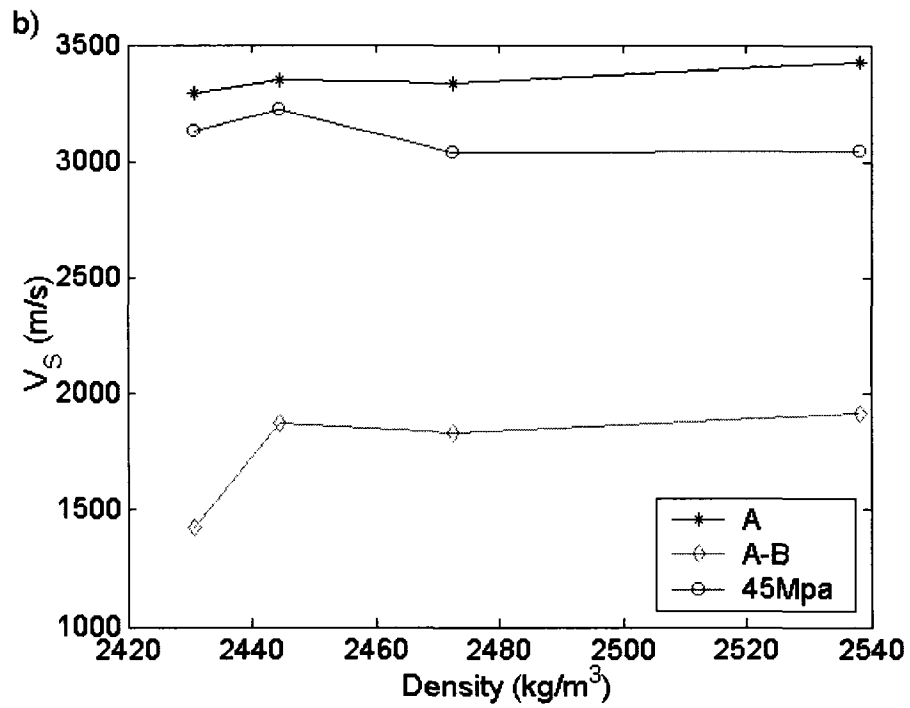
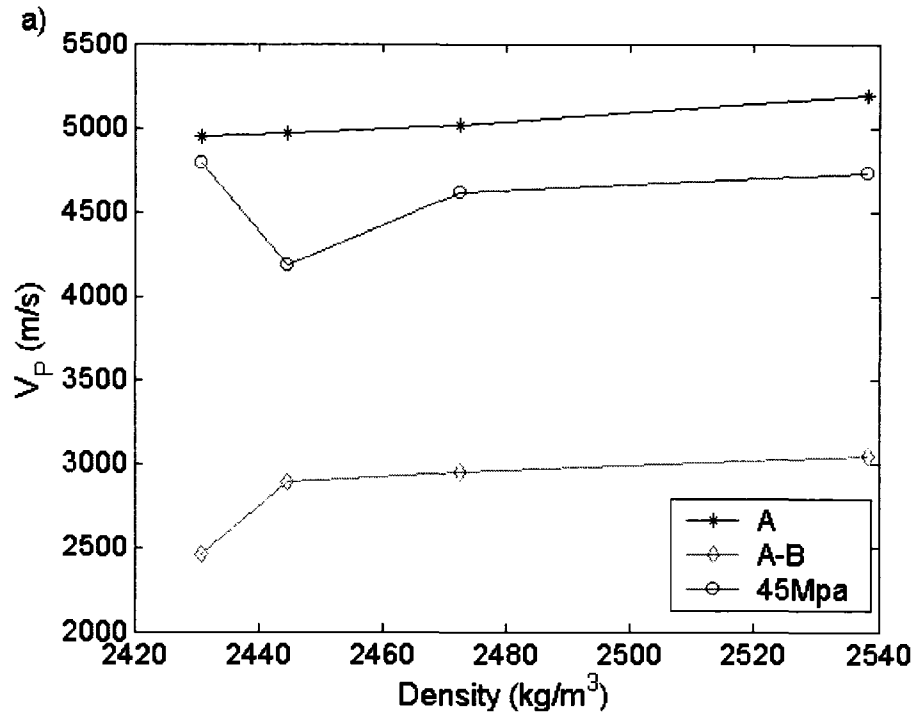


Figure 5.10: P-wave (Figure a) and S-wave (Figure b) velocity changes with density for the dry samples at zero effective pressure, pressure 45MPa and extremely high effective pressure.

Table 5.1: Best fit parameters using equation 5.2 for the experimental velocity data.

“Dry” represents the parameters for the dry sample; “Sat” means the parameters for the water saturated samples and “Par” is the partially water saturated samples (~7%).

		P-wave				S-wave			
		<i>A</i>	<i>B</i>	<i>D</i>	<i>A-B</i>	<i>A</i>	<i>B</i>	<i>D</i>	<i>A-B</i>
SB002	Dry	5238.2	1268.7	0.0853	3969.4	3663.3	670.0	0.0699	2993.4
SB003	Dry	5286.9	1578.2	0.0731	3708.7	3412.5	742.1	0.0428	2670.4
SB004	Dry	5496.6	1036.5	0.0450	4460.1	3468.2	640.2	0.0346	2828.0
	Sat	4942.0	580.5	0.0884	4361.5	3121.0	572.5	0.0639	2548.5
SB005	Dry	5211.6	730.6	0.0890	4481.0	3428.5	638.3	0.0744	2790.2
	Sat	5142.9	522.3	0.0586	4620.6	3308.0	655.9	0.0751	2652.1
SB006	Dry	4963.7	2071.9	0.0583	2891.9	3345.8	1471.3	0.0552	1874.6
	Sat	5103.0	839.5	0.0529	4263.5	3333.6	951.1	0.0603	2382.5
	Par	5271.7	2533.6	0.0552	2738.1	3467.3	1539.0	0.0539	1928.3
SB007	Dry	4948.8	2496.1	0.0611	2452.7	3293.4	1869.2	0.0543	1424.2
	Sat	5054.9	1093.2	0.0646	3961.7	3235.8	1387.9	0.0657	1847.9
	Par	5145.0	3014.4	0.0589	2130.6	3369.8	1987.0	0.0533	1382.8
SB008	Dry	5018.9	2070.3	0.0361	2948.6	3337.1	1505.6	0.0360	1831.4
	Sat	4995.1	1101.9	0.0609	3893.3	3162.5	942.0	0.0542	2220.5
	Par	5205.8	2377.3	0.0373	2828.6	3366.2	1453.7	0.0371	1912.4
SB009	Dry	5193.1	2147.1	0.0340	3046.0	3423.2	1505.8	0.0309	1917.4
	Sat	5164.1	1290.3	0.0569	3873.8	3197.4	1109.0	0.0529	2088.4

5.4 Water saturation and velocity dispersion

Fluid substitutions are an important concept in seismic attribute studies because they provide the interpreter with a valuable tool for modeling various scenarios that might explain an observed AVO anomaly at seismic frequencies or can assist in interpreting time-lapse seismic responses. Based on the bulk and shear modulus calculated from dry frame velocity measurement, the bulk moduli and shear moduli of the fully water

saturated rock were calculated using Gassmann's (1951) Eqn. 2.13. Gassman's equation also assumes that the shear moduli is not affected by the fluid saturation, therefore, the shear moduli of the fully saturated rock sample should be the same as the shear moduli of the dry frame.

As expected, the bulk moduli (Figure 5.11a) increase after the sample is fully saturated with water. What is interesting, however, is that we also observed an increase of the shear moduli (Figure 5.11b) at pressures below 60 MPa. A noticeable increase of both of the bulk and shear moduli from the values predicted by Gassmann's equation was also observed. However, the difference between the measured water-saturated bulk moduli and the predicted bulk moduli decreases with the increase of effective pressure, which means the local flow of the fluid in the microcracks have a big influence on the bulk moduli after water saturation by stiffening the rock. The other part of the deviation from the predicted value may be because of the frequency dispersion, the interaction of the water with the solid surface. The shear moduli increase after water saturation at pressures below 60 MPa, but the shear moduli of the water saturated rock become larger than the dry rock at pressures higher than 60 MPa.

It is generally accepted that velocity dispersion occurs when the acoustic wave propagates in fluid-saturated rocks. The existence of velocity dispersion between seismic (10-100 Hz) and ultrasonic frequencies (0.1-1 MHz) indicates that the results of laboratory velocity measurement cannot be directly applied to the interpretation of seismic data. Winkler (1986) and also Gist (1994) proposed a method to estimate the velocity dispersion between the zero frequency and ultrasonic frequencies. These methods requires the knowledge of the compressional and shear wave velocities

measured on the dry and fully fluid saturated rocks under ultrasonic frequencies. There are two assumptions underlying this method. The first one is the generally accepted phenomenon that the velocity dispersion of acoustic velocities in dry rocks is negligible; therefore the acoustic velocity can be assumed to be independent of frequency. The second assumption is that the zero frequency velocities in fully fluid saturated rocks can be predicted from the experimentally measured dry velocities using Gassmann's equation and can be approximated to the seismic frequencies.

As expected, Figure 5.12 shows that the P-wave velocity increases after water saturation, although the P-wave velocity at low pressures are much higher than that predicted by Gassmann's equation. In contrast to the theoretical prediction, which predicts that the S-wave velocity for the water saturated sample is always lower than that for the dry sample, this figure also shows an unexpected S-wave velocity increase after saturation at lower effective pressure. At higher effective pressures, the S-wave velocity-pressure curve of the dry rock cross over with that of the water saturated rock at 50 MPa, and the S-wave velocity for the dry rock is then less than that of the water saturated rock. This has been attributed to a number of mechanisms, such as viscous coupling, the reduction in free surface energy, and frequency dispersion due to local flow of the fluid in the microcracks (Khazanehdari and Sothcott, 2003). At higher pressures, the difference between the velocity of the dry and water saturated sample decreases with effective pressure; the S-wave velocity after water saturation begins to get larger than the dry sample, which has a trend to approach the theoretical velocity values predicted by Gassmann's equation. These velocity changes further demonstrate that the microcracks

and micro porosity not only plays an important role in controlling the pressure dependent velocity but also has a large effect on the velocity.

Based on the experimental dry velocities and density changes after water saturation, the theoretical P-wave and S-wave velocities were calculated. Figure 5.12 shows the dry, water saturated experimental and theoretical P- and S-wave velocities as a function of effective pressures. From the figure, we can see that both of the experimental P- and S-wave velocities are larger than the theoretical values. The theoretical S-wave velocity slightly decreases about 1.3% after the dry rock is saturated with water because the density increases and the shear modulus is unchanged. The theoretical P-wave, however, increased from 20% at low pressure to 2% at a pressure of 60 MPa. The velocity dispersion of the P- and S-wave is pressure dependent (Figure 5.13). The frequency dispersion of P-wave decreases with increasing effective pressures from 15% at very low effective pressure (5MPa) to less than 1% at higher effective pressure above 60 MPa. However the frequency dispersion of S-wave decreases with increasing effective pressures from 21% at very low effective pressure (5MPa) to 1% at higher effective pressure above 55 MPa. This means the S-wave dispersion is larger than the P-wave dispersion for this sample at lower effective pressures. At effective pressure higher than 30 MPa, both of the P- and S-wave velocity dispersions are less than 4%. The pressure dependency of the P- and S-wave dispersion further demonstrate that the microcracks in which the local fluid flow is induced by acoustic wave play an important role in controlling the acoustic velocities.

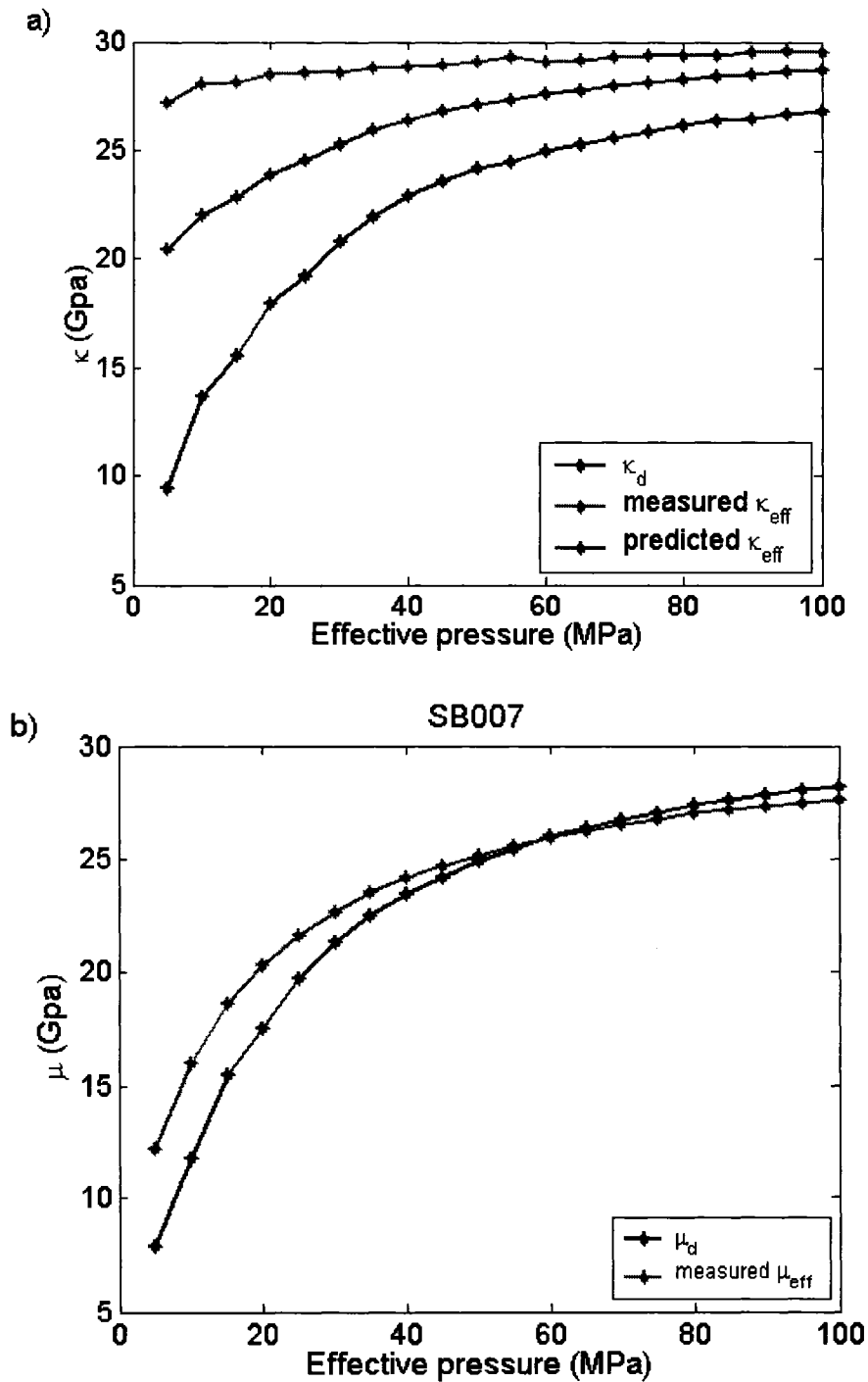


Figure 5.11: Changes in the dry and water saturated (both experimentally determined and Gassmann's equation predicted) bulk (Figure a) and shear moduli (Figure b) with effective pressure. The Gassman's equation predicted shear moduli is equal to the dry shear moduli.

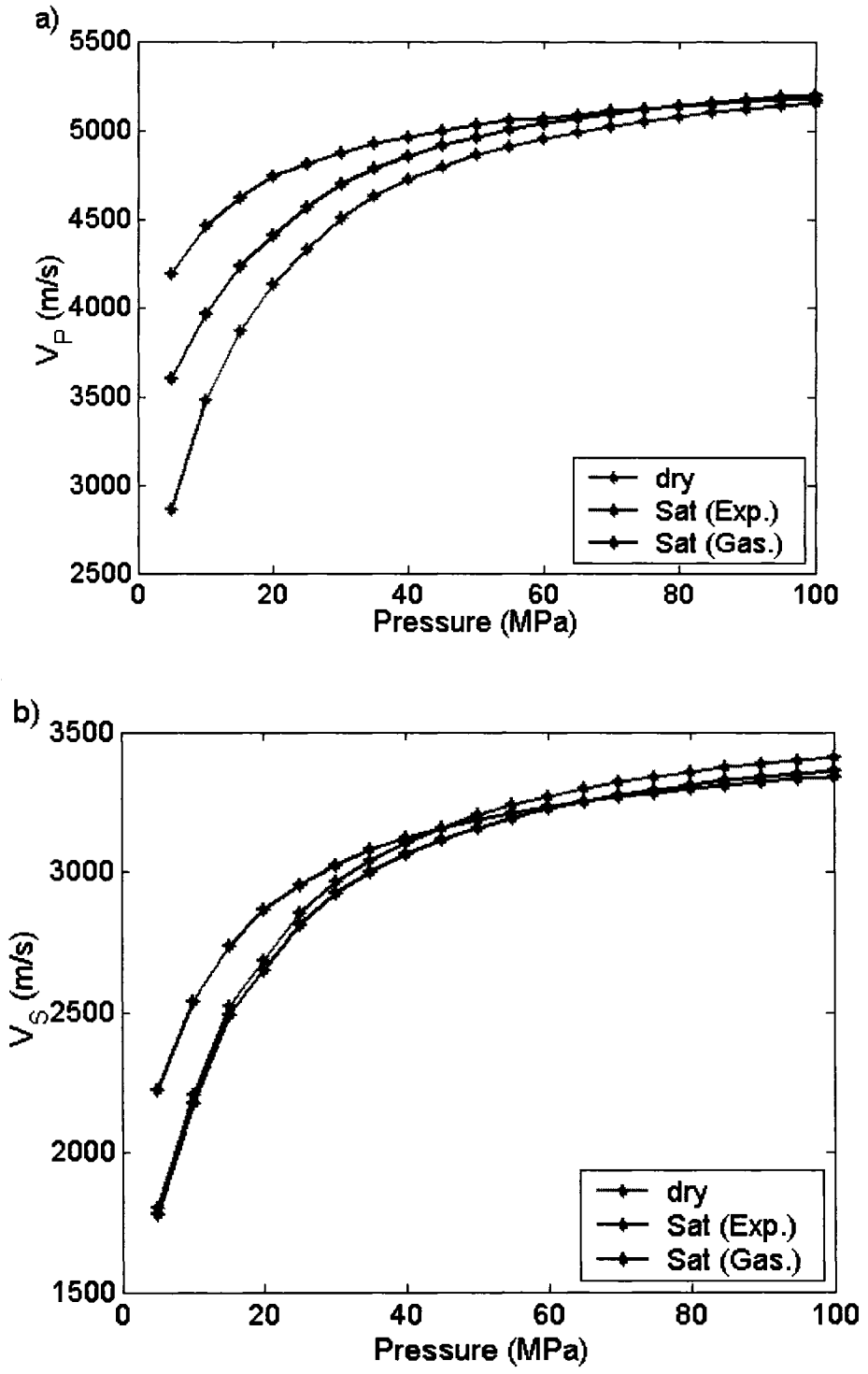


Figure 5.12: P-wave (Figure a) and S-wave (Figure b) velocity changes as a function of effective pressure for the dry, experimental and Gassmann's equation predicted values of water-saturated sample (SB007) with a higher peak pressure 100MPa.

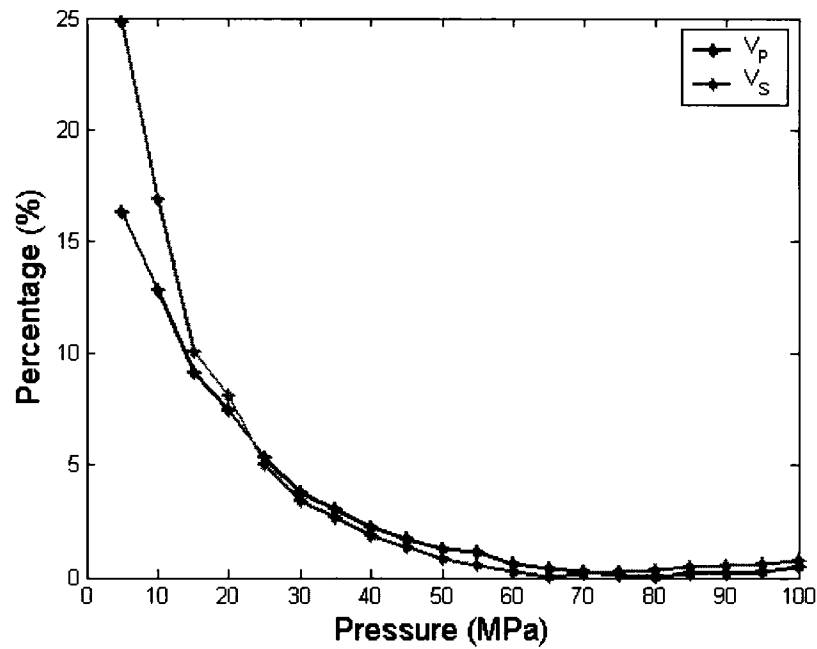


Figure 5.13: Velocity dispersion between theoretical Gassmann and the observed laboratory measured P- and S-wave velocities as a function of effective pressure for a fully saturated sample SB007.

5.5 V_p/V_s ratios and Poisson's ratio

The P- and S-wave velocity ratio (V_p/V_s) is very sensitive to the fluid type in the reservoir, differential pressure, pore geometry, porosity and many other factors. The crossplot by Pickett (1963) from the laboratory measurements popularized the use of (V_p/V_s) as a lithology indicator. The V_p/V_s ratio has also been used for many other purposes, such as pore fluid identification, consolidation degree determination and predicting S-wave velocities. In this thesis, we mainly study how the water saturation, pore geometry and pressure will affect this velocity ratio.

The velocity ratio is very sensitive to the type of fluid in the reservoir rocks and can provide information on the fluid type and saturation state of the reservoir rocks. The P-

wave velocity of a rock saturated with less compressible fluid shows a higher increase than the more compressible fluid, but the S-wave velocity is not as much affected by the fluid saturation because only the density changes account for the S-wave velocity changes. Therefore, rocks saturated with less compressible fluid have a large value of V_p/V_s ratio. The dependence of V_p/V_s ratio on pore fluid can be used for direct hydrocarbon detection and fluid identification. The theoretical models and experimental work show the importance of cracks and pore geometry in determining the value of V_p/V_s ratio, but show little variation with mineral composition of the rocks (Tatham, 1982). Because the cracks and porosity of the rocks will change during the loading and unloading stress, the V_p/V_s ratio of most rocks are pressure dependent. The laboratory data shows that V_p/V_s ratio of most samples generally increases with pressure with a small proportion of the samples do show the opposite trend (MacBeth, 2004). However, we observed a decreasing V_p/V_s ratio with confining pressure for all these consolidated samples with many cracks developed intra- and inter grains (Figure 5.14). The V_p/V_s ratio ranges from 1.35-1.60 for the dry samples. The V_p/V_s ratio increases after the dry sample is saturated with water and the differences between the dry and water-saturated V_p/V_s ratio become smaller when the differential pressure increases.

The experimental observation of Poisson's ratio can be used to calibrate the interpretation of seismic amplitude anomalies and amplitude versus offset (AVO) analysis. Spencer et al. (1994) observed a wide range of values from 0.091 to 0.237 in unconsolidated sands and sandstones, although 92% of the samples are within 0.12 and 0.23. From Figure 5.15, we can see that the Poisson's ratio for both of the dry (0.18-0.11)

and water saturated (0.30-0.14) samples decrease with effective pressure. The Poisson's ratio of the water-saturated sample is much higher than the dry sample.

Mudrock line is the line on a crossplot of P-wave velocity against S-wave velocity along which water saturated sandstone, shale and siltstones fall approximately. Gas-saturated sandstones have lower P-wave velocity and slightly higher S-wave velocities, and therefore falls off this trend line. Some of the other rock types that lie off the 'mudrock line' are carbonates and igneous rocks. The empirically derived "mudrock line" relationship between P- and S-wave velocity for water saturated elastic rocks is determined by Castagna et al. (1985):

$$V_p = 1360 \text{ m/s} + 1.16V_s \quad (5.3)$$

where both V_p and V_s are given in m/s. Crossplot of P-wave against S-wave velocities for four dry and water-saturated samples at different effective pressure the "mudrock line" are plotted (Figure 5.16). It shows that the velocities for the water-saturated samples almost fall along the "mudrock line", however, the dry sample lies below the "mudrock line" that means a relative low V_p/V_s ratio.

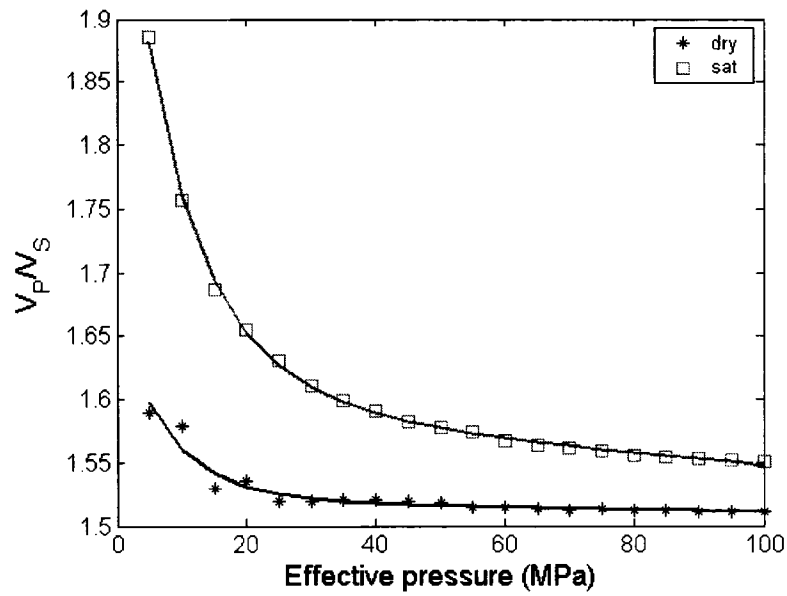


Figure 5.14: P- and S-wave velocity ratio as a function of effective pressure for sample SB007. The star, square represent the experimental data for the dry and the water saturated respectively. The solid line indicates the best-fit curves using lsqr method.

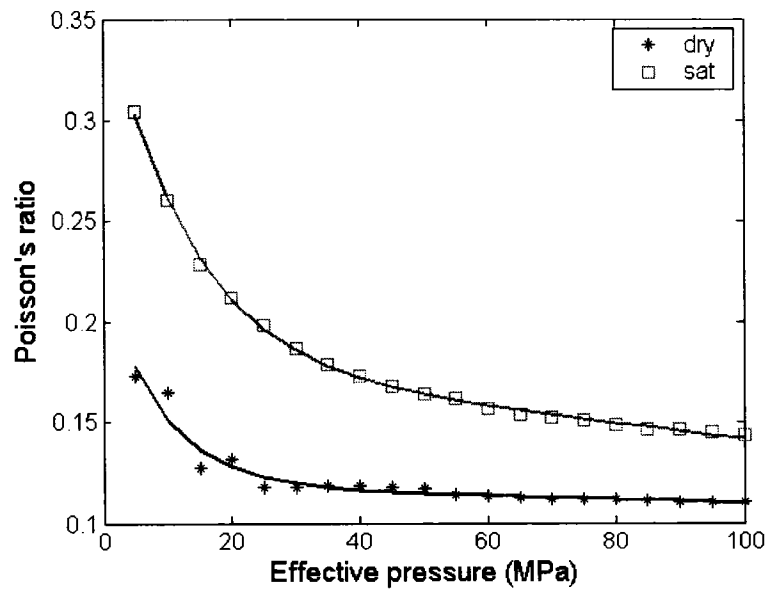


Figure 5.15: Poisson's ratio as a function of effective pressure for sample SB007. The star, square represent the experimental data for the dry and the water saturated respectively. The solid line indicates the best-fit curves using lsqr method.

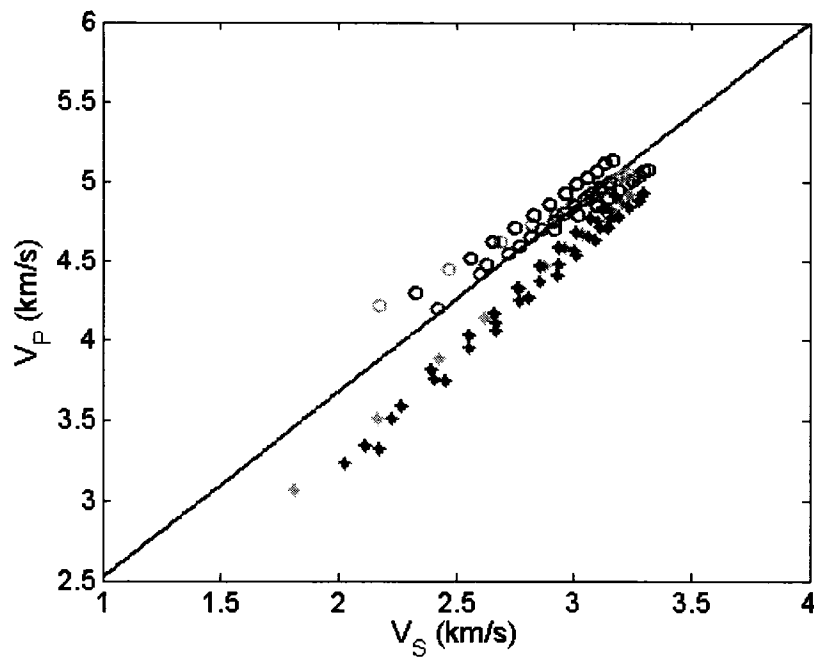


Figure 5.16: Crossplot of P-wave against S-wave velocities for four dry and water-saturated samples. The colors represent different samples, and circles and stars represent the velocities of the dry and water-saturated samples at different effective pressures respectively. Higher velocity corresponds to higher effective pressure. The blue line is the ‘mudrock line’ defined by Castagna et al. (1985).

5.6 Effective stress coefficient

The pore pressure (formation pressure or reservoir pressure) is generated by fluid trapped within the pores of the reservoir rock. When the formation is enclosed by impermeable rock such as shale, the pore fluid of the pores cannot always escape and then support the total overlying rock column, leading to a high pore pressure. Just as the confining pressure, the pore pressure also acts equally in all direction; however, it has an opposite effect to the confining pressure on the seismic velocities and rock properties. An increase of the pore pressure will open the microcracks in the rock by supporting the stress caused

by the confining pressure. Therefore, the pore pressure generally decreases the wave velocities and rock stiffness. The combining effect of internal pore pressure and confining pressure on the elastic wave velocities leads to an effective pressure that is expressed as $P_e = P_c - nP_p$, where n is the effective stress coefficient and found to be close to 1. This equation means the internal pore pressure has an opposite effect on the wave velocities to the confining pressure. When the internal pore pressure (P_p) exactly cancels the effect of the confining pressure (P_c), this equation can be reduced to $P_e = P_c - P_p$ with the effective stress coefficient being 1. The difference between confining pressure and internal pore pressure is defined as the differential pressure that is represented by P_d . The experimental value of n can be estimated using the following equation (Todd and Simmons, 1972; Christensen and Wang 1985; Prasad and Manghnani 1997):

$$n = 1 - \frac{\left(\frac{\partial V}{\partial P_p} \right)_{P_d}}{\left(\frac{\partial V}{\partial P_d} \right)_{P_p}} \quad (5.4)$$

where V is the P-wave or S-wave velocity. The numerator of the second term in the right side of equation is the slope of the linear line at constant differential pressure; the denominator is the slope of the observed nonlinear velocity versus confining pressure curve at constant pore pressure (i.e. $P_p = 0$ for this case) (Figure 5.17-5.22).

Table 5.2 lists a series of values of n at different differential pressure for both of P- and S-wave velocities at differential pressure 15 MPa and 30 MPa for all the samples. From these tables, we can see that the effective stress coefficient n is lower at higher

differential pressure than that at lower differential pressures; n for the P-wave velocities is typically greater than the n for the S-wave.

Table 5.2: Effective stress coefficient n for P- and S-wave velocities at constant differential pressures of 15 MPa and 30 MPa.

	P-wave		S-wave	
	15MPa	30MPa	15MPa	30MPa
SB004	0.93	0.59	0.98	0.60
SB005	0.83	0.87	0.95	0.95
SB006	0.97	0.93	0.99	0.98
SB007	0.95	0.95	0.99	0.99
SB008	0.92	0.78	0.99	0.88
SB009	0.95	0.88	0.98	0.92

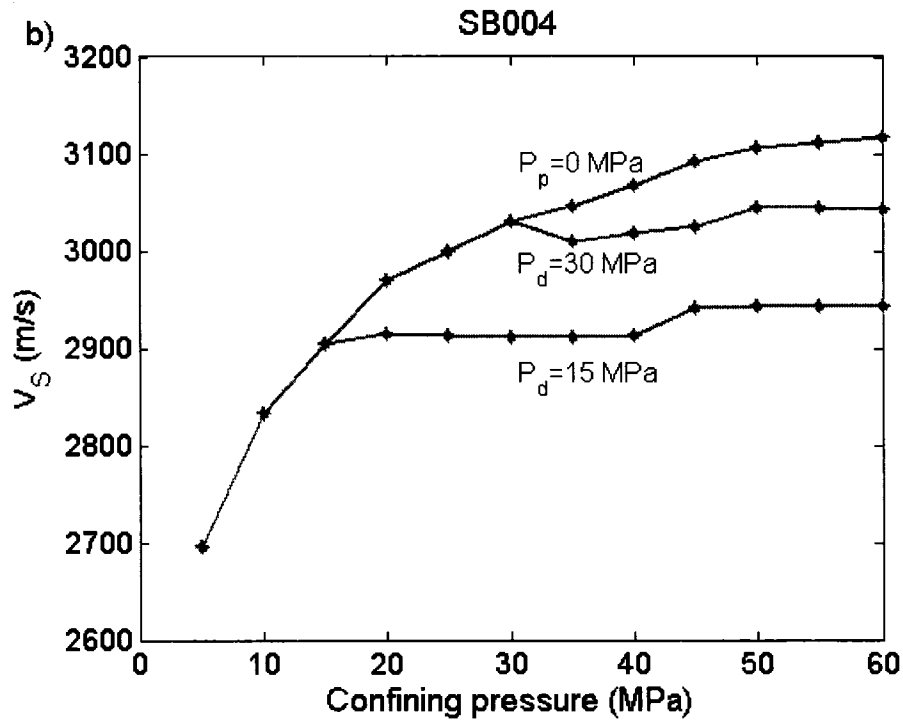
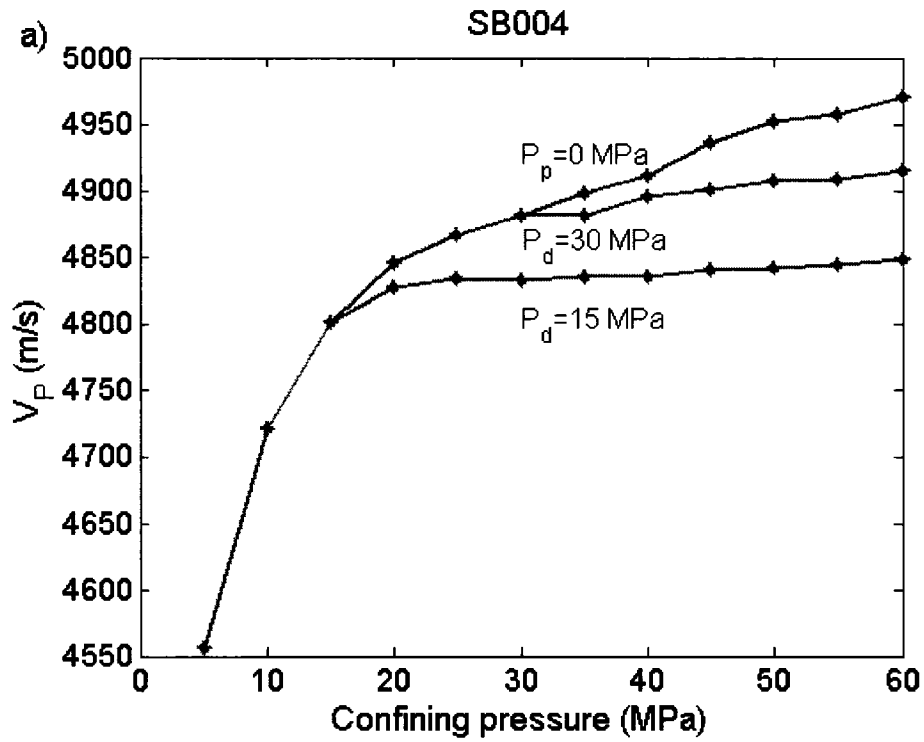


Figure 5.17: P-wave velocity (Figure a) and S-wave (Figure b) as a function of confining pressure and differential pressure for water saturated, but spoiled, sample SB004.

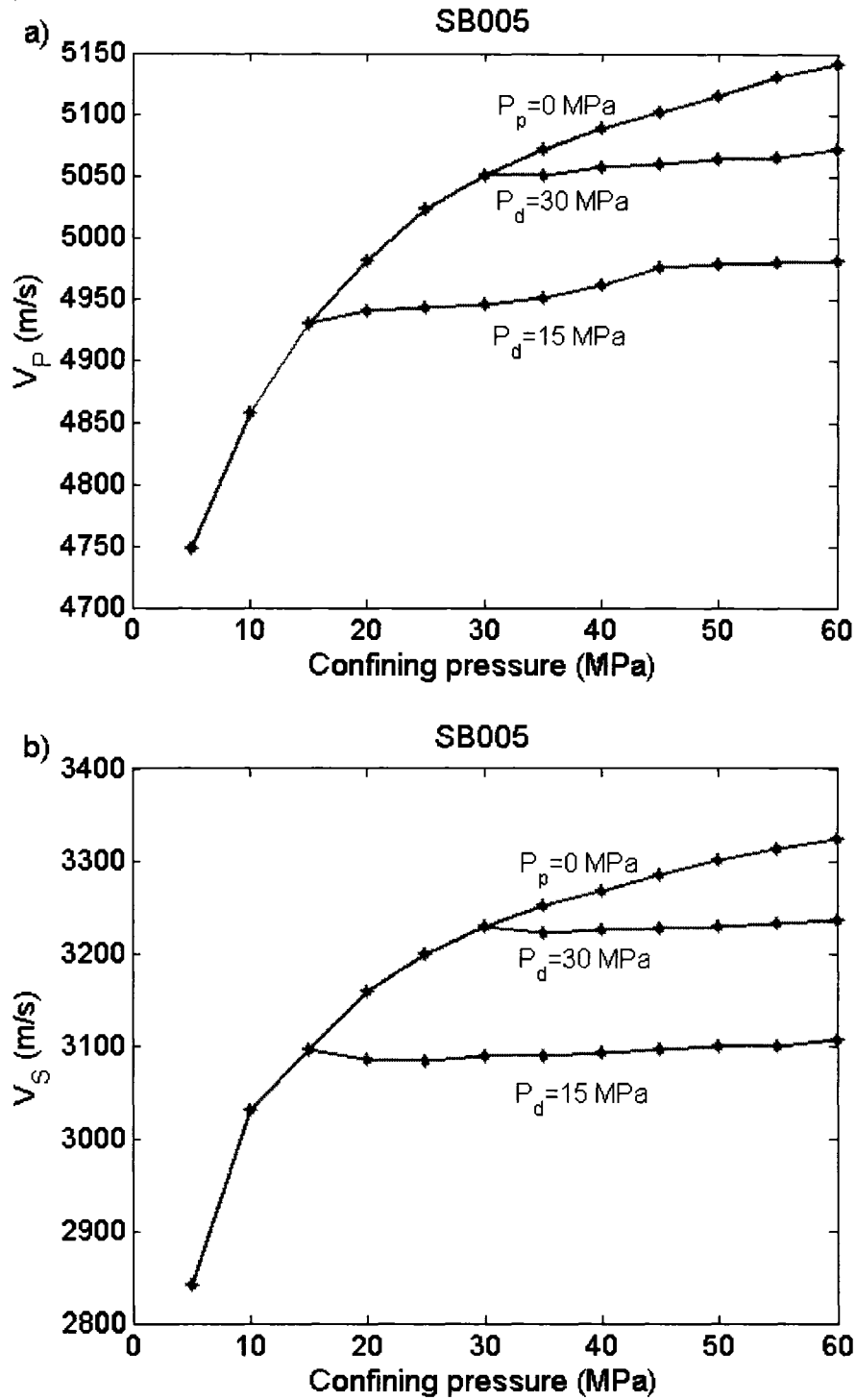


Figure 5.18: P-wave velocity (Figure a) and S-wave (Figure b) as a function of confining pressure and differential pressure for water saturated sample, but spoiled, SB005.

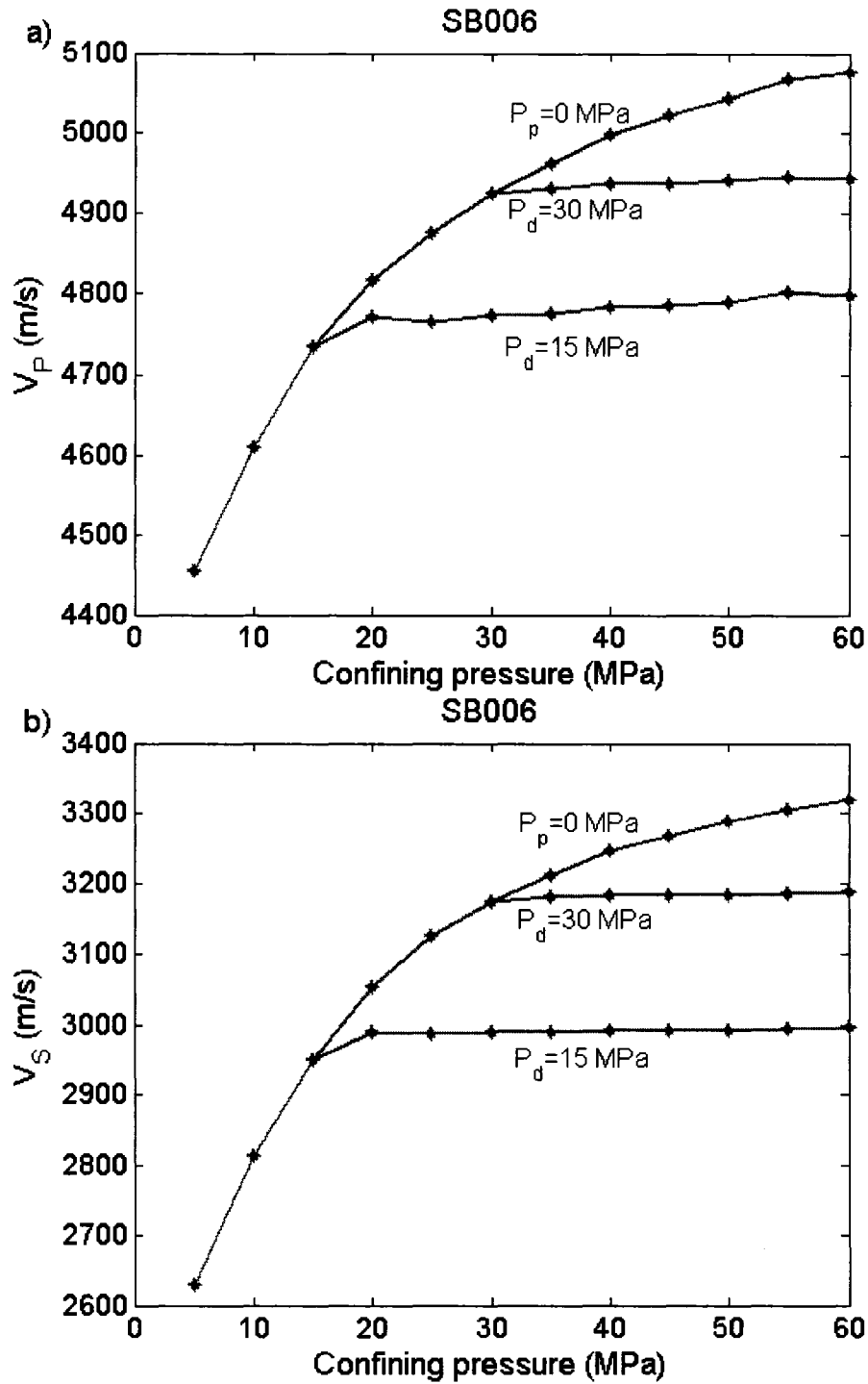


Figure 5.19: P-wave velocity (Figure a) and S-wave (Figure b) as a function of confining pressure and differential pressure for water saturated sample SB006.

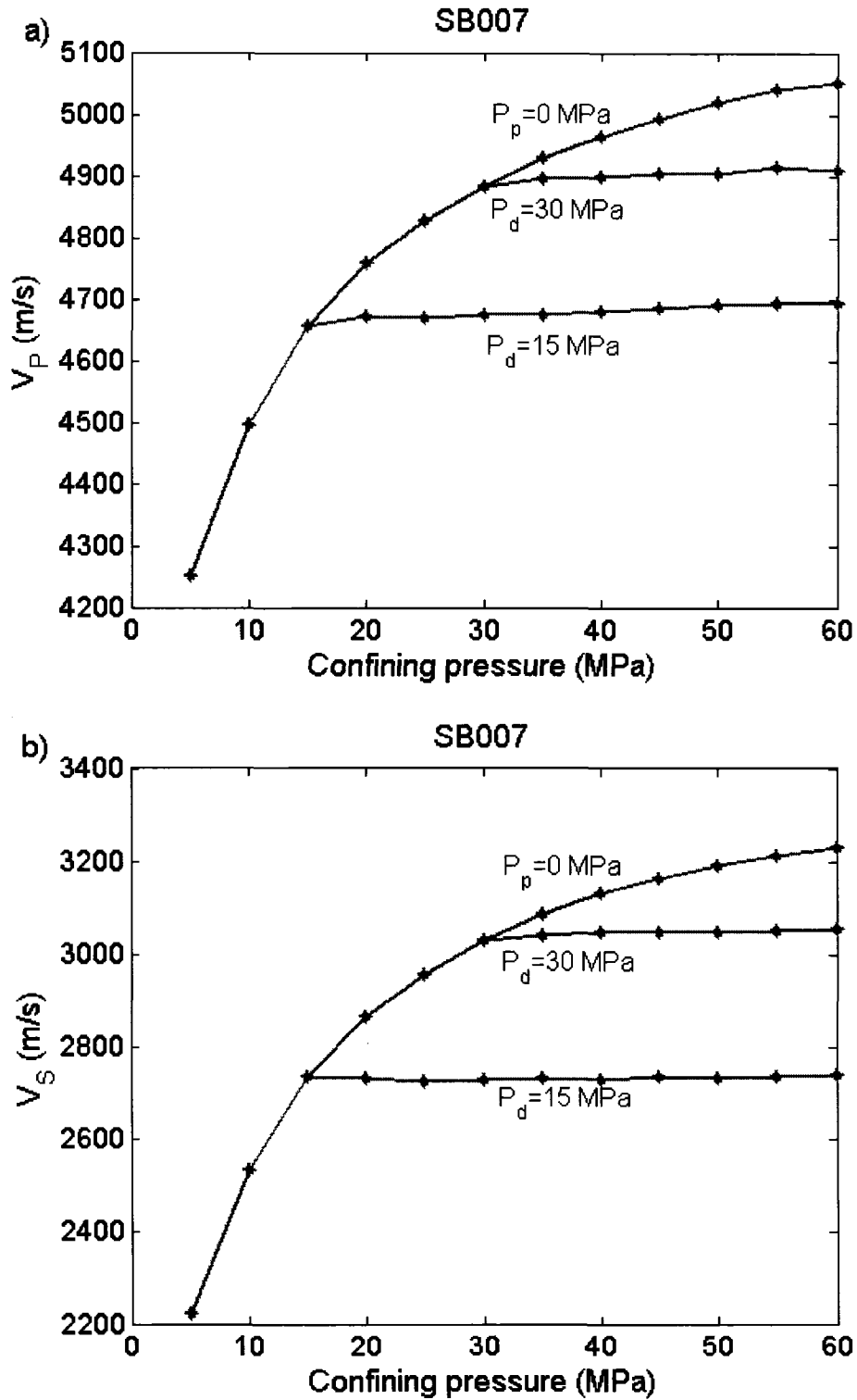


Figure 5.20: P-wave velocity (Figure a) and S-wave (Figure b) as a function of confining pressure and differential pressure for water saturated sample SB007.

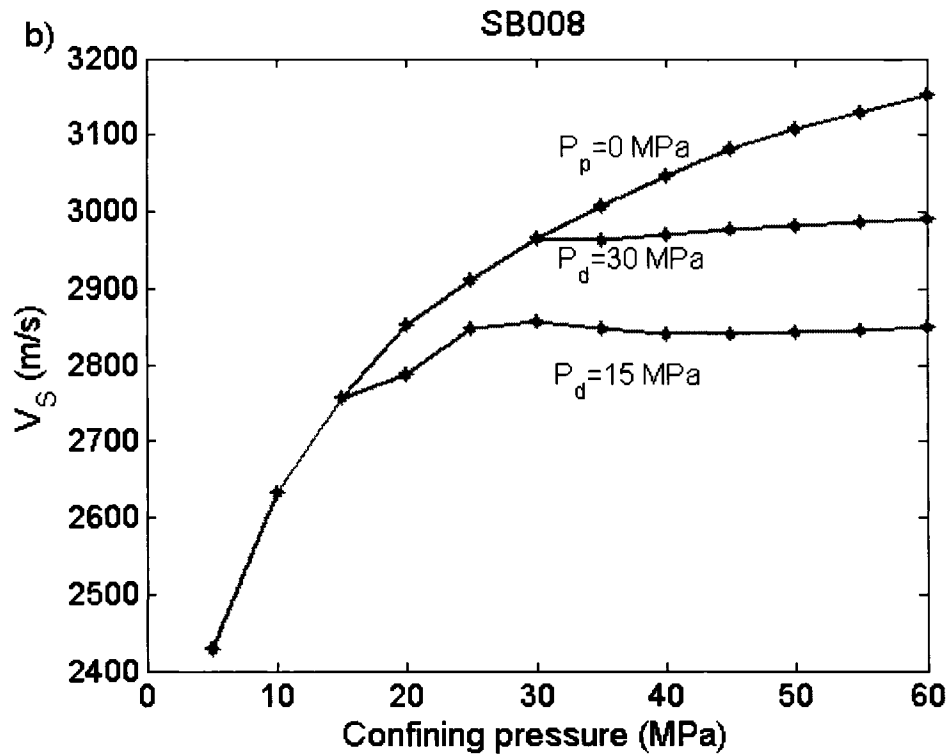
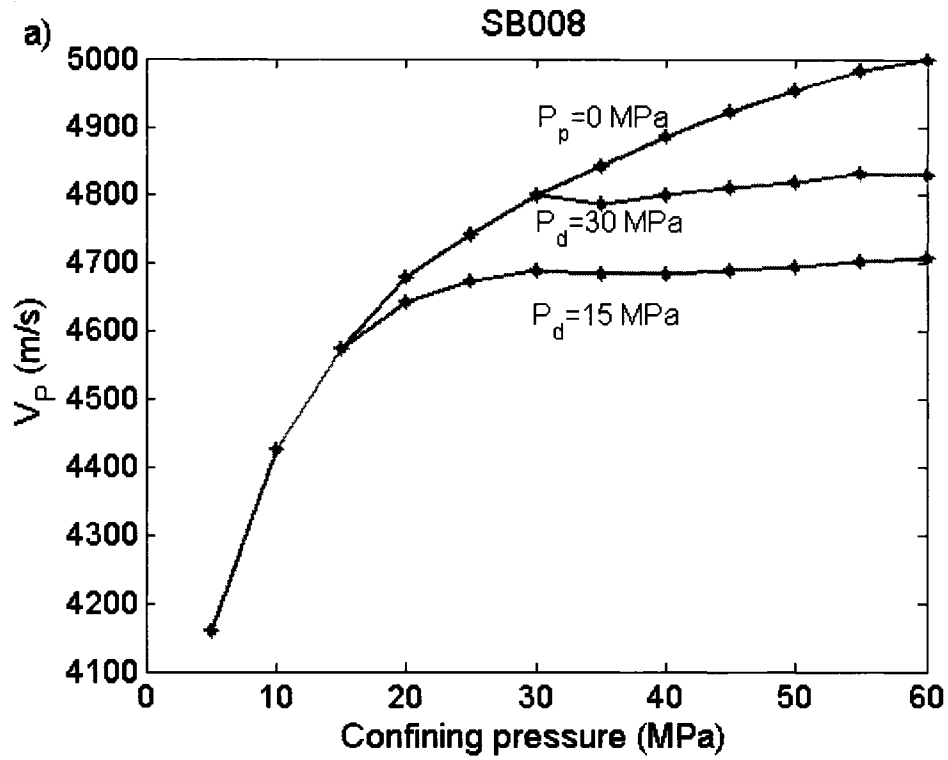


Figure 5.21: P-wave velocity (Figure a) and S-wave (Figure b) as a function of confining pressure and differential pressure for water saturated sample SB008.

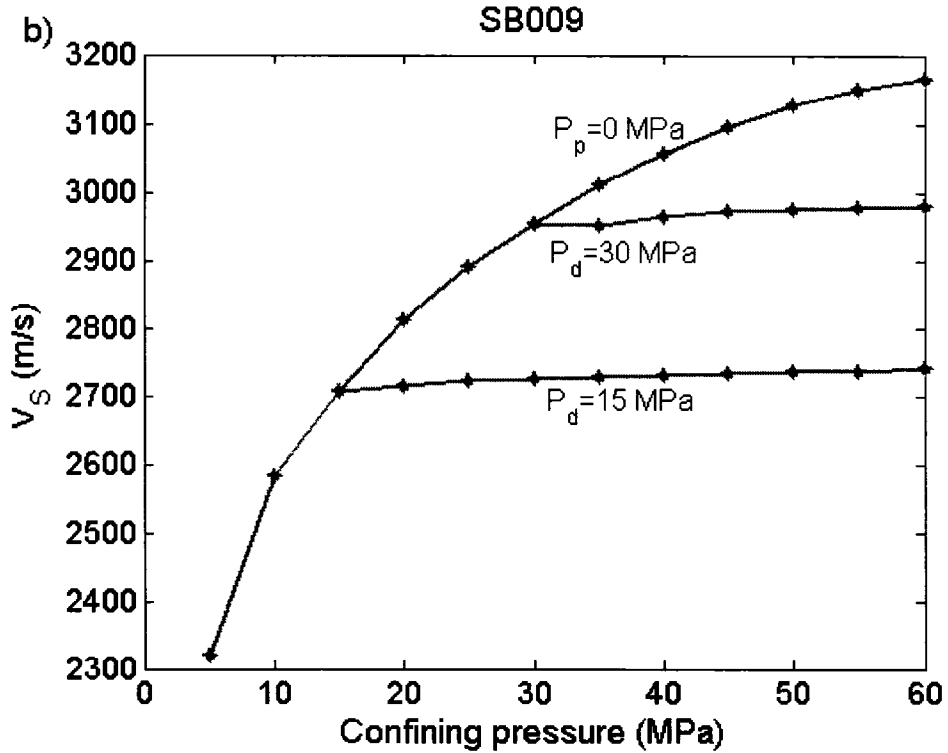
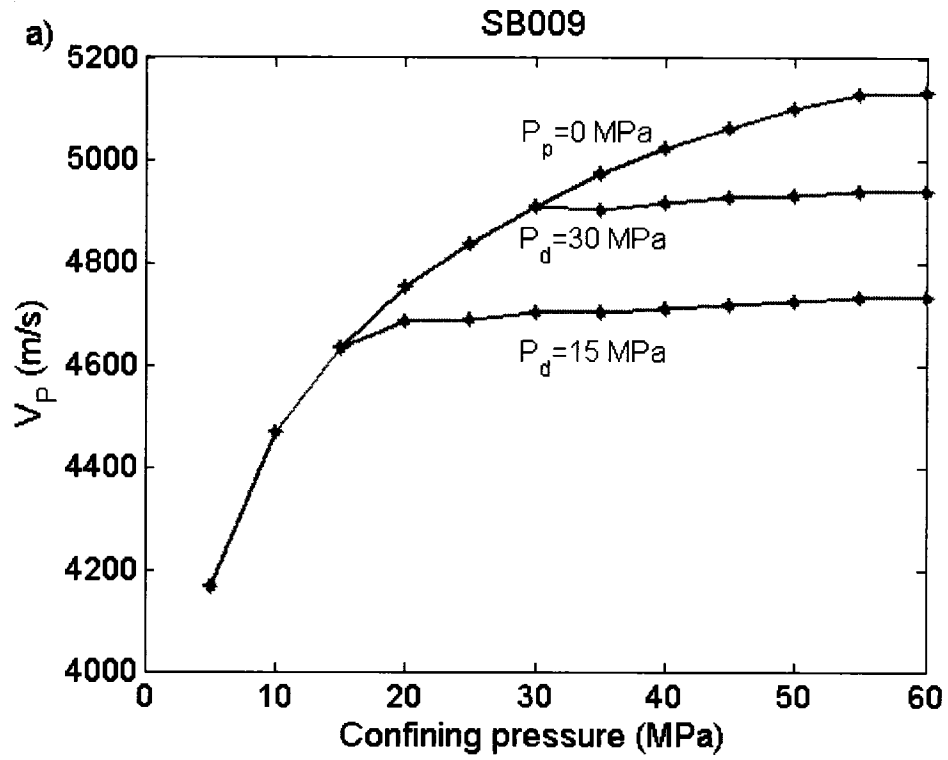


Figure 5.22: P-wave velocity (Figure a) and S-wave (Figure b) as a function of confining pressure and differential pressure for water saturated sample SB009.

The four latter samples, that were not spoiled by oil penetration, mostly show similar behaviour with both the P and S wave velocities remaining nearly constant and with values of n slightly less than, but very close to, unity. The plots for sample SB008 are anomalous in that they do not, at least at low confining pressure, appear to satisfy a simple linear relationship. The reasons for this are not completely known but may be related to the small pore dimensions in this rock. For example, it may have been that the pore fluid mass or pressure did not have time to properly equilibrate.

5.7 Discussions and conclusions

In order to better understand its seismic response, compressional and shear wave velocities were measured on a series of low porosity conglomerates under different confining and pore pressures under both dry and water saturated conditions. P- and S-wave velocities were simultaneously measured using standard pulse transmission methods. P-wave velocity, S-wave velocity, frame bulk and shear moduli are all highly pressure-dependent. They normally increase sharply at low differential pressure and then tend to stabilize at higher pressures. These indurated rocks show little consolidation during pressurization. According to Gassmann's equation, the P-wave velocity will increase and the S-wave velocity slightly decreases due to the density changes after fluid saturation. However, we see a noticeable increase of the S-wave after water saturation at low effective pressure. Both of the experimentally measure P- and S-wave at ultrasonic frequencies are much higher than the Gassmann's equation calculated velocities which assume zero frequency. The deviation of the experimental velocities from the theoretical values can be attributed to the frequency dispersion; the microcracks that cause local

fluid flow. The V_p/V_s ratio increases after the dry sample is saturated water and the ratio for both of the dry and water-saturated samples shows decreases with increasing differential pressure. The differences become smaller when the differential pressure increases.

From the experiments, we find the pore pressure has an opposite effect to the confining pressure on the P- and S-wave velocities. The pore pressure increases almost but cannot completely cancel the equal amount of confining pressure increases. The calculation of the elastic coefficient n relating to the pore and confining pressure showed that this value is lower at higher differential pressure than that at lower differential pressures; n for the P-wave velocities is less than the n for the S-wave.

Chapter 6

Pressure and fluid sensitivity of AVA response

This chapter presents the results of modeling of the variations in seismic reflection strength with the angle of incidence. The background and theory of this Amplitude versus Angle (AVA) method, usually employed to assist in discriminating between gas and liquid saturated reservoir rock, is described. AVA curves are then calculated using the results of the laboratory measurements and the implications for detecting gas versus water filled reservoir is discussed.

6.1 Background of amplitude versus angle analysis

Little, or no, petroleum exploration is carried out today without the additional information provided by seismic imaging, the economic risks involved are far too large without use of this tool to examine the geological structure of a target. However, additional information can be obtained from the seismic data that can assist in further reducing risk by providing some indications of what the fluid content might be. The simplest of such techniques is to search the final 'post-stack' seismic images for 'bright spots' which are zones of high reflectivity that ultimately result from the variations in the seismic impedance between those portions of a geological formation saturated with liquid (water or oil) versus those saturated with free gas. In this simplest case, the seismic

velocity of the gas saturated rock is substantially lower than that for the same, liquid saturated material. Consequently, the ‘normal-incidence’ reflection co-efficient R_{pp} :

$$R_{pp} = -\frac{\rho_1 V_{p1} - \rho_2 V_{p2}}{\rho_1 V_{p1} + \rho_2 V_{p2}} \quad (6.1)$$

where ρ_1 , V_{p1} and ρ_2 , V_{p2} are the density and P-wave velocity of upper and lower media, will depend on the saturation state of the rock. In the Western Canada Sedimentary Basin, many explorationists search for shallow (< 1000 m deep) gas deposits using such simple methods by looking for ‘bright spots’.

It is useful to make a few observations about the behaviour of the normal incidence reflection co-efficient $R_{pp}(\theta = 0)$. First, the magnitude of the reflection essentially depends on the contrast in the elastic impedance $\rho_2 V_{p2} - \rho_1 V_{p1}$ across the geological interface. Second, the sign, or more accurately the polarity, of the reflection depends on whether the impedance of layer 1 is greater or less than that of layer 2. It is useful to consider some extreme cases here. In the first case, let layer 1 be air and layer 2 be a stiff solid such as steel. In this case, $R_{pp}(\theta = 0)$ is very close to +1 as $\rho_2 V_{p2} \gg \rho_1 V_{p1}$. In the second case, let layer 1 be steel and layer 2 be air for which $R_{pp}(\theta = 0)$ is nearly -1. What this means is that the polarity of the reflected wave also depends on the relative contrasts; this polarity contains information on which of layer 1 or 2 has lower impedance. AVA analysis can provide even more information by studying how both the amplitude and the polarity will change with angle of incidence.

Reflection and transmission will occur when seismic waves propagate in a discontinuous media. The reflection and transmission of an incident P-wave occurring on a simple isotropic two-layer model is shown in Figure 6.1. If the incident angle is not

zero, the P-wave energy is partitioned into reflected P- and S-wave and transmitted P- and S-wave components. The reflected and transmitted P- and S-wave velocities depend on the contrast in the physical properties such as the density, P- and S-wave velocities across the boundary. Further information may be obtained, however, by studying the behaviour of the seismic reflections from a given geological interface, particularly how their amplitude and phase will change with the angle of incidence of the seismic energy to the reflecting geological interface. The reader may be more familiar with the dependence of the intensity of light being reflected from, say, the surface of a body of water on the angle of the light's incidence. The sun's reflection from a still lake is weak when the sun is overhead, but later in the day the reflected light is nearly as strong as the sun itself. Seismic waves experience similar effects when reflected from a geological interface. Essentially, the energy of a given incoming wave is partitioned between reflected and transmitted portions depending on the contrasts in the materials elastic properties and densities as will be described below. The problem is more difficult than that for a reflected light wave as one must also consider the conversion of waves at the interfaces between P and S modes also. This problem has long been studied in geophysics, and indeed the solution to the fully elastic problem was provided by Karl Zoeppritz (1919), one of the pioneers of seismology, which was published 11 years after his early death at the age of 26 in 1908.

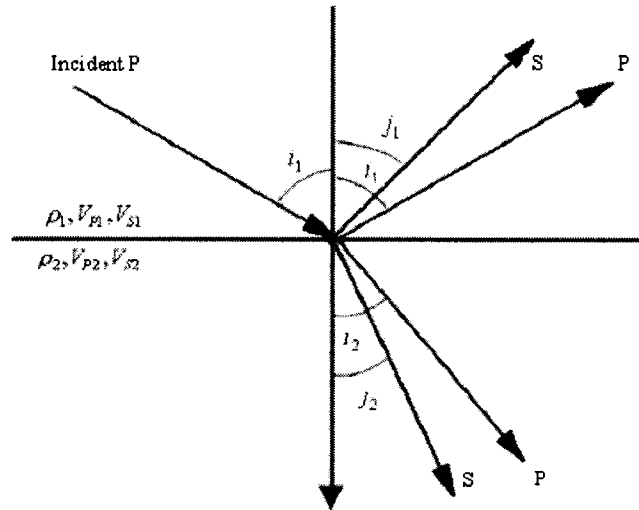


Figure 6.1: Sketch map showing the reflected P- and S-wave in upper layer and the transmitted P- and S-wave in lower layer of an incident P-wave in upper layer on a solid-solid interface. i_1, i_2 represent the reflected and transmitted angles for P-wave; j_1, j_2 represent reflected and transmitted angles of S-wave respectively; ρ_1, V_{P1}, V_{S1} are the density, P- and S-wave velocities in the upper medium; ρ_2, V_{P2}, V_{S2} are the density, P- and S-wave velocities in the lower medium.

The problem was reconsidered by Ostrander (1984) who carried out simple modeling to demonstrate how one might expect the seismic amplitude to vary as with the angle of incidence for a compliant sand layer encased by higher impedance shale (Figure 6.2). The P-wave velocity of the shale is 3048 m/s, an increase of 610 m/s from the velocity of the gas sand. The density of the shale is 2.40 g/cm^3 , which is 10% higher than the density of the gas sand. The poisson's ratio of the shale and gas sand is 0.1 and 0.4 respectively. The result of this model gives a reflection coefficient of 0.16 on the top and bottom of gas sand with different polarity (Figure 6.3). The solid lines in Figure 6.3 shows that the

reflection coefficient on the top and bottom of gas sand change substantially up to 70% from normal incidence angle to 40 degrees.

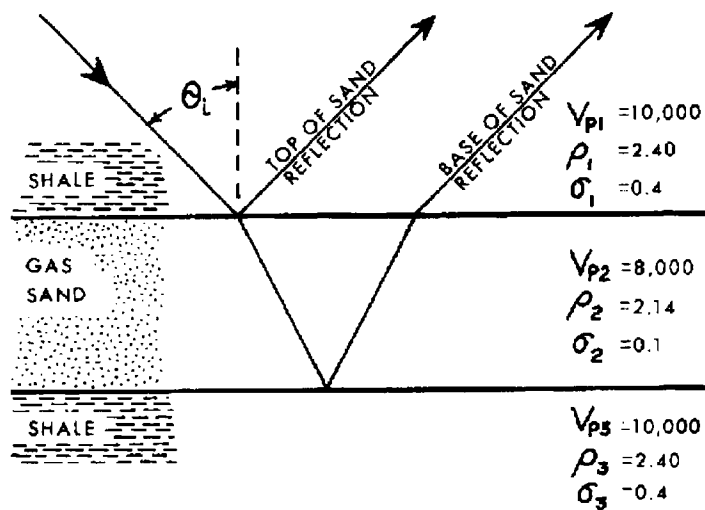


Figure 6.2: A gas model showing the gas sand encased in shale, figure from Ostrander (1984) with the permission to use granted by the Society of Exploration Geophysics.

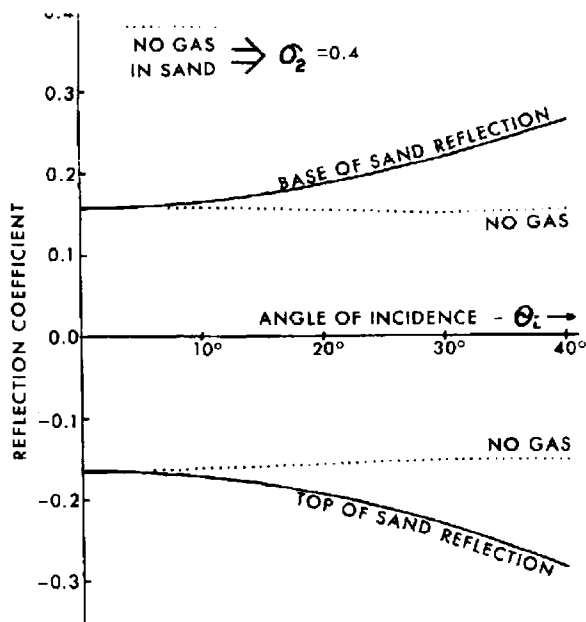


Figure 6.3: P-wave reflection coefficient changes with angle of incidence for the above gas model, figure From Ostrander (1984) with the permission to use granted by the Society of Exploration Geophysics.

Rutherford (1989) built on this work and provided further classifications of the types of amplitude versus angle of incidence behaviour one might be expected to encounter in practice. He classified the gas sands into three classes: class I, class II and class III depending on the impedance contrast of the gas sands and the overlying shale. The class I, II and III gas sands have higher, nearly the same and lower impedance relative to the overlying shale. Castagna et al. (1998) found the existence of class IV gas sands for which the magnitude of reflection efficient decreases with the angle of incidence (Figure 6.4).

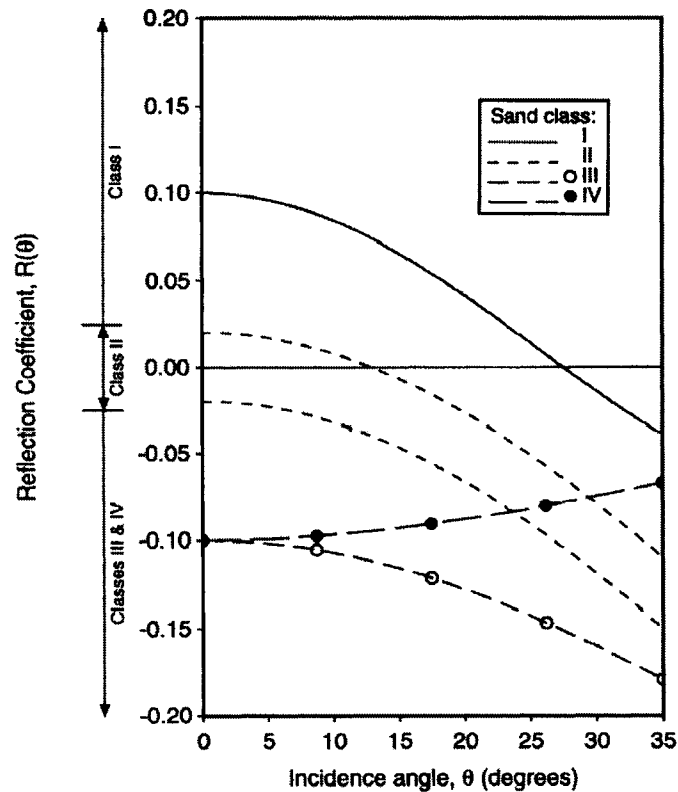


Figure 6.4: P-wave reflection coefficient at the top of class I, II, III and IV gas sands, figure from Castagna et al. (1998) with permission to use granted by the Society of Exploration Geophysics.

In the applied geophysics literature, the use of these variations in amplitude with angle of incidence are variously referred to as 'Amplitude versus Angle' (AVA) or 'Amplitude versus Offset' (AVO). The use of AVO is clear when one considers that a change in the angle of incidence at the geological reflection point can only be achieved by increasing the offset between the seismic source and the receiver.

AVO analysis is also finding use in time lapse seismic analysis. Time-lapse seismic analysis is a procedure where a reservoir is monitored at several time steps while the reservoir is being depleted. The main purpose of time-lapse studies is to map the typical reservoir parameters changes such as the pore pressure changes and fluid saturation changes during production and enhanced oil recovery (EOR) processes. The consequent changes in seismic properties due to these reservoir changes depend on the combined effects of the pressure and saturation changes. One of the examples is that saturation changes because water will displace oil after injection, while the reservoir pressure may decrease during hydrocarbon extraction or increase due to water injection. To better understand the time-lapse data, the relationship between seismic parameters and the reservoir parameters has been extensively studied in laboratory and theory as well. Many investigations showed that the pore pressure is one of the most important factors in controlling the acoustic wave velocities in sandstones and conglomerates, the P- and S-wave velocities generally increases with the decreasing reservoir pressure. The water saturation increase because of the water injection during oil production will decrease the P-wave velocity. These velocities changes means that the reservoir changes might produce an observable changes in seismic impedance.

One of the potential methods for mapping the changes in the reservoir is to apply Amplitude Variation with Offset AVO analysis. The seismic properties changes in response to the reservoir parameters changes may produce noticeable changes of AVO responses, which in turn provide an important method to map the reservoir pressure changes and fluid migration through AVO responses on a time scale (Tsingas and Kanasewich, 1991; Tura et al., 1999). To examine the feasibility of time lapse studies, the amplitude changes with effective pressure and angle of incidence is studied based on the experimental measurement of P- and S-wave velocities. One of the most commonly used theories in AVO analysis is to use Zoeppritz's equation. The pressure sensitivity of P-P and P-SV reflection coefficient was performed on a simple two-layer model interface using the complete Zoeppritz's equations.

6.2 Zoeppritz's equations

The reflected and transmitted P- and S-wave velocity depends on the contrast in the physical properties such as the density, P- and S-wave velocities across the boundary. Based on the boundary conditions which assume continuity of the displacement and traction across the boundary, the energy partitioning of the incident P- or S-wave to reflected and transmitted P- and S-wave on a two layer interface can be described by the Zoeppritz's equations (Aki & Richard, 1980). The most commonly used equations from these equations are the reflected P-wave (P-P) and converted SV (P-SV) from an incident P-wave. In standard layered medium there is a second set of equations to describe the decoupled SH reflectivity problem, but we focus here only on the P-P and P-SV coupled

problem which is used in practice. The reflectivity coefficient of P-P ($\overset{\vee}{P}\overset{\vee}{P}$) and P-SV ($\overset{\vee}{P}\overset{\vee}{S}$) in terms of angle of incident can be expressed as follows (Aki & Richard, 1980):

$$R_{PP} = \left[\left(b \frac{\cos i_1}{V_{P1}} - c \frac{\cos i_2}{V_{P2}} \right) F - \left(a + d \frac{\cos i_1}{V_{S1}} \frac{\cos j_2}{V_{S2}} \right) H p^2 \right] / D \quad (6.2)$$

$$R_{PSV} = -2 \frac{\cos i_1}{V_{P1}} \left(ab + cd \frac{\cos i_2}{V_{P2}} \frac{\cos j_2}{V_{S2}} \right) p V_{P1} / (V_{S1} D) \quad (6.3)$$

In these two equations:

$$a = \rho_2 (1 - 2V_{S2}^2 p^2) - \rho_1 (1 - 2V_{S1}^2 p^2) \quad (6.4)$$

$$b = \rho_2 (1 - 2V_{S2}^2 p^2) + 2\rho_1 V_{S1}^2 p^2 \quad (6.5)$$

$$c = \rho_1 (1 - 2V_{S1}^2 p^2) + 2\rho_2 V_{S2}^2 p^2 \quad (6.6)$$

$$d = 2(\rho_2 V_{S2}^2 - \rho_1 V_{S1}^2) \quad (6.7)$$

$$E = b \frac{\cos i_1}{V_{P1}} + c \frac{\cos i_2}{V_{P2}} \quad (6.8)$$

$$F = b \frac{\cos j_1}{V_{S1}} + c \frac{\cos j_2}{V_{S2}} \quad (6.9)$$

$$G = a - c \frac{\cos i_1}{V_{P1}} \frac{\cos j_2}{V_{S2}} \quad (6.10)$$

$$H = a - d \frac{\cos i_2}{V_{P2}} \frac{\cos j_1}{V_{S1}} \quad (6.11)$$

$$D = EF + GH p^2 \quad (6.12)$$

where i_1, i_2 represent the reflected and transmitted angles for P-wave; j_1, j_2 represent reflected and transmitted angles of S-wave respectively; ρ_1, V_{P1}, V_{S1} are the density, P-

and S-wave velocities in the upper media; ρ_2, V_{P2}, V_{S2} are the density, P- and S-wave velocities in the lower media.

There are many different simplifications of these equations that are intended to simplify analysis of AVA observations. One of the most popular simplifications was developed by Shuey (1985), it is only applicable at low incidence angles. According to Shuey's approximation the P-wave reflection coefficient as a function of angle of incidence can be simplified to:

$$R_{PP}(i_1) \cong R_{P0} + \left[\frac{A_0 R_{P0} + \Delta v}{(1 - v^2)} \right] \sin^2(i_1) + \frac{1}{2} \frac{\Delta V_P}{V_P} [\tan^2(i_1) - \sin^2(i_1)] \quad (6.13)$$

$$A_0 = B_0 - 2(1 + B_0) \frac{1 - 2v}{1 - v} \quad (6.14)$$

$$B_0 = \frac{\Delta V_P / V_P}{\Delta V_P / V_P + \Delta \rho / \rho} \quad (6.15)$$

$$R_{P0} \cong \frac{1}{2} \left(\frac{\Delta V_P}{V_P} + \frac{\Delta \rho}{\rho} \right) \quad (6.16)$$

Often, Shuey's formula is written in shorter form as

$$R_{PP}(i_1) = A + B \sin^2(i_1) + C [\tan^2 i_1 - \sin^2 i_1] \quad (6.17)$$

where A , B , and C may be found by direct comparison to Shuey's full approximation.

Usually, for small angles $< 30^\circ$, $[\tan^2 i_1 - \sin^2 i_1]$ is small and the third constant C is ignored and then equation 6.17 takes the form of a simple line with independent variable $\sin^2(i)$, intercept A , and gradient B . Note that A represents the normal incidence P-wave reflection coefficient (given by equation 6.1 above).

Equation 6.17 is not really necessary for the calculation of the $R_{pp}(\theta)$ as it requires just as much information as the full elastic Zoeppritz solution (equation 6.2~6.12)

However, in the opposite sense it is employed as one way to simply condense the information contained in an observed AVA curve. In practice, an observed AVA curve is transformed from amplitude $R_{pp}(\theta)$ versus angle θ space to amplitude $R_{pp}(\theta)$ versus $\sin^2\theta$ space. The observations which fall along a curved AVA line will then follow a linear trend upon transformation which, after applying linear regression, can be described by only intercept A and gradient B (e.g., Tigrek et al., 2005). Broadly, an AVO curve whose reflected amplitude becomes more negative with angle will have a negative gradient. An AVO curve whose amplitude becomes increasingly positive with angle of incidence will have a positive gradient.

One way to facilitate an interpretation of such information is to simply plot A versus B (Smith and Gidlow, 1987); a classification can then be given to the curve on the basis of where it falls in A-B space. Figure 5 (from Castagna et al, 1998) shows the fields of the differing classifications with this A-B space (Castagana, 1993, Castagna and Smith, 1994).

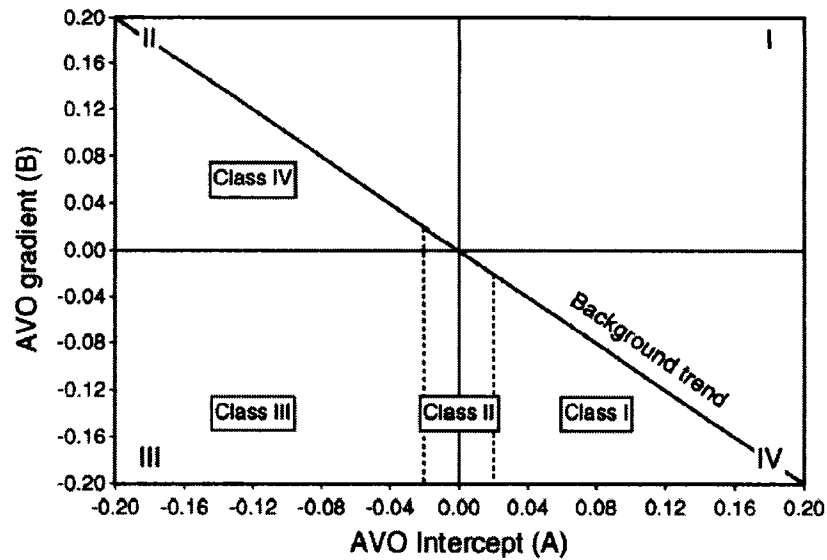


Figure 6.5: AVO gradient versus AVO intercept crossplot showing the differing classifications within the A-B space. Quadrants of this space are numbered from I to IV in a counterclockwise fashion, figure from Castagna et al., 1993 with permission to use granted by Society of Exploration Geophysicists.

6.3 Petrophysical sensitivity of reflection coefficient

The results of the previous chapters demonstrate the dependence of the P and S wave velocities of the Cadotte formation on both effective pressure and saturation state. As noted earlier, the Cadotte is an important gas reservoir in the Western Canada Sedimentary Basin; consequently, any information that may be obtained from acquired seismic data that will improve the opportunity for detecting gas over water filled zones can have economic value. In this section, the influence of both effective pressure and fluid saturation on the AVA responses for a simple geological interface are calculated for illustrative purposes. These calculations employ the full elastic Zoeppritz equations given

above, although the calculations are carried out via the more general scattering matrix approach developed by Aki and Richards (1980) and implemented in Matlab™.

For the numerical model, it is assumed that an incident plane P-wave is reflected on the two-layer interface with the density, P- and S-wave velocities in each layer given in table 6.1. The Upper layer is assumed to be a shale layer; while the lower layer is the conglomerate layer with the experimentally measured and Gassmann's equation predicted P- and S-wave velocity of the water-saturated sample. Figure 6.6 and 6.7 shows that P-wave and S-wave reflection for dry and water saturated conglomerate layer. There are relatively large amplitude changes at large angle of incidence and small amplitude changes at small angle of incidence. At high effective pressure (45 MPa), the changes of P-P and P-SV reflectivity can be hardly noticed after the dry sample is saturated with water (Figure 6.6) because of the low velocity contrast between the dry and water saturated velocities, however, the changes of P-P and P-SV reflection coefficient after the sample is saturated water becomes larger at low effective pressure (Figure 6.7).

Figure 6.8 and 6.9 shows P-P (a) and P-SV (b) reflection coefficient as a function of angle of incidence and effective pressure. The velocities used in the lower layer for Figure 6.8 are the Gassmann's equation predicted velocities of the water-saturated sample (SB007); the velocities in the lower layer for Figure 6.9 are the experimentally measured velocities of the water-saturated sample (SB007). The P-P reflection coefficient increases remarkably with increasing effective pressure at the low angle of incidence; however, it hardly changes with effective pressure at the higher angle of incidence. The P-P reflection coefficient is more sensitive to effective pressure at the low-pressure areas. However, the angle dependency is much stronger in high-pressure areas. The P-P

reflection coefficient normally decreases with increasing incident angle. But when the velocity of the lower layer is less than the velocity of the upper layer, the P-P reflection coefficient will increase with the angle of incidence.

Contrary to the P-P reflection coefficient, the P-SV reflection coefficient shows little changes with the variation of effective pressure at low angle of incidence; however, it shows remarkable changes at high angle of incidence. Just the same as the P-P reflection coefficient, the angle dependence of P-SV reflection coefficient is more obvious at high effective pressure.

The gradient and intercept (Figure 6.10) are calculated from the amplitude versus $\sin^2(\theta)$ at different effective pressures by a linear regression analysis. From the figure, we can see that the gradient of the P-P reflection coefficient changes decreases with increasing effective pressure and it changes more rapidly at low effective pressure. At low effective pressure, the gradient of the P-P reflectivity has a positive value that means the reflection coefficient increases with angle with incidence. At high effective pressure, however, the gradient has a negative value that means the reflection coefficient decreases with angle of incidence. The intercept for the P-P reflection shows an increase with effective pressure. Figure 6.11 shows the crossplot of the AVO gradient and AVO intercept for the simple two layer model using the velocities of dry and water saturated sands at different pressures. Both A and B become more positive when the sandstone layer is saturated with water. At low confining pressures, both the dry and water saturated AVO curves fall in the class IV zone of quadrant II but these migrate into a class I sands in quadrant IV with only a small amount of increase in the confining pressure. The dry and the saturated curves approach one another with increasing

confining pressure also. This may suggest that detection of gas saturated zones relative to water saturated zones on the basis of differences in the AVO curves of these rocks may be difficult, particularly at high confining pressures.

These differences may even be less when the influence of effective pressure on the rock velocities is considered. One related factor that was mentioned in earlier presentations of the geology at the area is that the gas saturated zones in the Cadotte appear to be underpressured relative to the water saturated zones at the same depth (Figure 4.6). As such, the gas saturated rock will be subject to a larger *effective* confining pressure which has the consequence of making stiffening the rock and increasing its seismic velocity such that it will approach that for an equivalent water saturated rock at the same elevation. In the A-B space plot above, the gas saturated values would come even closer to the water saturated values making it even more difficult to distinguish gas from water saturated zones.

Table 6.1: The density, P- and S-wave velocities of each layer on a simple two-layer model. The parameters used in layer two are based on the lab measurement of sample SB007.

		V _P (m/s)	V _S (m/s)	Density (Kg/m ³)
Layer 1		4000	2300	2300
Layer 2	Dry	3065~4922	1811~3242	2473
	Theoretical	3688~5011	1834~3199	2498
	Experimental	4250~5051	2224~3231	2498

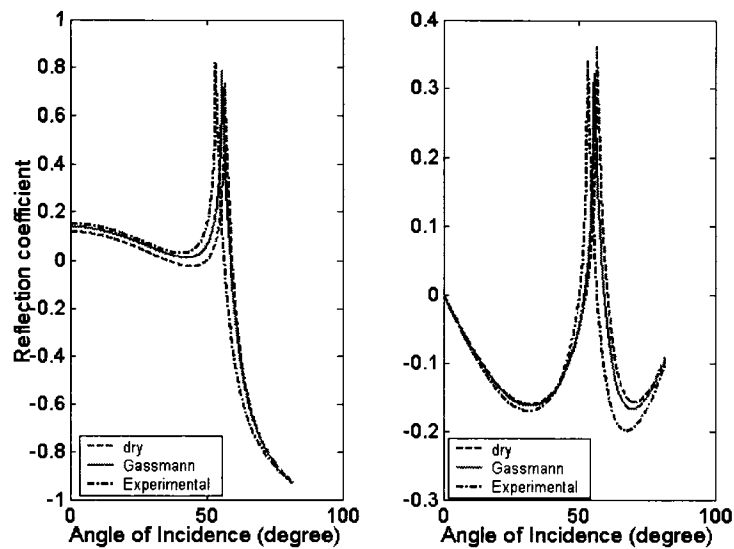


Figure 6.6: P-P and P-SV reflection coefficient as a function of angle of incidence on a two layer isotropic interface. The V_p , V_s and density of the lower layer are the experimental values of sample SB007 at effective pressure 45MPa.

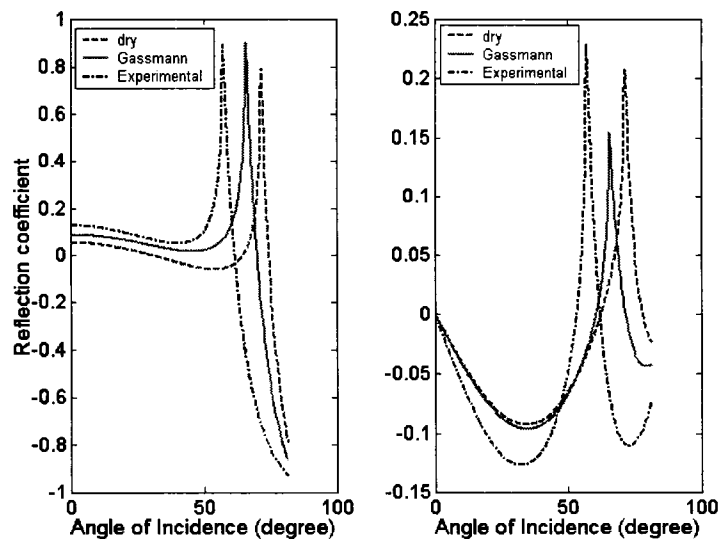


Figure 6.7: P-P and P-SV reflection coefficient as a function of angle of incidence on a two layer isotropic interface. The V_p , V_s and density of the lower layer are the experimental values of sample SB007 at effective pressure 20MPa.

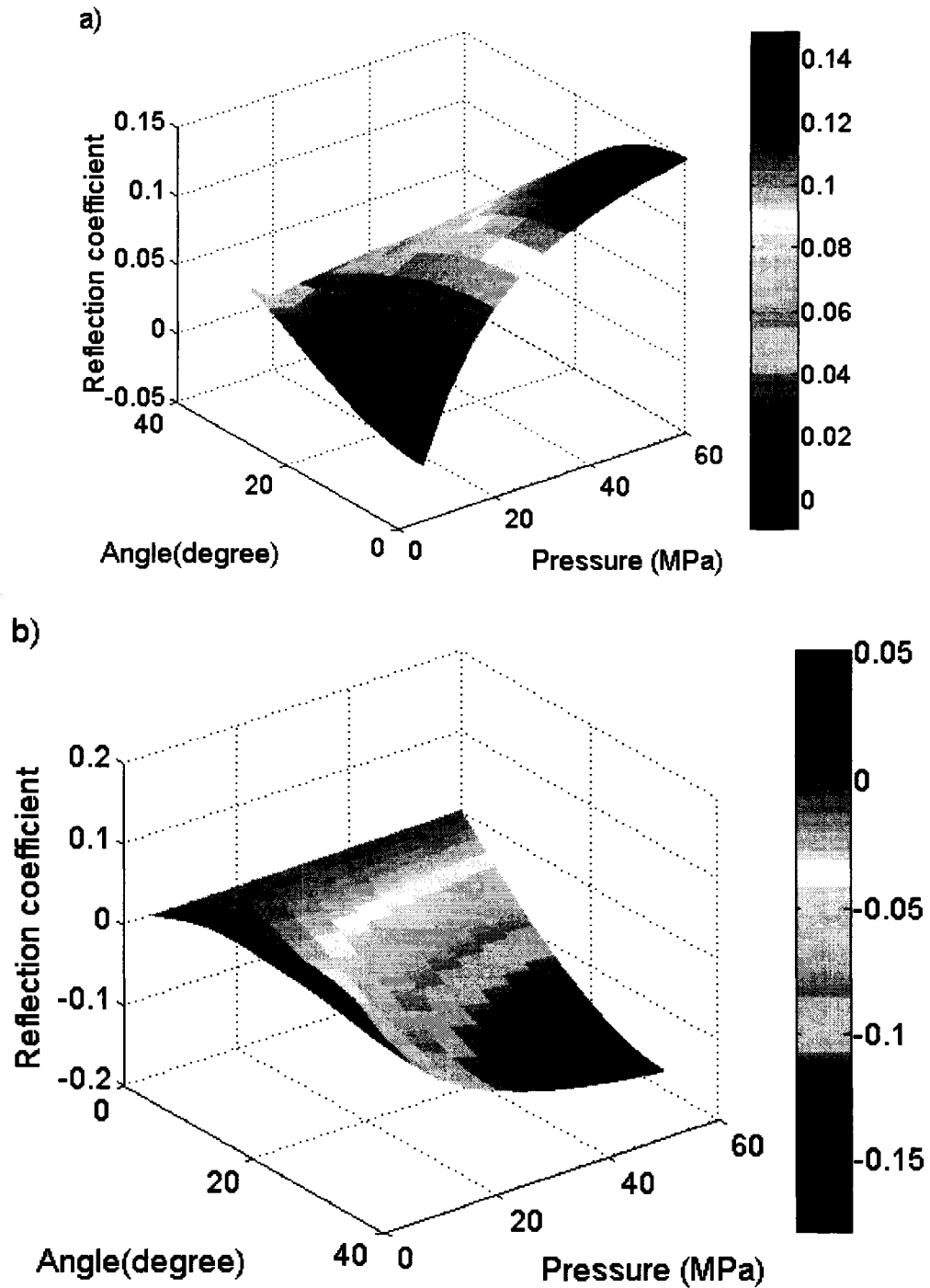


Figure 6.8: P-P (Figure a) and P-SV (Figure b) reflection coefficient as a function of angle of incidence and pressure. The velocities in the lower layer are the Gassmann's equation predicted velocities of the water-saturated sample SB007.

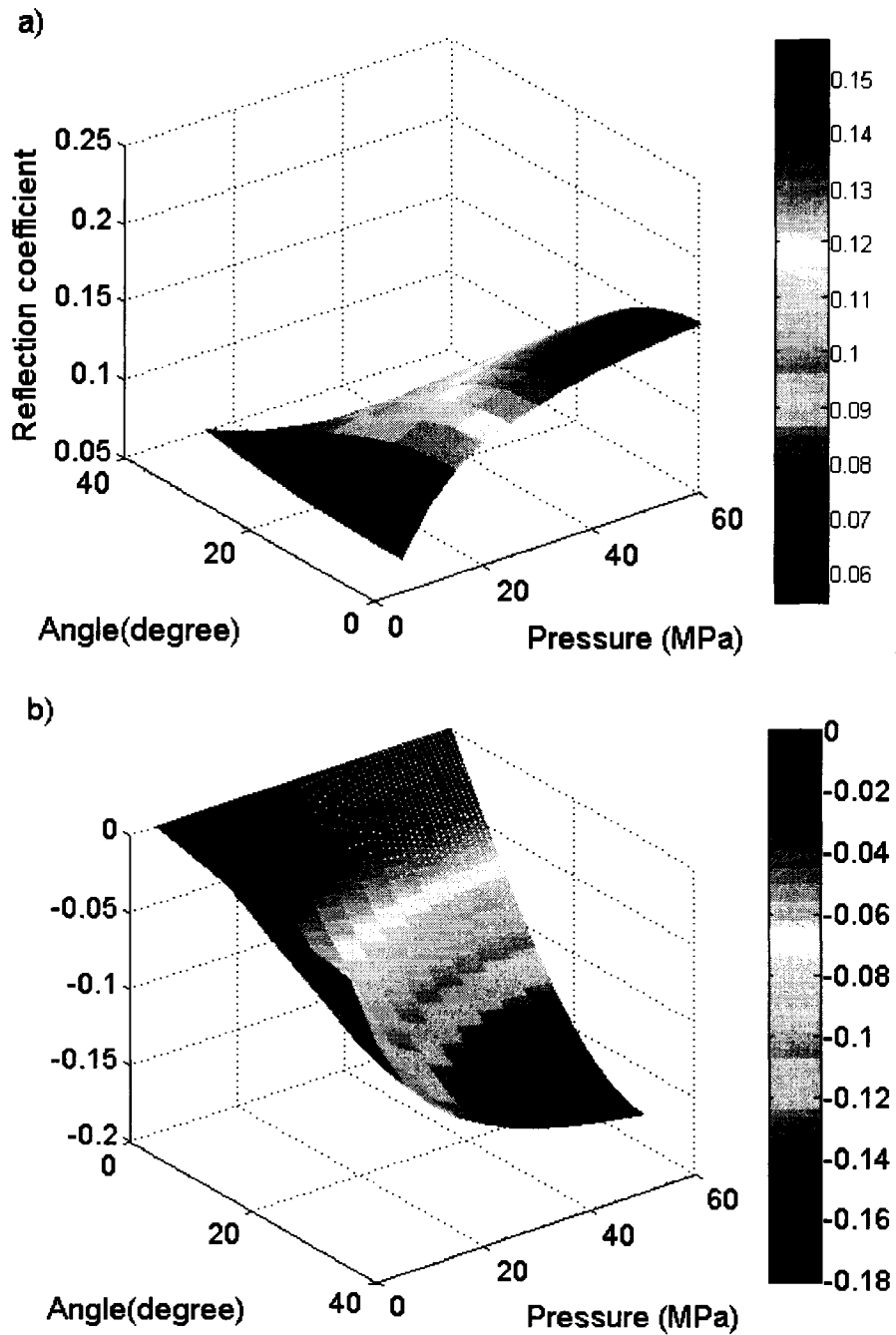


Figure 6.9: P-P (Figure a) and P-SV (Figure b) reflection coefficient as a function of angle of incidence and pressure. The velocities in the lower layer are the experimentally measured velocities of the water-saturated sample SB007.

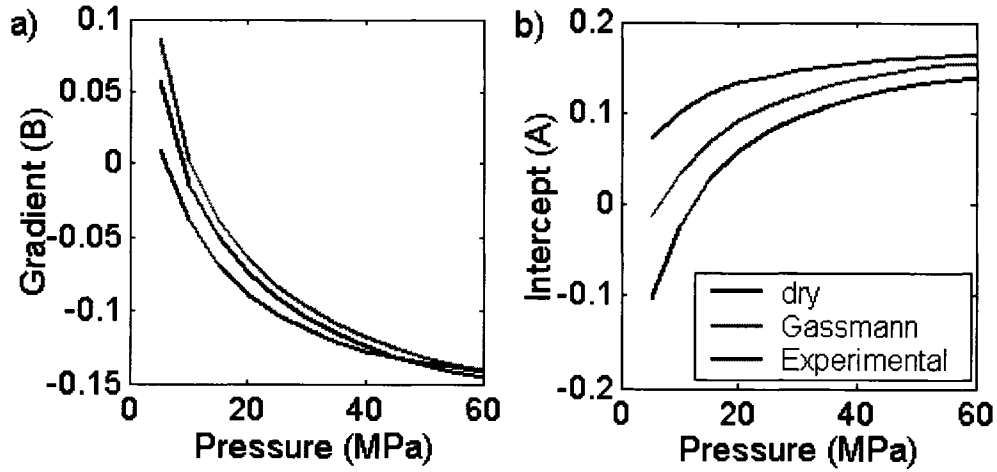


Figure 6.10: A and B as a function of effective pressure. The velocities in the lower layer are the dry, experimentally measured and Gassmann's equation predicted velocity values of the water-saturated sample

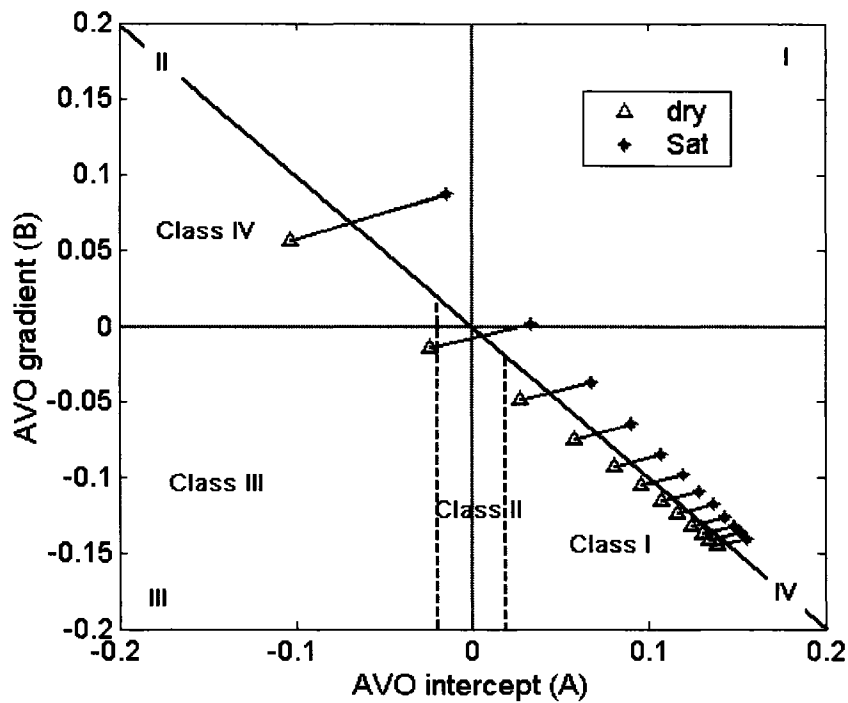


Figure 6.11: The AVO gradient and AVO intercept for the simple two layer model using the velocities of dry and water saturated sands as calculated using Gassmann's Eqn. 2.13 at different pressure. The intercept (A) increases with the increasing effective pressures.

6.4 Summary

The background of AVA analysis was first briefly described in the beginning of this Chapter. Base on the velocity result of the experimental measurement, the pressure sensitivity of P-P and P-SV reflection coefficient was performed. The results shows that the P-P reflection coefficient are more sensitive to effective pressure at the low angle of incidence and more sensitive to effective pressure at the low-pressure areas. The P-SV reflection coefficient, however, shows little change with the variation of effective pressure at low angle of incidence. Just the same as the P-P reflection coefficient, the angle dependence of P-SV reflection coefficient is more obvious at high effective pressure.

Chapter 7

Conclusion

7.1 Summary of work in the thesis

The purpose of this study is to investigate the effect of pore and confining pressure and water saturation on elastic properties of conglomerate and sandstone. To accomplish this, the conventional ultrasonic transmission technique was employed to determine the compressional and shear wave velocity using our recently updated high-pressure instrument, which now includes pore pressure setup. The new method of making transducers also gives us an improved velocity precision that is less than 0.2%.

The main mechanism of the pressure dependency of the P- and S-wave velocity is the closing of microcracks under stress. Both of the images of thin section and SEM and porosimetry analysis demonstrate that microcracks exist in these rocks, which only represent only a small portion of total porosity. The SEM also shows that quartz overgrowth and quartz cement constitute most of the materials between the grain contact and on the grains. Some of the quartz overgrowth is covered with clays.

As expected, P- and S-wave velocities are all highly pressure dependent for these samples. They increase with the progressively loading of stress. The increasing rate is much higher at low effective pressure than high effective pressures because most of the microcracks are closed at relatively low pressure. As predicted by Gassmann's equation,

the P-wave velocity increases after the samples are saturated with water. However, an unexpected S-wave velocity increase at relatively lower pressure was observed, which can be attributed to the frequency dispersion; the microcracks that cause local fluid flow. This is further demonstrated by the observation that deviation of the experimentally measured P- and S-wave at ultrasonic frequencies from the Gassmann's equation calculated velocities decreases abruptly with increased effective pressure, which means the Gassmann's equation become valid when the microcracks are closed. The elastic coefficient n relating to the pore and confining pressure is also pressure dependent. It is also interesting to note that n for the P-wave velocities is less than the n for the S-wave.

Based on the laboratory experimental result, we also performed pressure sensitivity analysis of AVA responses on a simple two-layer model in order to better understand time-lapse seismic data. The results shows that the P-P reflection coefficient is more sensitive to effective pressure at the low angle of incidence and more sensitive to effective pressure at the low-pressure areas. The P-SV reflection coefficient, however, shows little changes with the variation of effective pressure at low angle of incidence. Just the same as the P-P reflection coefficient, the angle dependence of P-SV reflection coefficient is more obvious at high effective pressure. However, distinguishing gas from water saturated zones on the basis of an amplitude versus offset signature may be challenging. The fact that the gas saturated zones will be at a higher effective confining pressure due to pore pressures that are below those in an equivalent water saturated zone may make seismic discrimination of these zones even more difficult.

7.2 Contributions of this work

There are three principle contributions of the work in this thesis.

- 1) Development of a new methodology for simultaneous determination of both P-wave and S-wave velocity under conditions of pressure. A major part of this work included the technical development and calibration of the system for obtaining ultrasonic waveforms under conditions of confining and pore pressure, including the capacity to subject the pore space to a vacuum. This allowed for precise measurements of the velocity.
- 2) Application of the laboratory results to illustrate the influence of effective pressure and saturation conditions on amplitude versus offset curves. To our knowledge, this is the only study in which such laboratory studies have been applied to see how real in situ conditions may influence a seismic exploration program. The laboratory work here suggests that, at higher effective confining pressures and assuming that Gassmann's Eqn 2.13 applies to low frequency seismic waves, it may be difficult to clearly distinguish the desired gas saturated from uneconomic water saturated zones.
- 3) Development of a sample characterization protocol. In this thesis a number of tools were used to characterize the rock that included scanning electron microscopy, optical microscopy, and a variety of porosimetry techniques in addition to the more novel velocity measurements. The characterization suggested that the rocks contained dual porosity pore space; the finer crack-like pores are in good agreement with the highly nonlinear elastic behaviour of the rocks with respect to effective pressures.

7.3 Recommendations and future research directions

The focus of this thesis was primarily on the application of the laboratory measurements to a real exploration problem. While the AVO analysis of Chapter 6 does provide an interesting illustration of possible rock physics influences on seismic reflections in the area, the work would in future be greatly improved by access to real industry data for comparison's sake. It must be noted, however, that obtaining modern high quality data is problematic due to proprietary issue.

The work of the thesis has raised some new questions that were beyond the immediate research goals, however.

First, as has been seen in many previous studies, the observed P and S wave velocities for the saturated rock substantially exceed those predicted using Gassmann's equation particularly at the lower effective confining pressures. However, one unique observation in this study is that, in the single additional experiment carried out on SB007 to 100 MPa of confining pressure, Gassmann's equation does predict well both the P and S wave velocities at the higher pressures. This may suggest that the influence of microcracks on the wave propagation at ultrasonic frequencies is eliminated once the microcracks are sufficiently closed. More experimental and theoretical work is required on this observation.

Second, in general one conclusion is that the effective pressure coefficient 'n' is close to, but not exactly, equal to unity. However, this current analysis has not taken into account all the possible influences such as the increase in the bulk modulus and density of the experimental results with this in mind.

Finally, the AVO analysis of Chapter 6 assumed that the 'dry' values are representative of the gas saturation. However, this analysis did not account for the influence of both pressure and temperature on the elastic properties of methane. Indeed, under expected in situ conditions the elastic properties of methane may not be so easily ignored and may further narrow the differences with water saturated zones.

References

- Aki, K., and Richard, P.G., 1980, Quantitative seismology: Theory and Methods: W. H. Freeman and Company.
- Avseth, P., Dvorkin, J. and Mavko, G., 2000, Rock physics diagnostic of north sea sands: Link between microstructure and seismic properties: *Geophysical Research Letters*, 27, 2761-2764.
- Berryman, J. G., 1999, Origin of Gassmann's equations: *Geophysics*, 64, 1627-1629.
- Baechle, H. T., Weger, R. J., and Eberli, G. P., 2005, Changes of shear moduli in carbonage rocks: implications for Gassmann applicability: *The leading edge*, 507-510.
- Banthia, B. S., King, M. S., and Fatt, I., 1965, Ultrasonic shear-wave velocities in rocks subjected to simulated overburden pressure and internal pore pressure: *Geophysics*, 30, 117-121.
- Bass, J. D., 1995, Elasticity of minerals, glasses, and melts, *in* T.J. Ahrens, ed., *Mineral Physics and Crystallography: A Handbook of Physical Constants*, American Geophysical Union, Washington, D.C., 45-63.
- Batzle, M. L., Simmons, G. and Siegfried, R. W., 1980, Microcrack closure in rocks under stress: direct observation: *Journal of Geophysical Research*, 85, 7072-7090.

- Batzle, M. and Wang, Z., 1992, Seismic properties of pore fluids: *Geophysics*, 57, 1396-1408.
- Beaumont, C., 1981, Foreland basins: *Geophysical Journal of the Royal Astronomical Society*, 65, 291-329.
- Biot, M. A., 1956, Theory of propagation of elastic waves in a fluid-saturated porous solid: I. Low frequency range: *Journal of the Acoustical Society of America*, 28, 168-178.
- Biot, M. A., 1956, Theory of propagation of elastic waves in a fluid-saturated porous solid: II. higher frequency range: *Journal of the Acoustical Society of America*, 28, 179-191.
- Biot, M. A., 1962, Mechanisms of deformation and acoustic propagation in porous media: *Journal of Applied Physics*, 33, 1482-1498.
- Brace, W. F., Silver, E., Hadley, K., and Goetze, C., 1972, Cracks and pores: A closer look: *Science*, 178, 162-764.
- Brakel, V. J., ed., 1981, A Special Issue Devoted to Mercury Porosimetry: *Powder Technology*, 29, 1-209.
- Cant, D. J., 1986, Diagenetic traps in sandstones: *AAPG Bulletin*, 70(2): 155-160.
- Carcione, J. M., and Tinivella, U., 2001, The seismic response to overpressure: A modelling study based on laboratory, well and seismic data: *Geophysical Prospecting*, 49, 523-539.
- Carlson R. L., and Gangi, A. F., 1985, Effects of cracks on the pressure dependence of P wave velocities in crystalline rocks: *Journal of Geophysical Research*, 90, 8675-8684.

- Castagna, J. P., 1993, Petrophysical imaging using AVO: The Leading Edge, 172-178.
- Castagna J. P., Batzle M. L. and Eastwood R. L. 1985, Relationships between compressional-wave and shear-wave velocities in clastic silicate rocks: *Geophysics*, 50, 571-581.
- Castagna, J. P., and Smith, S. W., 1994, Comparison of AVO indicators: A modeling study: *Geophysics*, 59, 1849-1855.
- Castagna, J. P., Swan H. W., and Foster D. J., 1998, Framework for AVO gradient and intercept interpretation: *Geophysics*, 63, 948–956.
- Christensen, N. I. and Wang H. F., 1985, The influence of pore pressure and confining pressure on dynamic elastic properties of Berea sandstone: *Geophysics*, 50, 207-213.
- Davis, T. B., 1984, Subsurface pressure profiles in gas-saturated basins, *in* J.A. Masters, ed., *Elmworth: Case study of a Deep basin gas field: AAPG Memoir 38*, 189-203.
- Dvorkin, J., and Nur, A., 1993, Dynamic poroelasticity: A unified model with the squirt and the Biot mechanisms: *Geophysics*, 58, 524-533.
- Eberhart-Phillips, D., Han, D-H, and Zoback, M. D., 1989, Empirical relationships among seismic velocity, effective pressure, porosity, and clay content in sandstone: *Geophysics*, 54, 82-89.
- Eshelby, J. D., 1957, The Determination of the Elastic Field of an Ellipsoidal Inclusion and Related Problems: *Proceedings of Royal Society of London*, A241, 376–396.

- Freund, D., 1992, Ultrasonic compressional and shear velocities in dry clastic rocks as a function of porosity, clay content, and confining pressure: *Geophysical Journal International*, 108, 125-135.
- Gassmann, F., 1951, Elasticity of porous media: *Über die Elastizität poroser Medien: Vierteljahrsschrift der Naturforschenden Gesellschaft in Zurich*, 96, 1-23.
- Gist, G. A., 1994, Interpreting laboratory velocity measurements in partially gas-saturated rocks: *Geophysics*, 59, 1110-1109.
- Goertz, D., and Knight, R. J., 1998, Elastic wave velocities during evaporative drying: *Geophysics*, 63, 171-183.
- Green, D. H., and Wang, H. F., 1986, Fluid pressure response to undrained compression in saturated sedimentary rock: *Geophysics*, 51, 948-956.
- Han, D-H., Nur, A. and Morgan, D., 1986, Effects of porosity and clay content on wave velocities in sandstones: *Geophysics*, 51, 2093-2107.
- Hayes, B. J. R., Christopher, J. E., Rosenthal, L., Los, G., McKercher, B., Minken, D., Tremblay, Y. M. and Fennell, J., 1994, Cretaceous Mannville Group of the Western Canadian Sedimentary Basin. In: Mossop, G. D. and Shetsen, I., *Geological Atlas of the Western Canada Sedimentary Basin*. Canadian Society of Petroleum Geologists and the Alberta Research Council, Calgary, 317-334.
- Hunter, R. E., Clifton, H. E. and Phillips, R. L., 1979, Depositional processes, sedimentary structures, and predicted vertical sequences in barred nearshore systems, southern Oregon coast: *Journal of Sedimentary Petrology*, 49 (3): 711-726.

- Hutcheon, I., 1990, Aspects of the diagenesis of coarse-grained siliclastic rocks. *In* I.A. McIlreath, and D.W. Morrow, ed., Diagenesis, Geological Association of Canada: Reprint Series, 4, 165-176.
- Jones, S. M., 1995, Velocities and quality factors of sedimentary rocks at low and high effective pressure: *Geophysical Journal International*, 123, 774-780.
- Khazanehdari, J., and Sothcott, J., 2003, Variation in dynamic elastic shear modulus of sandstone upon fluid saturation and substitution: *Geophysics*, 68, 472-481.
- Khaksar, A., Griffiths, C. M., and McCann C., 1999, Compressional- and shear-wave velocities as a function of confining stress in dry sandstones: *Geophysical Prospecting*, 47, 487-508.
- King, M. S., 1966, Wave velocities in rocks as a function of changes in overburden pressure and pore fluid saturants: *Geophysics*, 31, 50-73.
- King, M. S., Marsden, J. R., and Dennis, J. W., 2000, Biot dispersion for P- and S-wave velocities in partially and fully saturated sandstones: *Geophysical prospecting*, 48, 1075-1089.
- King, M. S., and Marsden, J. R., 2002, Velocity dispersion between ultrasonic seismic frequencies in brine-saturated reservoir sandstone: *Geophysics*, 67, 254-258.
- Kirstetter, O., and MacBeth, C., 2001, Compliance-based interpretation of dry frame pressure sensitivity in shallow marine sandstone: *SEG Expanded Abstracts*, 2132–2135.
- Kozlov E.A., 2004, Pressure-dependent seismic response of fractured rock: *Geophysics*, 69, 885-897.

- Kuster, G. T., and Toksöz, M. N., 1974, Velocity and attenuation of seismic waves in two-phase media—Part I: Theoretical formulations: *Geophysics*, 39, 447-472.
- Lo, T. W., Coyner, K. B., and Toksöz, M. N., 1986, Experimental determination of elastic anisotropy of Berea sandstone, Chicopee shale, and Chelmsford granite: *Geophysics*, 51, 164-171.
- MacBeth, C., 2004, A classification for the pressure-sensitivity properties of a sandstone rock frame: *Geophysics*, 69, 497-510.
- Mackenzie, J. K., 1950, The Elastic Constants of a Solid Containing Spherical Holes: *Proceedings of Physical Society of London*, B63, 2–11.
- Masters, J. A., 1979, Deep Basin gas trap, western Canada: *AAPG Bulletin*, 63(2),152-181.
- Masters, J. A., 1984, Lower Cretaceous oil and gas in Western Canada, *in* J.A. Masters, ed., *Elmworth: Case study of a Deep basin gas field: AAPG Memoir 38*, 1-33.
- Mayr S. I., and Burkhardt, H., 2006, Ultrasonic properties of sedimentary rocks: effect of pressure, saturation, frequency and microcracks: *Geophysical Journal International*, 164, 246-258.
- Molyneux, J. B., and Schmitt, D. R., 1999, First break timing: Arrival onset times by direct correlation: *Geophysics*, 64, 1492-1501.
- Molyneux, J. B., and Schmitt, D. R., 2000, Compressional-wave velocities in attenuating media: A laboratory physical modelling study: *Geophysics*, 65,1162-1167.

- Mossop, G. D., and Shetsen, I., 1994, Geological atlas of the Western Canada Sedimentary Basin: Canadian Society of Petroleum Geologists and Alberta Research Council, Calgary, Alberta.
- Nicholas, M. E., Joyner, P. A., Tessem, B. M., and Olson, M. D., 1961, The effect of various gases and vapors on the surface tension of mercury: *Journal of Physical Chemistry*, 65(8), 1373-1375.
- Nur, A. M., Walls, J. D., Winkler, K., and DeVilbiss, J., 1980, Effects of fluid saturation on waves in porous rock and relations to hydraulic permeability: *Society of Petroleum Engineers Journal*, 20(6), 450-458.
- O'Connell, R. J., and Budiansky, B., 1974, Seismic velocities in dry and saturated cracked solids: *Journal of Geophysical Research*, 79, 5412-5426.
- Ostrander, W. J., 1984, Plane-wave reflection coefficients for gas sands at nonnormal angles of incidence: *Geophysics*, 49, 1637-1648.
- Pickett, G. R., 1963, Acoustic character logs and their application in formation evaluation: *Journal of Petroleum Technology*, 15, 650-667.
- Prasad, M., and Manghnani, M. H., 1997, Effects of pore and differential pressure on compressional wave velocity and quality factor in Berea and Michigan sandstones: *Geophysics*, 62, 1163-1176.
- Ravalec M. L., and Guéguen Y., 1996, High- and low-frequency elastic moduli for a saturated porous/cracked rock-Differential self-consistent and poroelastic theories: *Geophysics*, 61, 1080-1094.

- Reinprecht, J. P., 2005, The cadotte member of the Boulder Creek Formation, Commotion Creek and Dokie Ridge, Northeast British Columbia: Master thesis, University of Alberta.
- Rutherford, S. R., and Williams R. H., 1989, Amplitude-versus-offset variations in gas sands: *Geophysics*, 54, 680-688.
- Shapiro, S. A., 2003, Elastic piezosensitivity of porous and fractured rocks: *Geophysics*, 68, 482-486.
- Shuey, R. T., 1985, A simplification of the Zoeppritz's equations: *Geophysics*, 50, 609-614.
- Simmons, G., and Brace, W. F., 1965, Comparison of static and dynamic measurements of compressibility of rocks: *Journal Geophysical Research*, 70, 5649-5656.
- Smith, D. G., Zorn, C. E., and Sneider, R. M., 1984, The paleogeography of the Lower Cretaceous of western Alberta and northeastern British Columbia in and adjacent to the Deep Basin of the Elmworth area. *in* J. A. Masters, ed., Elmworth: Case study of a Deep basin gas field: AAPG Memoir 38, 79-114.
- Smith, G. C., and Gidlow, P. M., 1987, Weighted stacking for rock property estimation and detection of gas: *Geophysical Prospecting*, 35, 993-1014.
- Sneider, R. M., King, H. R., Hietala, R. W., and Connolly, E. T., 1984, Integrated rock-log calibration in the Elmworth field: Alberta, Canada, *in* J. A. Masters, ed., Elmworth: Case study of a Deep basin gas field: AAPG Memoir 38, 205-282.
- Spencer, J. W., Cates M. E., and Thompson, D. D., 1994, Frame moduli of unconsolidated sands and sandstones: *Geophysics*, 59, 1352-1361.

- Tao, G., King, M. S., and Nabi-Bidhendi, M., 1995, Ultrasonic wave propagation in dry and brine-saturated sandstones as a function of effective stress: laboratory measurements and modelling: *Geophysical Prospecting*, 43, 299-327.
- Tatham R. H., 1982, V_p/V_s and lithology: *Geophysics*, 47, 336-344.
- Tiğrek, S., Slob, E. C., Dillen, M. W. P, Cloetingh, S. A. P. L., and Fokkema, J. T., 2005, Linking dynamic elastic parameters to static state of stress: toward an integrated approach to subsurface stress analysis, *Tectonophysics*, 397, 167-179.
- Todd T., and Simmons, G., 1972, Effect of pore pressure on the velocity of compressional waves in low-porosity rocks: *Journal of Geophysical Research*, 77, 3731-3743.
- Toksöz M. N., Cheng, C. H. and Timur, A., 1976, Velocities of seismic waves in porous rocks: *Geophysics*, 41, 621-645.
- Tsingas, C., and Kanasewich, E. R., 1991, Seismic reflection amplitude versus angle variations over a thermally enhanced oil recovery site: *Geophysics*, 56, 292-301.
- Tura, A, and Lumeley, D. E., 1999, Estimating pressure and saturation changes from time-lapse AVO data. *SEG Expanded Abstracts*, 1655-1658.
- Walls J. D., Nur, A. M., and Thierry B. T., 1982, Effects of pressure and partial water saturation on gas permeability in tight sands: experimental results: *Journal of Petroleum Technology*, 34(4), 930-936.
- Wang, Z., and Nur, A., 1992, Elastic wave velocities in porous media: A theoretical recipe, *in* Wang, Z., and Nur. A., Ed., *Seismic and acoustic velocities in reservoir rocks: Theoretical and model studies: Society of Exploration Geophysics*, 2, 1-35.

- Washburn, E. W., 1921, Note on a method of determining the distribution of pore sizes in a porous material: *Proceedings of the National Academy of Science*, 7, 115-116.
- Winkler K. W., 1986, Estimates of velocity dispersion between seismic and ultrasonic frequencies: *Geophysics*, 51, 183-189.
- Wyllie, M. R. J., Gregory, A. R., and Gardner, G. H. F., 1958, An experimental investigation of factors affecting elastic wave velocities in porous media: *Geophysics*, 23, 459-493.
- Walsh, J. B., 1965, The effect of cracks on the compressibility of rock: *Journal of Geophysical Research*, 70, 381-389.
- Zimmerman, R. W., Somerton, W. H., and King, M. S., 1986, Compressibility of porous rocks: *Journal Geophysical Research*, 91, 12765–12777.
- Zoeppritz, K., 1919, Erdbebenwellen VII. VIIb. Über Reflexion und Durchgang seismischer Wellen durch Unstetigkeitsflächen. *Nachrichten der Königlichen Gesellschaft der Wissenschaften zu Göttingen, Mathematisch-physikalische Klasse*, 66-84.

Appendix

Experimental Data of the Samples

Sample SB002 (dry)

P_c (Mpa)	P_p (Mpa)	V_p (m/s)	V_s (m/s)	κ (GPa)	μ (GPa)
5	0	4329.119	3099.343	15.166	24.553
10	0	4699.495	3306.436	19.192	27.944
15	0	4851.498	3381.030	21.203	29.219
20	0	4962.751	3450.846	22.368	30.438
25	0	5037.234	3496.216	23.198	31.244
30	0	5084.507	3538.880	23.398	32.011
35	0	5123.293	3564.823	23.782	32.482
40	0	5172.549	3593.654	24.375	33.010
45	0	5198.766	3613.320	24.587	33.372
50	0	5241.312	3630.955	25.287	33.698
55	0	5235.489	3661.966	24.360	34.276
60	0	5263.343	3673.183	24.827	34.487
55	0	5257.429	3669.328	24.764	34.414
50	0	5243.593	3662.087	24.574	34.279
45	0	5236.993	3656.528	24.536	34.175
40	0	5210.601	3640.649	24.226	33.879
35	0	5185.613	3625.682	23.933	33.601
30	0	5142.637	3605.105	23.305	33.220
25	0	5091.058	3576.869	22.647	32.702
20	0	5033.668	3535.364	22.168	31.947
15	0	4941.453	3489.577	20.913	31.125
10	0	4796.801	3410.290	19.177	29.727
5	0	4436.779	3249.640	14.326	26.992

Sample SB003 (dry)

P_c (Mpa)	P_p (Mpa)	V_p (m/s)	V_s (m/s)	κ (GPa)	μ (GPa)
5	0	4395.940	2778.065	23.007	19.655
10	0	4694.531	2863.631	28.281	20.884
15	0	4877.689	2994.867	30.135	22.842
20	0	4955.898	3072.080	30.503	24.035

25	0	5029.428	3130.324	31.146	24.955
30	0	5040.575	3151.107	30.989	25.288
35	0	5080.853	3184.181	31.316	25.821
40	0	5134.171	3217.798	31.972	26.370
45	0	5169.204	3241.406	32.373	26.758
50	0	5206.471	3277.456	32.560	27.356
55	0	5220.451	3296.095	32.515	27.668
60	0	5261.950	3326.916	32.930	28.188
55	0	5252.190	3323.979	32.735	28.139
50	0	5341.223	3404.417	33.299	29.517
45	0	5322.470	3383.626	33.269	29.157
40	0	5279.665	3352.729	32.820	28.627
35	0	5222.214	3319.707	32.032	28.066
30	0	5133.342	3273.230	30.729	27.286
25	0	5020.491	3204.328	29.326	26.149
20	0	4893.188	3128.925	27.733	24.933
15	0	4667.533	3003.072	24.859	22.968
10	0	4376.716	2957.552	19.082	22.277
5	0	3972.007	2886.915	11.879	21.225

Sample SB004 (dry)

P_C (Mpa)	P_P (Mpa)	V_P (m/s)	V_S (m/s)	κ (GPa)	μ (GPa)
5	0	4487.548	2889.761	21.309	19.764
10	0	4644.989	2979.786	23.045	21.014
15	0	4799.284	3000.595	26.101	21.309
20	0	4839.859	3056.878	25.951	22.116
25	0	4884.212	3074.053	26.639	22.365
30	0	5312.146	3270.338	33.036	25.312
35	0	5312.132	3305.020	32.316	25.852
40	0	5334.105	3316.348	32.633	26.029
45	0	5361.840	3333.860	32.968	26.305
50	0	5362.028	3342.933	32.781	26.448
55	0	5384.356	3355.084	33.092	26.641
60	0	5384.090	3364.127	32.894	26.785
55	0	5386.059	3362.774	32.973	26.763
50	0	5388.155	3341.420	33.478	26.424
45	0	5359.715	3341.000	32.763	26.418
40	0	5358.019	3324.840	33.060	26.163
35	0	5332.199	3311.500	32.686	25.953
30	0	5284.662	3281.523	32.115	25.485
25	0	5263.494	3231.887	32.607	24.720
20	0	5215.426	3190.059	32.263	24.085
15	0	5185.192	3170.351	31.914	23.788
10	0	5064.134	3078.414	30.791	22.428
5	0	4841.929	2972.626	27.601	20.913

Sample SB004 (water saturated)

P _C (Mpa)	P _P (Mpa)	V _P (m/s)	V _S (m/s)	κ (GPa)	μ (GPa)
5	0	4586.648	2697.150	27.525	17.661
10	0	4716.601	2838.942	27.919	19.566
15	0	4806.819	2925.377	28.392	20.776
20	0	4846.646	2976.323	28.352	21.506
25	0	4860.875	2992.444	28.376	21.739
30	0	4881.966	3022.609	28.288	22.180
35	0	4898.870	3042.613	28.296	22.474
40	0	4914.615	3061.969	28.289	22.761
45	0	4940.682	3080.437	28.545	23.037
50	0	4960.630	3106.334	28.506	23.426
55	0	4958.302	3113.383	28.308	23.532
60	0	4971.034	3116.425	28.554	23.578
55	0	4956.488	3110.984	28.313	23.496
50	0	4944.627	3106.318	28.122	23.425
45	0	4930.662	3102.339	27.867	23.365
40	0	4908.818	3073.148	27.929	22.928
35	0	4896.349	3051.832	28.054	22.611
30	0	4879.115	3038.143	27.915	22.408
25	0	4872.359	3004.279	28.418	21.912
20	0	4844.558	2961.120	28.595	21.287
15	0	4794.629	2884.454	28.877	20.199
10	0	4724.700	2826.883	28.326	19.400
5	0	4526.169	2693.072	26.258	17.607
20	5	4826.794	2914.053	29.073	20.615
25	10	4833.174	2913.929	29.225	20.613
30	15	4832.886	2911.878	29.257	20.584
35	20	4834.962	2912.106	29.302	20.588
40	25	4834.299	2913.659	29.257	20.610
45	30	4839.714	2941.377	28.859	21.004
50	35	4841.001	2942.327	28.871	21.017
55	40	4844.235	2943.189	28.930	21.030
60	45	4848.427	2943.190	29.029	21.030
35	5	4880.620	3009.356	28.514	21.986
40	10	4895.886	3017.905	28.710	22.111
45	15	4900.540	3025.806	28.666	22.227
50	20	4907.417	3043.918	28.474	22.494
55	25	4908.712	3044.686	28.490	22.505
60	30	4915.629	3042.625	28.695	22.475

Sample SB005 (dry)

P _C (Mpa)	P _P (Mpa)	V _P (m/s)	V _S (m/s)	κ (GPa)	μ (GPa)
5	0	4664.703	2914.520	25.624	20.862

10	0	4878.381	3060.564	27.775	23.005
15	0	4988.109	3195.049	27.679	25.071
20	0	5059.650	3251.817	28.246	25.970
25	0	5104.313	3298.624	28.357	26.723
30	0	5133.427	3336.892	28.257	27.347
35	0	5153.216	3362.248	28.201	27.764
40	0	5154.810	3378.456	27.884	28.032
45	0	5186.243	3392.676	28.367	28.269
50	0	5193.096	3406.246	28.239	28.495
55	0	5218.009	3419.152	28.588	28.712
60	0	5228.223	3430.205	28.602	28.898
55	0	5224.682	3424.462	28.640	28.801
50	0	5234.913	3427.293	28.839	28.849
45	0	5215.833	3420.152	28.510	28.729
40	0	5197.931	3407.834	28.327	28.522
35	0	5194.606	3393.727	28.557	28.286
30	0	5160.103	3375.804	28.076	27.988
25	0	5150.027	3350.204	28.385	27.565
20	0	5110.984	3315.613	28.156	26.999
15	0	5061.309	3259.149	28.131	26.087
10	0	4981.919	3194.833	27.532	25.068
5	0	4801.569	3055.939	26.042	22.936

Sample SB005 (water saturated)

P _C (Mpa)	P _P (Mpa)	V _P (m/s)	V _S (m/s)	κ (GPa)	μ (GPa)
5	0	4759.250	2833.277	29.748	19.988
10	0	4850.642	3026.496	28.176	22.807
15	0	4922.257	3082.426	28.784	23.658
20	0	4965.792	3142.464	28.616	24.589
25	0	5018.869	3188.380	28.970	25.312
30	0	5038.837	3218.031	28.839	25.785
35	0	5063.096	3242.755	28.919	26.183
40	0	5080.304	3261.599	28.947	26.488
45	0	5097.991	3279.357	29.010	26.778
50	0	5107.672	3298.561	28.836	27.092
55	0	5125.628	3310.294	29.036	27.285
60	0	5141.823	3323.691	29.155	27.507
55	0	5136.805	3314.847	29.222	27.360
50	0	5122.149	3303.968	29.087	27.181
45	0	5105.945	3290.706	28.964	26.963
40	0	5098.056	3274.567	29.116	26.699
35	0	5080.618	3260.737	28.974	26.474
30	0	5061.389	3238.561	28.967	26.115
25	0	5026.570	3210.426	28.694	25.664
20	0	4994.983	3176.177	28.632	25.119
15	0	4937.907	3107.368	28.656	24.042

10	0	4865.032	3034.757	28.358	22.932
5	0	4738.008	2848.414	28.960	20.202
15	0	4920.689	3074.027	28.918	23.529
20	5	4938.241	3082.917	29.167	23.666
25	10	4940.791	3079.519	29.299	23.613
30	15	4943.680	3085.491	29.248	23.705
35	20	4943.883	3086.516	29.232	23.721
40	25	4957.992	3092.624	29.454	23.815
45	30	4974.306	3094.565	29.818	23.845
50	35	4975.824	3097.792	29.789	23.895
55	40	4977.305	3090.343	29.979	23.780
60	45	4980.695	3105.385	29.754	24.012
55	40	4981.843	3106.583	29.758	24.030
50	35	4980.521	3098.999	29.881	23.913
45	30	4977.230	3096.999	29.841	23.882
40	25	4964.510	3091.873	29.631	23.803
35	20	4957.477	3092.064	29.453	23.806
30	15	4947.964	3091.467	29.231	23.797
25	10	4943.817	3088.030	29.199	23.744
20	5	4940.834	3086.881	29.149	23.727
15	0	4937.907	3107.368	28.656	24.042
30	0	5038.837	3218.031	28.839	25.785
35	5	5044.472	3214.260	29.061	25.725
40	10	5055.115	3221.934	29.165	25.848
45	15	5058.343	3222.446	29.235	25.856
50	20	5059.845	3224.758	29.224	25.893
55	25	5061.396	3230.112	29.148	25.979
60	30	5071.152	3235.465	29.279	26.066
55	25	5067.617	3234.234	29.217	26.046
50	20	5066.481	3232.239	29.231	26.014
45	15	5061.428	3231.293	29.124	25.998
40	10	5059.780	3228.941	29.133	25.961
35	5	5056.413	3227.932	29.069	25.944
30	0	5061.389	3238.561	28.967	26.115

Sample SB006 (dry)

P_C (Mpa)	P_P (Mpa)	V_P (m/s)	V_S (m/s)	κ (GPa)	μ (GPa)
5	0	3320.531	2174.602	11.540	11.560
10	0	3748.695	2455.336	14.702	14.737
15	0	4065.448	2669.816	17.170	17.424
20	0	4267.795	2813.934	18.716	19.356
25	0	4406.740	2930.721	19.476	20.996
30	0	4532.795	3014.640	20.604	22.216
35	0	4630.702	3095.511	21.187	23.424

40	0	4712.374	3146.756	22.010	24.206
45	0	4779.172	3194.603	22.571	24.947
50	0	4846.336	3241.407	23.169	25.684
55	0	4879.658	3278.267	23.178	26.271
60	0	4926.810	3302.812	23.782	26.666
55	0	4908.210	3291.242	23.583	26.480
50	0	4886.272	3274.197	23.423	26.206
45	0	4845.905	3244.534	23.093	25.733
40	0	4796.489	3203.660	22.787	25.089
35	0	4726.517	3154.307	22.181	24.322
30	0	4638.559	3102.748	21.219	23.533
25	0	4518.971	3015.973	20.272	22.235
20	0	4386.520	2926.986	19.113	20.943
15	0	4183.219	2761.376	17.924	18.640
10	0	3897.181	2520.177	16.426	15.526
5	0	3476.200	2284.398	12.531	12.757

Sample SB006 (water saturated)

P_C (Mpa)	P_P (Mpa)	V_P (m/s)	V_S (m/s)	κ (GPa)	μ (GPa)
5	0	4477.326	2628.309	27.171	17.322
10	0	4590.205	2768.702	27.204	19.222
15	0	4706.091	2917.432	27.078	21.342
20	0	4792.112	3017.894	27.133	22.838
25	0	4848.083	3097.889	26.850	24.064
30	0	4903.427	3149.216	27.132	24.868
35	0	4945.168	3191.576	27.265	25.542
40	0	4990.605	3234.350	27.478	26.231
45	0	5011.115	3256.547	27.510	26.592
50	0	5040.001	3281.540	27.692	27.002
55	0	5066.428	3301.121	27.931	27.325
60	0	5076.119	3319.235	27.776	27.626
55	0	5068.487	3308.564	27.819	27.449
50	0	5048.957	3296.205	27.596	27.244
45	0	5035.853	3279.977	27.621	26.976
40	0	5006.804	3257.426	27.383	26.607
35	0	4978.944	3233.629	27.202	26.219
30	0	4947.662	3198.362	27.181	25.651
25	0	4903.956	3151.347	27.100	24.902
20	0	4841.079	3089.547	26.853	23.935
15	0	4763.183	2982.643	27.147	22.307
10	0	4628.136	2859.480	26.373	20.503
5	0	4429.745	2627.955	26.114	17.317
15	0	4706.091	2917.432	27.078	21.342
20	5	4786.766	2993.445	27.496	22.469
25	10	4774.605	2989.928	27.275	22.416
30	15	4782.458	2990.822	27.445	22.430

35	20	4786.010	2988.166	27.584	22.390
40	25	4790.480	2990.806	27.638	22.429
45	30	4792.389	2992.165	27.657	22.450
50	35	4794.098	2992.211	27.697	22.451
55	40	4809.265	2993.500	28.036	22.470
60	45	4799.099	2996.146	27.738	22.510
55	40	4794.148	2992.886	27.685	22.461
50	35	4784.912	2992.675	27.467	22.458
45	30	4780.104	2991.526	27.375	22.440
40	25	4777.742	2991.577	27.317	22.441
35	20	4766.252	2988.672	27.100	22.397
30	15	4762.759	2988.162	27.027	22.390
25	10	4757.547	2985.545	26.955	22.351
20	5	4758.190	2985.362	26.974	22.348
15	0	4763.183	2982.643	27.147	22.307
30	0	4903.427	3149.216	27.132	24.868
35	5	4935.490	3183.601	27.195	25.414
40	10	4942.405	3183.807	27.362	25.418
45	15	4936.577	3183.897	27.215	25.419
50	20	4943.867	3183.943	27.395	25.420
55	25	4949.195	3184.625	27.513	25.431
60	30	4943.808	3188.587	27.295	25.494
55	25	4940.186	3186.495	27.249	25.461
50	20	4940.001	3184.559	27.286	25.430
45	15	4936.478	3183.126	27.229	25.407
40	10	4930.559	3181.639	27.114	25.383
35	5	4927.580	3180.711	27.061	25.368
30	0	4947.662	3198.362	27.181	25.651

Sample SB007 (dry)

P _C (Mpa)	P _P (Mpa)	V _P (m/s)	V _S (m/s)	κ (GPa)	μ (GPa)
5	0	3065.262	1811.625	12.202	7.978
10	0	3508.361	2166.509	14.706	11.409
15	0	3885.173	2430.417	17.547	14.358
20	0	4138.470	2626.600	19.271	16.770
25	0	4326.217	2770.434	20.618	18.657
30	0	4470.484	2876.177	21.768	20.108
35	0	4583.983	2966.372	22.558	21.389
40	0	4675.928	3036.546	23.262	22.413
45	0	4756.710	3104.391	23.764	23.425
50	0	4825.321	3158.607	24.262	24.251
55	0	4867.617	3204.723	24.307	24.964
60	0	4922.140	3242.822	24.809	25.561
55	0	4890.672	3219.115	24.554	25.189
50	0	4864.753	3195.542	24.430	24.821

45	0	4821.950	3157.320	24.209	24.231
40	0	4758.467	3101.041	23.872	23.375
35	0	4686.042	3034.653	23.530	22.385
30	0	4599.889	2954.309	23.145	21.215
25	0	4473.009	2851.710	22.277	19.767
20	0	4299.276	2714.289	21.052	17.908
15	0	4061.923	2527.055	19.408	15.523
10	0	3701.146	2261.020	16.729	12.426
5	0	3125.893	1906.221	11.974	8.832

Sample SB007 (water saturated)

P _C (Mpa)	P _P (Mpa)	V _P (m/s)	V _S (m/s)	κ (GPa)	μ (GPa)
5	0	4220.094	2177.989	28.685	11.848
10	0	4442.428	2473.142	28.923	15.277
15	0	4621.217	2691.981	29.207	18.100
20	0	4728.959	2827.989	29.223	19.976
25	0	4796.611	2923.269	29.007	21.344
30	0	4859.221	3002.010	28.963	22.510
35	0	4914.688	3061.113	29.124	23.405
40	0	4950.460	3111.128	28.977	24.176
45	0	4980.230	3150.645	28.892	24.794
50	0	5014.569	3177.551	29.182	25.219
55	0	5036.930	3209.062	29.073	25.722
60	0	5051.323	3231.217	28.961	26.078
55	0	5042.570	3216.249	29.061	25.837
50	0	5024.823	3204.839	28.859	25.654
45	0	5007.665	3175.513	29.052	25.187
40	0	4977.910	3149.185	28.865	24.771
35	0	4945.903	3110.321	28.882	24.163
30	0	4905.847	3055.428	29.023	23.318
25	0	4856.125	2990.949	29.109	22.344
20	0	4790.332	2900.444	29.300	21.012
15	0	4689.531	2775.933	29.267	19.247
10	0	4550.756	2587.590	29.428	16.724
5	0	4280.505	2270.241	28.601	12.873
15	0	4621.217	2691.981	29.207	18.100
20	5	4680.457	2728.619	29.922	18.596
25	10	4674.225	2730.319	29.745	18.620
30	15	4681.403	2732.412	29.875	18.648
35	20	4682.225	2731.406	29.912	18.634
40	25	4685.019	2728.178	30.036	18.590
45	30	4686.686	2739.522	29.869	18.745
50	35	4695.930	2732.823	30.207	18.654
55	40	4699.830	2738.510	30.195	18.731
60	45	4693.926	2737.415	30.077	18.717
55	40	4685.005	2731.780	29.970	18.640
50	35	4687.622	2732.790	30.013	18.653

45	30	4684.863	2733.850	29.929	18.668
40	25	4675.777	2730.219	29.783	18.618
35	20	4669.853	2730.219	29.645	18.618
30	15	4666.357	2725.652	29.646	18.556
25	10	4665.153	2722.003	29.684	18.506
20	5	4666.535	2731.249	29.549	18.632
15	0	4689.531	2775.933	29.267	19.247
30	0	4859.221	3002.010	28.963	22.510
35	5	4898.029	3036.718	29.211	23.033
40	10	4902.491	3047.728	29.097	23.200
45	15	4904.950	3047.520	29.162	23.197
50	20	4906.077	3047.576	29.188	23.198
55	25	4917.588	3048.941	29.443	23.219
60	30	4909.080	3052.778	29.156	23.277
55	25	4909.172	3050.144	29.212	23.237
50	20	4902.330	3050.185	29.043	23.238
45	15	4902.849	3046.292	29.135	23.179
40	10	4897.082	3048.905	28.941	23.218
35	5	4892.521	3045.010	28.909	23.159
30	0	4905.847	3055.428	29.023	23.318

Sample SB008 (dry)

P _c (Mpa)	P _p (Mpa)	V _p (m/s)	V _s (m/s)	κ (GPa)	μ (GPa)
5	0	3238.010	2031.071	12.324	10.200
10	0	3511.816	2231.790	14.073	12.315
15	0	3758.457	2408.277	15.807	14.340
20	0	3955.090	2555.061	17.155	16.142
25	0	4108.367	2669.604	18.238	17.621
30	0	4250.066	2774.342	19.287	19.031
35	0	4370.979	2861.596	20.243	20.247
40	0	4478.279	2938.013	21.130	21.343
45	0	4569.037	3004.055	21.866	22.313
50	0	4658.890	3068.047	22.635	23.274
55	0	4711.149	3114.821	22.893	23.989
60	0	4777.162	3160.234	23.502	24.693
55	0	4748.785	3140.850	23.236	24.391
50	0	4709.612	3112.789	22.899	23.958
45	0	4658.716	3073.255	22.526	23.353
40	0	4580.971	3021.938	21.781	22.580
35	0	4491.671	2958.798	21.023	21.646
30	0	4381.598	2875.894	20.202	20.450
25	0	4239.903	2777.541	19.015	19.075
20	0	4076.833	2656.730	17.826	17.452
15	0	3886.355	2518.332	16.437	15.681
10	0	3629.414	2328.904	14.689	13.411

5	0	3343.547	2132.751	12.646	11.247
---	---	----------	----------	--------	--------

Sample SB008 (water saturated)

P _C (Mpa)	P _P (Mpa)	V _P (m/s)	V _S (m/s)	κ (GPa)	μ (GPa)
5	0	4199.629	2421.244	24.841	14.829
10	0	4419.697	2606.508	26.497	17.185
15	0	4546.946	2724.073	27.270	18.771
20	0	4652.782	2819.172	27.955	20.104
25	0	4700.213	2867.300	28.154	20.796
30	0	4753.258	2918.778	28.418	21.550
35	0	4800.642	2960.528	28.735	22.171
40	0	4846.908	3004.155	28.987	22.829
45	0	4887.087	3047.736	29.086	23.496
50	0	4925.769	3078.588	29.409	23.974
55	0	4966.463	3110.021	29.771	24.466
60	0	4997.578	3152.667	29.655	25.142
55	0	4998.011	3147.594	29.773	25.061
50	0	4981.988	3135.392	29.628	24.867
45	0	4958.091	3114.721	29.462	24.540
40	0	4926.440	3087.196	29.247	24.108
35	0	4881.561	3053.709	28.827	23.588
30	0	4843.450	3009.747	28.788	22.914
25	0	4781.978	2954.993	28.393	22.088
20	0	4701.898	2884.626	27.858	21.048
15	0	4597.610	2789.398	27.227	19.682
10	0	4430.709	2658.983	25.812	17.884
5	0	4118.004	2435.712	22.887	15.007
15	0	4546.946	2724.073	27.270	18.771
20	5	4666.294	2848.316	27.716	20.522
25	10	4731.401	2914.036	27.987	21.480
30	15	4753.117	2922.417	28.343	21.604
35	20	4736.592	2900.429	28.378	21.280
40	25	4720.513	2879.487	28.402	20.974
45	30	4714.646	2868.380	28.477	20.812
50	35	4711.425	2862.288	28.518	20.724
55	40	4714.184	2855.226	28.720	20.622
60	45	4706.472	2851.328	28.611	20.565
55	40	4686.801	2835.426	28.449	20.337
50	35	4674.324	2822.547	28.399	20.152
45	30	4659.049	2811.411	28.250	19.994
40	25	4645.114	2802.692	28.087	19.870
35	20	4631.674	2797.114	27.877	19.791
30	15	4624.079	2790.010	27.833	19.690
25	10	4615.249	2780.748	27.801	19.560
20	5	4613.879	2726.135	28.783	18.799

15	0	4597.610	2789.398	27.227	19.682
30	0	4753.258	2918.778	28.418	21.550
35	5	4776.577	2948.334	28.395	21.988
40	10	4794.915	2964.858	28.510	22.236
45	15	4806.517	2974.074	28.607	22.374
50	20	4820.907	2980.916	28.820	22.477
55	25	4835.417	2987.128	29.049	22.571
60	30	4827.273	2991.442	28.763	22.636
55	25	4822.492	2985.257	28.771	22.543
50	20	4814.357	2981.568	28.647	22.487
45	15	4814.379	2978.352	28.712	22.438
40	10	4802.461	2976.592	28.458	22.412
35	5	4794.842	2977.783	28.249	22.430
30	0	4843.450	3009.747	28.788	22.914

Sample SB009 (dry)

P _C (Mpa)	P _P (Mpa)	V _P (m/s)	V _S (m/s)	κ (GPa)	μ (GPa)
5	0	3347.572	2116.236	13.288	11.368
10	0	3590.651	2271.368	15.265	13.096
15	0	3816.880	2393.653	17.589	14.544
20	0	4030.648	2553.999	19.162	16.557
25	0	4175.283	2660.845	20.289	17.972
30	0	4328.105	2765.958	21.657	19.420
35	0	4462.198	2861.002	22.839	20.777
40	0	4580.459	2939.831	24.005	21.938
45	0	4680.710	3009.880	24.952	22.996
50	0	4773.006	3072.699	25.873	23.966
55	0	4832.835	3127.315	26.186	24.825
60	0	4905.722	3176.690	26.934	25.615
55	0	4876.155	3157.703	26.607	25.310
50	0	4839.551	3126.499	26.368	24.812
45	0	4785.388	3090.666	25.799	24.247
40	0	4709.055	3037.029	25.072	23.412
35	0	4612.975	2976.584	24.028	22.490
30	0	4504.863	2896.987	23.108	21.303
25	0	4358.795	2795.301	21.781	19.834
20	0	4196.209	2677.139	20.439	18.192
15	0	3996.570	2536.651	18.766	16.333
10	0	3729.133	2340.608	16.758	13.906
5	0	3418.337	2172.283	13.690	11.978

Sample SB009 (water saturated)

P _C (Mpa)	P _P (Mpa)	V _P (m/s)	V _S (m/s)	κ (GPa)	μ (GPa)
----------------------	----------------------	----------------------	----------------------	---------	---------

5	0	4295.250	2326.028	29.036	13.982
10	0	4511.728	2561.270	30.001	16.954
15	0	4629.213	2658.053	31.036	18.259
20	0	4716.521	2748.673	31.456	19.525
25	0	4791.475	2831.476	31.706	20.719
30	0	4863.087	2895.603	32.227	21.668
35	0	4934.216	2963.287	32.662	22.693
40	0	4985.701	3014.147	32.934	23.479
45	0	5025.543	3056.560	33.078	24.144
50	0	5072.419	3101.249	33.353	24.856
55	0	5114.561	3133.428	33.771	25.374
60	0	5133.204	3164.734	33.585	25.884
55	0	5142.005	3164.017	33.835	25.872
50	0	5125.059	3156.228	33.555	25.745
45	0	5100.292	3134.357	33.374	25.389
40	0	5059.168	3101.231	33.006	24.855
35	0	5013.127	3061.636	32.649	24.225
30	0	4958.632	3011.199	32.300	23.433
25	0	4883.835	2951.679	31.620	22.516
20	0	4786.217	2873.374	30.752	21.337
15	0	4640.709	2755.170	29.500	19.618
10	0	4423.301	2602.817	27.220	17.508
5	0	4039.876	2315.403	23.705	13.855
15	0	4629.213	2658.053	31.036	18.259
20	5	4686.701	2711.097	31.439	18.995
25	10	4684.977	2721.439	31.203	19.140
30	15	4702.248	2724.331	31.568	19.181
35	20	4705.028	2727.905	31.569	19.231
40	25	4713.197	2729.626	31.735	19.256
45	30	4716.740	2732.612	31.765	19.298
50	35	4727.426	2737.296	31.938	19.364
55	40	4739.515	2738.497	32.211	19.381
60	45	4732.378	2741.549	31.978	19.424
55	40	4725.509	2734.293	31.948	19.321
50	35	4718.237	2734.341	31.769	19.322
45	30	4720.259	2732.029	31.862	19.289
40	25	4709.191	2733.249	31.569	19.307
35	20	4698.970	2729.578	31.390	19.255
30	15	4701.308	2727.361	31.488	19.224
25	10	4690.520	2721.983	31.328	19.148
20	5	4687.048	2720.251	31.276	19.124
15	0	4640.709	2755.170	29.500	19.618
30	0	4863.087	2895.603	32.227	21.668
35	5	4888.322	2929.144	32.190	22.173
40	10	4908.456	2955.412	32.167	22.573
45	15	4921.650	2968.177	32.242	22.768
50	20	4933.586	2972.406	32.459	22.833

55	25	4944.798	2975.972	32.672	22.888
60	30	4938.902	2980.802	32.423	22.962
55	25	4935.408	2978.045	32.390	22.920
50	20	4929.347	2977.998	32.237	22.919
45	15	4933.467	2978.009	32.341	22.919
40	10	4923.429	2975.922	32.129	22.887
35	5	4915.984	2972.397	32.011	22.833
30	0	4958.632	3011.199	32.300	23.433